NTNU
Norwegian University of
Science and Technology

In situ characterization of industrial catalysts with Raman spectroscopy

My Nhung Thi Tran

Chemical Engineering and Biotechnology
Submission date: June 2018
Supervisor: Magnus Rønning, IKP
Co-supervisor: Samuel K. Regli, IKP

Norwegian University of Science and Technology
Department of Chemical Engineering

"Success can come to you by courageous Devotion to the task lying in front of you"
C.V. Raman

Preface

This master thesis has been carried out at the Department of Chemical Engineering, Catalysis group at the Faculty of Science and Norwegian University of Science and Technology (NTNU). This work is a continuation of the Specialization Project in the fall of 2017 in the course TKP4580 Chemical Engineering. The project is affiliated with iCSI, a Centre for research based innovation (SFI).

Foremost, I would like to express my gratitude to my supervisor, Professor **Magnus Rønning** for his supervising, support and research guidance. I also wish to thank my co-supervisor Ph.D. candidate, **Samuel K. Regli** for providing excellent training in the use of Raman spectrometer, his motivation, encouragement, and support.

I would also like to give a special thanks to **Estelle Marie M. Vanhaecke** for laboratory guidance, which is very much appreciated, motivation, and support throughout the course. Additionally, I would like to thank **Ata ul Rauf Salman** for his kind help regarding the experimental work.

Declaration of compliance:

I declare that this is an independent work according to the exam regulations of the Norwegian University of Science and technology (NTNU).

Trondheim, June 26th, 2018

My Nhung Tran

Abstract

Raman spectroscopy is one of the most powerful characterization methods for *in situ* Raman study of catalytic materials and surfaces under working conditions. The use of Raman spectroscopy in catalytic NO oxidation would be of interest, as it provides fundamental information about catalytic molecular structures of the active phase and surface reaction intermediates. The platinum metal supported oxides catalyst are found to be the most active in NO oxidation, as they have an outstanding activity over a range of conditions.

Herein, a systematic work was performed to study the advanced characterization method, *in situ* Raman Spectroscopy by characterization of active platinum based catalysts for NO oxidation. Two supported metal oxides catalyst, 5wt.% Pt/Al_2O_3 and 5wt.% Pt/ZrO_2, were synthesized by one step aqueous incipient wetness impregnation. Catalysts were characterized by nitrogen adsorption, X-Ray diffraction (XRD), CO chemisorption and temperature programmed reduction (TPR). The catalysts have furthermore been investigated by *ex situ* Raman spectroscopy at ambient conditions and *in situ* Raman spectroscopy at industrially relevant conditions in terms of temperature at atmospheric pressure under different atmospheres (O_2, H_2, Ar).

The characterization techniques indicated that the catalysts contained both small and large particles detected by CO chemisorption and XRD, respectively. Both Pt and PtO_2 were identified, but due to the low metal loading, the associated Raman band could not be detected. However, a Raman band located at 577 cm^{-1} attributed to a Pt-O stretch, was identified in the Raman spectra of 5wt.% Pt/Al_2O_3, but due to the complications with the *in situ* cell window the experiment could not be further carried out. It is, therefore, recommended to try more suitable *in situ* cell windows to optimize the Raman signals.

Ex situ Raman measurements were well established to gain a better understanding of the principle of Raman spectroscopy and Raman parameters. A quite complex *In situ* Raman spectroscopic characterization procedure of 5wt.% Pt/ZrO_2 under certain reaction conditions was successfully carried out using a quartz *in situ* cell window. However, this could be adapted to some other materials which can be more Raman active.

Sammendrag

Raman spektroskopi er en av de mest kraftfulle karakteriseringsmetodene for *in situ* Raman studier av katalytiske materialer og overflater under gitte arbeidsforhold. Bruken av Raman spektroskopi i katalytisk NO oksidasjon vil være interessant, da den gir grunnleggende informasjon om den katalytiske molekylære strukturen av den aktive fasen og mellomprodukter under overflatereaksjoner. Platina metall med bærer er kjent til å være den mest aktive katalysatoren i NO oksidasjon systemer, da den utfører de mest fremragende aktiviteter over en rekke forhold.

I dette prosjektet er det utført et systematisk arbeid for å studere den avanserte karakteriseringsmetoden, *in situ* Raman spektroskopi ved karakterisering av aktive platina baserte katalysatorer for NO oksidasjon. To katalysatorer, 5wt% Pt/Al_2O_3 og 5wt.% Pt/ZrO_2, ble syntetisert ved impregnering. Katalysatorene ble karakterisert ved nitrogen adsorpsjon, røntgendiffraksjon (XRD), CO-kjemisorption og temperaturprogrammert reduksjon (TPR). Videre er det blitt undersøkt en *ex situ* Raman spektroskopi ved omgivende forhold og *in situ* Raman spektroskopi ved industrielle forhold med hensyn på temperaturer ved atmosfærisk trykk under forskjellig atmosfærer (O_2, H_2, Ar).

Karakteriseringsteknikkene indikerte at katalysatorene inneholdt både små og store partikler som er detektert av henholdsvis CO-kjemisorption og XRD. Både Pt og PtO_2 ble identifisert, men på grunn av den lave vektprosenten av metallet, ble det ikke observert noen tilhørende Raman topper. Imidlertid ble en Raman topp lokalisert ved 577 cm^{-1}, som tilhører en Pt-O binding identifisert i Raman spektrene på 5wt% Pt/Al_2O_3, men på grunn av noen komplikasjoner med *in situ* vinduet, kunne ikke eksperimentet utføres. Det anbefales derfor å prøve andre *in situ* vinduer som er mer passende for å optimalisere Raman signalet.

Både *ex situ* og *in situ* Raman spektroskopi målinger ble gjennomført i dette studiet. *Ex situ* Raman målinger var godt etablert for å få en bedre forståelse av prinsippet Raman spektroskopi og Raman parametere. Det var utført en vellykket kompleks *in situ* Raman spektroskopisk karakteriseringsprosedyre på 5wt% Pt/ZrO_2 under bestemte reaksjonsbetingelser ved bruk av *in situ* kvarts vindu. Dette *in situ* eksperimentet kunne imidlertid tilpasses til andre materialer som kan være mer Raman aktive.

Abbreviations

BET Brunauer-Emmett-Teller

CCD Couple charge device

CCR Catalyst cell reactor

c-BN Cubic boron nitride

He-Cd Helium cadmium laser

He-Ne Helium neon laser

IR Infrared

LO Longitudinal mode

LWP Long wave pass

MFC Mass flow controller

MS Mass spectrometer

NUV Near ultra violet

PE Potential energy

SWP Short wave pass

TO Transverse optical mode

TCD Thermal conductivity detector

TPR Temperature programmed reduction

UV Ultra violet

XRD X-Ray diffraction

Symbols

α Polarizability

β Peak width

λ Wavelength

θ Diffraction angle

σ Average area

μ Induced dipole moment

A Specific metal surface area

$\mathbf{a}_m$ Surface area

c Speed of light

C BET constant

d Distance between two lattice planes

D Metal dispersion

$\mathbf{D}_o$ Energy required to break band

E Electric field

$\mathbf{E}_p$ Potential energy

h Plank's constant

K Constant

L Avogadro's constant

<L> Dimension of the particle

m Mass

M Atomic mass of metal

P Pressure

$\mathbf{P}_o$ Saturated vapour pressure

V Volume

$\mathbf{V}_{imp}$ Liquid volume

$\mathbf{V}_m$ Volume of an adsorbed monolayer

$\mathbf{V}_p$ Pore volume

υ_m Molar volume

υ Frequency

υ_i Quantum number

X Displacement vectors

Contents

List of Tables

List of Figures

Chapter 1

Introduction

1.1 Motivation

Over the past few decades *in situ* Raman spectroscopy has become a common catalyst characterization method with the help of reaction cells designed to combine *in situ* molecular characterization studies with simultaneous fundamental quantitative kinetics studies [1]. The phenomena Raman effect was first discovered in 1928 by Sir Chandrasekhara Venkata Raman and is based on the frequency of a small fraction of scattered light that is different from the frequency of monochromatic incident light [2]. At that time measurements were time-consuming and complicated as only crude instrument was available. Sir Raman used sunlight as the source, a telescope as the collector and his own eyes as the detector [3]. As time passed, the various components of Raman instrumentation were gradually improved and making it much more approachable technique. Raman spectroscopy today is among the handful catalyst characterization techniques that can provide information in molecular level about heterogeneous catalyst under *in situ* controlled environmental conditions [1].

About thirty years ago only a handful of Raman spectroscopy was published in the catalysis literature, but none were *in situ* studies. Presently, the number of publications of Raman spectroscopy studies appeared in the catalysis literature were an amount of 1322 publications of which 221 are *in situ* studies [1]. This demonstrates the fast growing of *in situ* Raman studies, the dynamic nature of heterogeneous catalyst surfaces, and the importance of performing characterization studies under reaction conditions. Raman spectroscopy is undoubtedly one of the most powerful *in situ* characterization technique of catalytic materials. Raman spectroscopy has, as compared to other technique a straightforward construction of *in situ* reactors, no interference of the gas phase or the support and high reaction temperatures [4].

The environmental problems regarding air quality due to air pollutant have been the center of attention over the past years. The primary source of air pollution is a large number of combustion processes of fossil fuel power plants, in vehicles and other industrial processes [5]. Nitrogen oxides (NOx) are considered to be the primary air pollutants since they contribute to such environmental problems as photochemical smog, acid rain, ozone depletion and even global warming [6]. Utilization of supported metal oxide catalysts for NO oxidation reactions has significantly increased over the past few decades due to their excellent catalytic properties in the production of chemical intermediates and improvement in pollution control strategies. Such supported metal oxide catalysts are well suited for Raman spectroscopic studies [7]. The utilization of the powerful characterization technique, *in situ* Raman spectroscopy in catalytic oxidation reaction would be of interest, as it provides fundamental information about catalytic molecular structures of the active phase and surface reaction intermediates [7]. The harmful effect of NOx on the environment has forced the governments to introduce new and strict regulations regarding these NOx emissions. A considerable amount of oxidation catalysts has for this reason been studied for NO oxidation [5]. The most commonly used catalyst is the supported noble metals, as they have an outstanding activity over a range of conditions. For NO oxidation, different platinum-based catalysts are found to be most active one [6].

One study investigated adsorbed oxygen and NOx species on Pt/γ-alumina catalyst with UV Raman. It was found that under oxidizing conditions, a broad peak at 571 cm^{-1} was observed, which they attributed to the Pt-O stretch of atomic oxygen. The peak could further be easily removed under reducing conditions, even at room temperature, and the process is entirely reversible [8]. A similar study on a different noble metal, palladium, found that small PdO was reduced at a lower temperature, whereas larger particles were reduced at a higher temperature, under reducing conditions. This process showed that it is completely reversible under gas flows containing O_2 and H_2 [9].

1.2 Project Objective

The objective of this thesis is to study the advanced characterization method, *in situ* Raman Spectroscopy by characterization of active platinum based catalysts for NO oxidation system. The synthesized catalysts, alumina and zirconia supported platinum with metal loading of 5wt.% will be characterized using some of the main characterization techniques, to obtain information about the catalytic properties. Further, the catalyst will be investigated by *in situ* Raman at industrially relevant conditions in terms of temperature, atmospheric pressure, and feed composition. *Ex situ* Raman measurements were conducted to establish and to gain an understanding of the principle of Raman spectroscopy and the Raman parameters.

Chapter 2

Theory

Raman Spectroscopy

Raman spectroscopy is one of the most powerful vibrational spectroscopic techniques for the characterization of surfaces and solids of technological importance. With the high resolution and the broad spectral range (50 - 5000 cm^{-1}) of Raman spectroscopy, it allows experimentation of the nature of molecular species, identification of crystalline solid phases, and determination of the structure of non-crystalline surfaces phases [10].

2.1   Electromagnetic Radiation

All types of lights (including infrared) are in the category of the electromagnetic radiation. The radiation behaves like waves and consist of alternating electric and magnetic fields components. These components oscillate in a continuous sinusoidal wave motion normal to each other. Figure 2.1 shows the alternating electric and magnetic fields components. The Raman scattering is the result of the interaction of the oscillating electric field and the dipole moment in the molecule. The electric field is therefore only considered for topics about Raman spectroscopy.
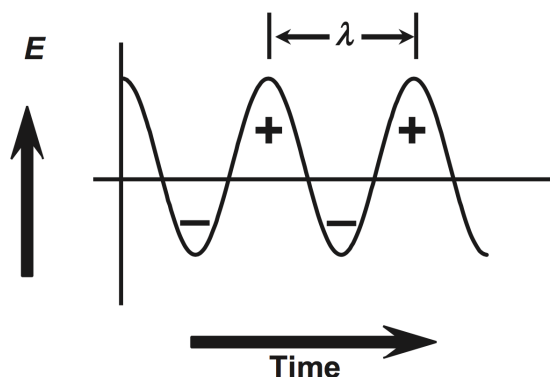
Figure 2.1: Alternating electric and magnetic field component that oscillates normal to each other. The wavelength, λ is the distance between two crests [11].

In vibrational spectroscopy, the photon energy is usually expressed as wavenumber, $\tilde{v}$, which is the number of waves per unit length (cm^{-1}). Frequencies and wavelengths are therefore generally transformed into wavenumbers and given by [11]:

$$\tilde{v} = \frac{v}{c/n} = \frac{1}{\lambda} \tag{2.1}$$

where v is the frequency (number of cycles per unit time), c is the speed of light and n the refractive index of the medium passing through and λ is the wavelength. According to quantum theory, the electromagnetic radiation is emitted from the photons, where the energy of the photon is expressed as:

$$E_p = hv \tag{2.2}$$

where h is Plank's constant and E_p is the potential energy. Photons may be absorbed or emitted by a molecule, resulting in a transfer of energy.

2.2 Simple Stretching Mode of a Diatomic Molecule

To get a better understanding of the vibrational mode of a molecule, a simple model is considered herein. The simple stretching mode of a diatomic molecule behaves as a simple quantum oscillator. Figure 2.2 shows the diatomic molecule with two different masses, m_1 and m_2 that is connected by a mass less spring. The displacement of the masses from the equilibrium position is denoted X_1 and X_2 which represents two different atoms in a diatomic molecule and K is the spring constant.
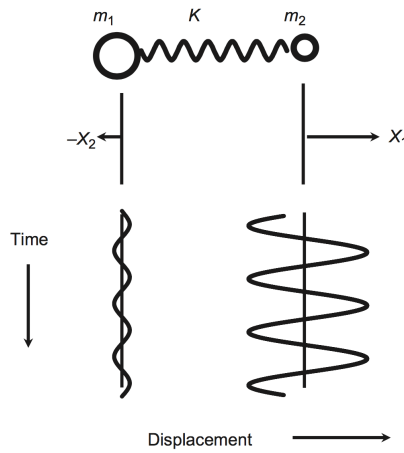
Figure 2.2: A simple model derived from classical mechanics. K, is the spring constant, m_1 and m_2 are masses and X_1 and X_2 are the displacement vectors [11].

As seen from the figure the displacement of the two different masses varies sinusoidal with time for a harmonic oscillator. However, both masses oscillate with the same frequency and goes through their equilibrium positions simultaneously. The amplitudes are inversely proportional to the mass which keeps it stationary and expressed by:

$$-\frac{X_1}{X_2} = \frac{m_2}{m_1} \tag{2.3}$$

The following expression of wavenumber, $\tilde{v}$, for a diatomic molecule is:

$$\tilde{v} = \frac{1}{2\pi c}\sqrt{K(\frac{1}{m_1} + \frac{1}{m_2})} \tag{2.4}$$

where K is the spring constant, c is the speed of light, m_1 and m_2 are masses and X_1 and X_2 are the displacement vectors.

2.3 Vibrational Energy Level Diagrams
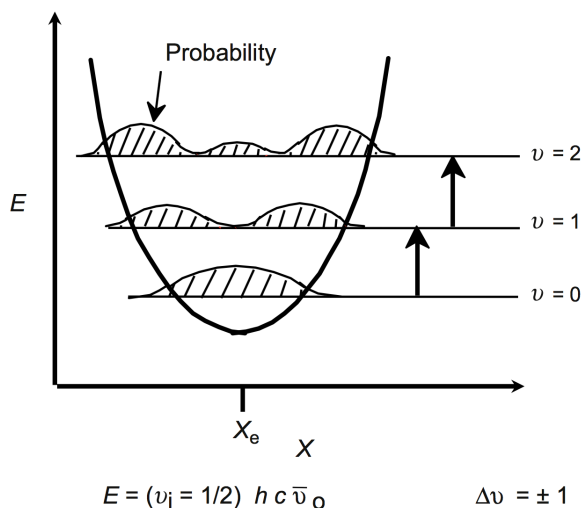
Figure 2.3: Illustration of the potential energy, E, of the different vibrational levels for a diatomic harmonic oscillator as a function of the internuclear distance, X [11].

The potential energy (PE) for a diatomic is expressed by:

$$PE = \frac{1}{2}KX^2 \tag{2.5}$$

In Figure 2.2, the relationship between the potential energy, PE and the distance, X between the two masses are shown. The internuclear distance, Xe has minimum potential energy and the force constant K is the measure of the potential well near Xe. However, the potential energy derived from Eq.2.5 is not continuously variable but somewhat quantified. Consequently, a molecule probed in spectroscopy can only have certain vibrational energy states. A molecule can transit from one energy state to another. The expression for the different energy levels E in the case of the harmonic potential is given by:

$$E_i = (v_i + \frac{1}{2})h\nu \quad v_i = 0,1,2... \tag{2.6}$$

where ν is the classical vibrational frequency, v_i is a quantum number which can only integer values. The change of ν is restricted to ±1 in harmonic oscillator model. This is called a fundamental transition, a transition such as $\nu=0$ to $\nu=2$ is not allowed. The zero point energy, $\nu=0$ cannot be removed from the molecule.

Although the harmonic oscillation gives a simple model of a diatomic molecule, it is

rather unrealistic. Anharmonic oscillation is therefore introduced due to its realistic approach. A larger transition in anharmonic is allowed. Most molecules would originate from its ground state (v=0) and usually to a virtual state (elastic scattering). A transition to higher vibrational level is far less probable and are of much weaker intensity, which is also called inelastic scattering. Figure 2.4 shows the potential energy diagram for the harmonic and anharmonic oscillator.
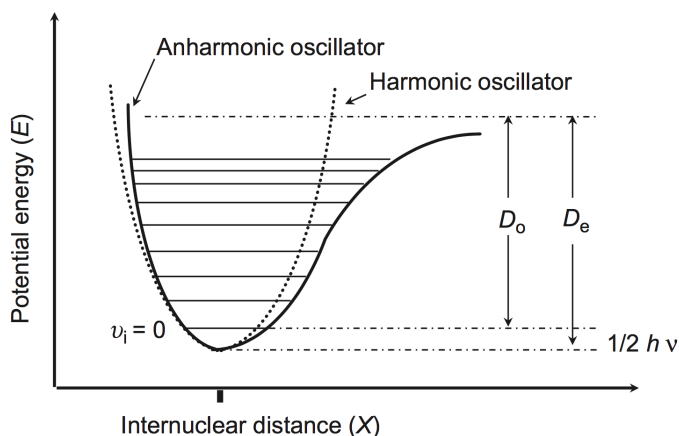
Figure 2.4: Comparison of potential energy diagram of the anharmonic system with the harmonic system. The diagram illustrates a transition from the v=0 level, and D_o is the energy required to break the bond [11].

2.4   Scattering Processes

The phenomena light scattering may be described classically and in terms of quantum mechanics. The classical arguments are described in terms of monochromatic light produced, by the interaction of electric field component with the oscillating dipoles in the molecule. The light scattered photons are primarily dominant of Rayleigh and occur as a result of a change in a molecules polarizability, which is the deformability of the electron cloud of the molecule, and hence resulting in a change in the dipole moment [11]:

$$\mu = \alpha E \tag{2.7}$$

where μ is the induced dipole moment, α is the polarizability and E is the incident electric field. In order for Raman bands to be detected, there must be a change in the polarizability.

However, it is more preferable to know the theory behind the light scattering in terms of quantum mechanics. Raman spectroscopy techniques use a laser light source to irradiate the sample with monochromatic radiation and generate Raman scattered light (Figure 2.5) which is detected as a Raman spectrum using a CCD (couple charge device) detector. The interaction of the light source with a molecule causes a change in electronic energy levels through the movement of the electrons. These scattering can either be Rayleigh (elastic) or Raman (inelastic) scattering [11]. The three different scattering processes are illustrated in Figure 2.6.
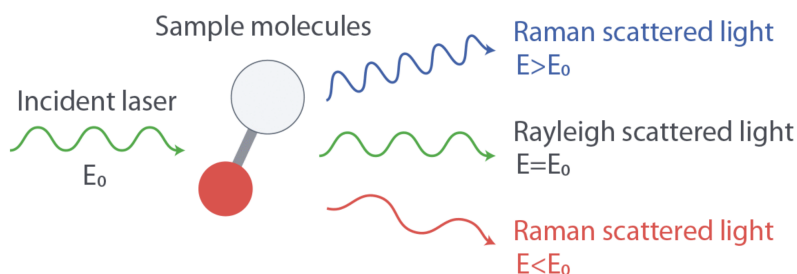
Figure 2.5: Schematic illustration of Rayleigh scattering and Stokes and Anti-Stokes Raman scattering [12].
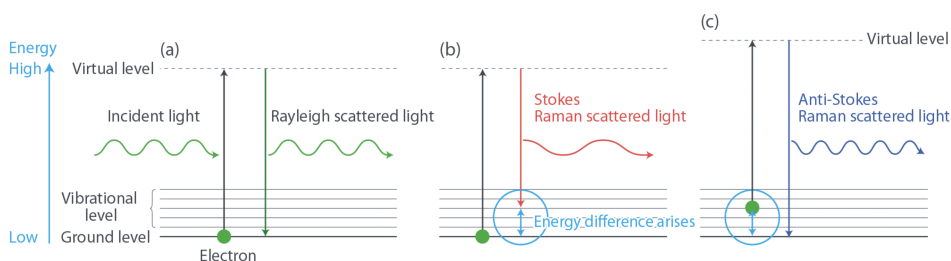
Figure 2.6: Illustration of three different scattering, Rayleigh and Raman scattering, where Stokes and Anti-Stokes are two varieties of Raman scattering. The upward arrows represent the laser excitation frequency, the downward arrows represent the scattered photon. a) Electrons are excited from the ground level and falls back down to the original ground level. b) Electrons are excited from the ground level and falls back down to the vibrational level. c)Electrons are excited from the vibrational level and falls back down to the ground level [12].

Most of the scattered light is dominated by Rayleigh (elastic) scattering, and only a small fraction are Raman scattering [11]. In Rayleigh scattering, the incident light is absorbed from the ground state, raised up to a virtual energy state, and further drops back down to its ground state. Since the electron falls back to its initial state there is

no change in energy. The energy of the scattered light is therefore equal to the energy of the incident light. In Raman scattering, the energy of the scattered light is different from the energy of the incident light. When the electron is excited from the initial ground state and falls back down to a higher energy vibrational level, the energy of the incident light is higher than the energy of the scattered light. This is called inelastic Stokes Raman scattering. The opposite process of the Stokes Raman scattering is the anti-Stokes Raman scattering. In this process, the electron is positioned in a vibrational state, rises to the virtual state and further falls back down to its ground state. This energy of the incident light is, therefore, lower than the energy of the scattered light [11]. Stokes and anti-Stokes provide the same information and are used to construct the Raman spectrum. A Raman spectrum is presented as an intensity of the scattered Raman versus wavenumber shift. The Stokes Raman bands involve a transition from lower to higher energy vibrational level, the intensity of Stokes is, therefore, higher than anti-Stokes and hence are measured in Raman spectroscopy [2].

2.5   Fluorescence

Raman scattering and fluorescence emission are two strongly competing phenomena, which have a similar base. In contrast to Raman scattering, some molecules are capable of being excited due to absorption of light energy. When the absorbed energy of the excitation photon provide sufficient energy, the molecule reaches a higher vibrational state, (Figure 2.7). Depending on the wavelength and energy of the excitation photon, multiple high vibrational states can be obtained. However, at these high energy state the molecule is quite unstable and will continuously seek the lowest vibrational excited state, where it is semi-stable. In this absorption process, energy is lost. When the molecule returns from the semi-stable state to the ground state, excess energy is released, and light is emitted [13]. Fluorescence band mainly appears in the range from 300 nm to 700 nm or at longer wavelength region [14]. Fluorescence emissions are often much more intense than Raman scattering and overlap the Raman features. Choosing a laser with a lower wavelength, such as UV-light can be used to avoid fluorescence since Raman scattering tends to be much more informative than fluorescence [10].
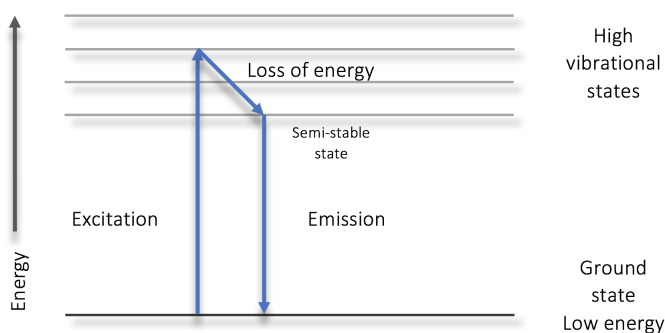
Figure 2.7: Absorption process for fluorescence. A molecule is excited to a very high vibrational state through absorption of light. At this state the molecule is unstable and seek the lowest vibrational excited state and loses energy. The molecule returns to the ground level and light is emitted. Modified Jablonski diagram of fluorescence by Jaffe and Miller [13].

2.6 Laser

The monochromatic light used in Raman spectroscopy ranges from 244 - 1064 nm, and the most common ones are ultraviolet light (UV), visible light and near infra-red (IR) with wavelengths 325 nm, 633 nm and 785 nm, respectively. The intensity of Raman scattering is proportional to λ^{-4}, where λ is the wavelength of the laser and the choice of laser wavelength has, therefore, an impact on the sensitivity of the desired analysis. Infrared laser with a wavelength of 785 nm would therefore results in a major decrease in the intensity of the scattering in comparison with blue/green visible laser. Certain vibrational modes of a substance interact better with specific wavelengths. Some materials could also be fluorescent with one wavelength and not with other wavelengths. Each of the various laser wavelengths requires an individual filter [15].
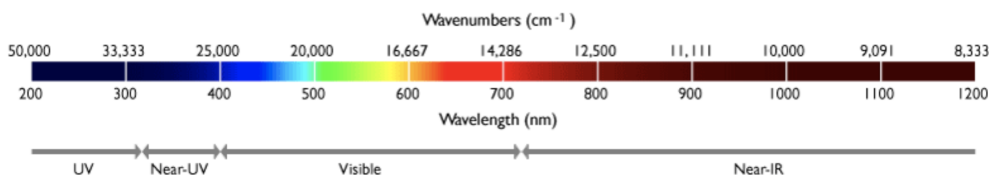
Figure 2.8: Illustration of various wavelengths for monochromatic light used in Raman spectroscopy [16].

Raman signal strength is proportional to the power of laser (milliwatts) exciting the sample. The stronger laser power used, the larger the Raman signal. However, one drawback of using full power laser is the chance of beam damage. It is therefore recommended to increase laser power gradually [17]. One possible way to avoid beam damage is to reduce the contact time between the sample and the laser spot by either moving the laser beam or the solid catalyst in a continuous mode [18].

2.7 Raman Parameters

2.7.1 Optical filters

One of the main challenges is to prevent the undesired light from Rayleigh scattering to overlap the relatively weak Raman signal. Different types of optical filters are therefore used to block Rayleigh scattering while allowing the Raman scattered light to reach the spectrometer and the detector. The four main types of filters to choose from in Raman spectroscopy (Figure 2.9) are: short wave pass (SWP) edge filter, long wave pass (LWP) edge filter, notch filter and laser line filter [16]. An edge filter absorbs all wavelengths up to a certain point and then transmits with high efficiency all wavelengths above this point. The edge filters offer excellent blocking of the laser, which makes the edge filter the superior alternative. Another advantage of the edge filter is that it is environmentally stable and has a near infinite lifetime [15]. The edge filters transmits either Stokes (LWP) or anti-Stokes (SWP). A notch filter has a sharp, discrete absorption which coincides with a specific laser wavelength. While the laser line filters transmit only the laser and block all other light, the notch filter prevents just the laser line. A combination of the notch filter and laser line blocks all the light and transmit both Stokes and anti-Stokes Raman scattering.
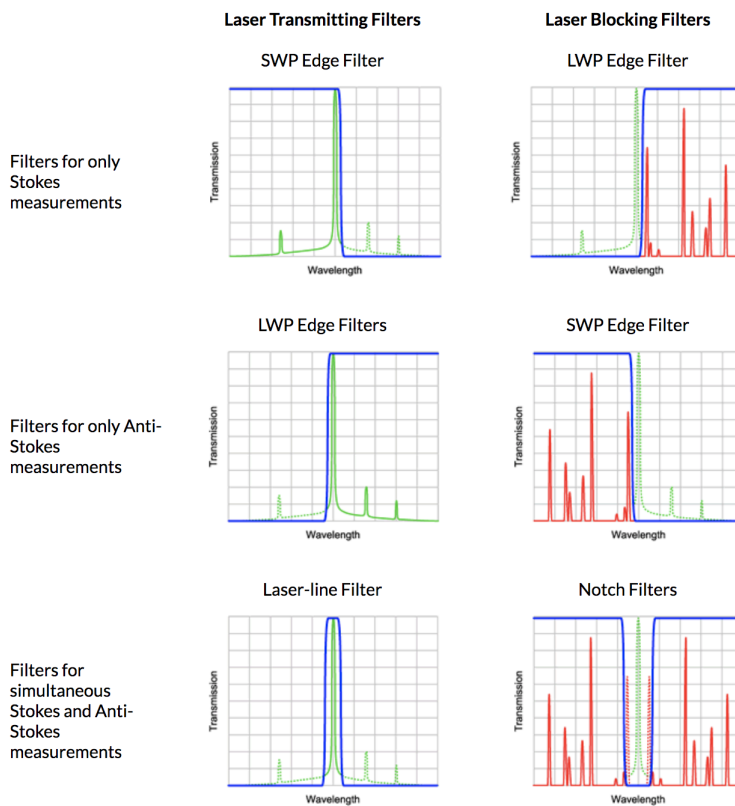
Figure 2.9: Illustration of how different optical filters can be used in a Raman spectrometer. The green lines represents the laser spectrum, blue lines represent the filter transmission spectra, and the red lines represent the Raman signals [16].

2.7.2 Diffraction Grating

The diffraction grating is the optical operation and is considered as an important parameter in spectroscopy, due to its ability to separate (disperse) Raman scatter and used to reduce stray light. This operation is a collection of transmitting elements of light and makes it possible to separate polychromatic light into its constituents monochromatic component [19]. There are several types of grating, and the two most common types are holographic and ruled diffraction grating. Holographic gratings are typically used in Raman spectrometers, as these offer some advantages such as less manufacturing defects in their structure than ruled grating, which results in a decrease of stray light. When the scattered light hits the diffraction grating, it disperses and further projected onto the couple charge detector (CCD) detector (Figure 2.10).

Typical gratings used for Raman spectroscopy vary from low resolution (300gr/mm) to high resolution (1800gr/mm). Besides, more specialized gratings (including 2400gr/mm and 3600gr/mm) are also available but have certain limitations. Spectral resolution is the capability to resolve spectral features and is an important experimental parameter. If the resolution is too high, the total exposure time will be longer than necessary. If the resolution is too low, some spectral information will be lost and prevents correct characterization. Focal length is the distance between the grating and the detector, and increasing this length will lead to an increase of the spectral resolution [15].
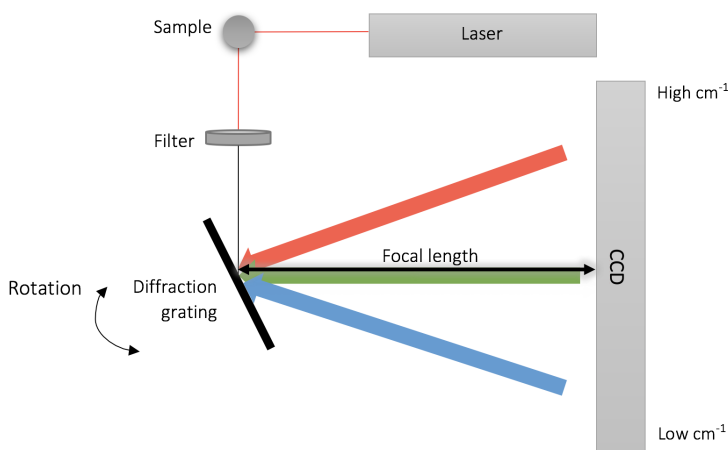
Figure 2.10: Illustration of how the light is illuminated on a sample, dispersed and further projected onto the CCD. Changing the grating or the focal length increases the spectral resolution. The diffraction grating can be rotated to change the color of the light extracted through the slit.

2.7.3 Charged coupled device (CCD)

The scattered light is dispersed using the diffraction grating and is then projected onto a CCD array. The detectors are used for Raman spectroscopy due to its extreme sensitivity to light, and are therefore suitable for analysis of the weak Raman signals. A CCD detector is a silicon based multichannel array detector of various wavelengths, and consist of millions of individual detectors elements. With this multichannel operation, the entire Raman spectrum can be detected in one single acquisition. Each of the elements in the CCD detector interacts with light for the charge to build up. The longer the interaction, and/or the brighter the light, the more charge is registered in the detector. The point of each measured charge reading is then collected. The different elements will each detect light from the corresponding wavenumber, cm^{-1} from low to high edge of the spectrum (Figure 2.10) [15]. The CCD detectors are

quite sensitive to other forms of radiation, which occurs in random events, known as cosmic rays. These may interfere with acquisition of spectra by hitting the detector and introduces sharp and strong features in the resulting Raman spectra [20].

2.7.4 Acquisition time

By adjusting the exposure time and the number of exposures added together, a final spectrum is obtained. The exposure time is analogous to a photographic camera, the longer the exposure time, the better picture in dim light, and therefore a better spectrum from a weak Raman scatter is obtained. The acquisition time is dependent on a number of factors, such as the desired spectral quality, the sample itself, and the Raman spectrometer used. However, a modern Raman spectrometer can acquire a good quality Raman spectra in a few seconds [15].

2.8 *In situ* reactor cell

The Catalytic Cell Reactor, CCR1000 from Linkam is designed to study catalytic reactions at high temperature and pressure. The CCR1000 system consists of a removable ceramic sample holder which is heated by a resistance coil. The samples are placed on a highly porous ceramic fabric filter. The *in situ* cell is connected to a temperature sensor cable, in and out gas lines and circulatory water pump filled with cooled water (15-18 °C), which has a capacity for up to 2 hours operation of the stage at 1000 °C or over. The carrier gas is introduced into the stage via a high pressure valve flowing downwards from top to bottom and heated by the sample holder before passing through the sample which is supported in a ceramic sample holder on a ceramic fabric filter (Figure 2.11a). Most of the parts that are in contact with the sample and carrier gas are usually made of either ceramic or stainless steel, selected for their unreactive properties. The tube of the heater is very narrow to prevent dead space and hot enough, so no condensation of the gas occurs before it is available for gas analysis. The temperature is accurately controlled by the TMS 94 heating stage via a thermocouple. This controller can heat samples at a temperature rate up 200 °C/min with temperature stability of 1 °C and pressure up to 5 bar (with quartz window installed).

(a) Linkam CCR1000 reactor   (b) Stage anatomy of the CCR1000 reactor
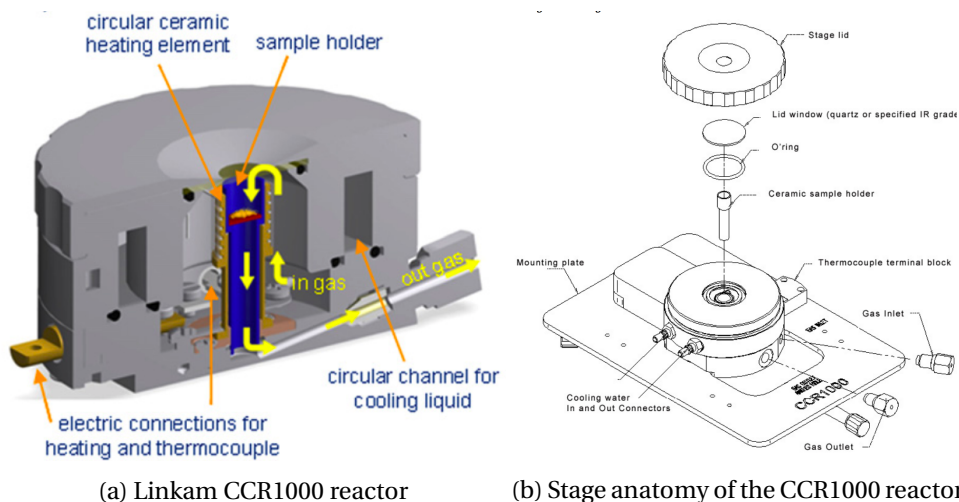
Figure 2.11: Detailed illustration of Linkam CCR100 reactor, stage anatomy and schematic drawing of the sample holder with flow indications by arrows [21].

2.9 Catalyst Characterization

2.9.1 Catalyst preparation

A heterogeneous catalyst is usually prepared by impregnation method by contacting a solid in a solution of a metal salt and inducing deposition. Further, the support is dried to remove the remaining liquid and then calcined. The impregnation method can be classified into two groups, according to the relationship between support pore volume (Vp) and liquid volume (Vimp), which are (1) Dry/Incipient wetness impregnation (2) Wet impregnation. When the volume of the impregnating solution is equal to the pore volume of the support, $V_{imp} \approx V_p$, the impregnation is called dry wetness impregnation, while in wet impregnation the liquid volume is higher than the supported pore volume, $V_{imp} > V_p$ [22].

There are several advantages to this method, such as no production of wastewater and no risk of losing precious precursor. Moreover, the process is mostly used within impregnation of precious metals onto the support [23]. The step after impregnation, the samples are dehydrated by being heated in an oven to the boiling point of the solvent in static conditions or under a flow of gas. The elimination of water increases the concentration of the precursor until saturation and crystallization. Calcination is thermos-chemical treatment step in the formation of a catalyst. During this step, the catalysts are heated at high temperature in the presence of oxygen and convert the supports into the final catalyst by the formation of a strong chemically network.

The purpose of calcination is to induce the solid state reactions to reach the ultimate stability of the material by thermally decompose monoxide precursor and oxidize the supports and remove undesired ligands [22].

2.9.2 Nitrogen adsorption

Nitrogen adsorption is a widely used tool for evaluation of the surface area, pore volume and pore size distribution of porous materials from physisorption isotherm data. This principle of this method involves measurement of the physisorption of nitrogen on a certain amount of material. The uptake of liquid nitrogen is measured at a constant low temperature at -193 °C as a function of nitrogen pressure [24]. Nitrogen can form multilayer adsorption and is usually well described by Brunauer-Emmett-Teller (BET) method. The BET isotherms equation (2.8) is an extension of the Langmuir isotherm and is based on the following assumptions [25]:

- The first layer of adsorbates is taken up with constant heat of adsorption.

- The second layer is characterized by heat of adsorption and is equal to the latent heat of evaporation.

- Consider a dynamic equilibrium between each layer and the gas phase.

By making these assumptions, Brunauer, Emmett and Teller were able to simplify their first and most useful form of equation, expressed by:

$$\frac{P}{V(P_o - P)} = \frac{1}{V_m C} + \frac{C-1}{V_m C} \cdot \frac{P}{P_o} \tag{2.8}$$

Where P is the pressure of nitrogen, V is the volume of nitrogen gas adsorbed, P_o is the saturated vapour pressure of the liquid at the operating temperature, V_m is the volume equivalent to an adsorbed monolayer and C is the BET constant [25]. The application of the BET method can be divided into two stages. Firstly, by plotting $\frac{P}{V(P_o - P)}$ against $\frac{P}{P_o}$ will give a linear relation with a slope equal to $\frac{C-1}{V_m C}$, and an intercept equal $\frac{1}{V_m C}$. The plot of this yield both the BET constant and the volume of the adsorbed monolayer. The second stage involves the calculation of the specific surface area, S_{BET}, from V_m. This evaluation is dependent of the average area, σ_{N_2}=0.162 nm^2 [23], which is a value based on the assumption proposed by Emmet and Brunauer, that the monolayer had the liquid form of close-packed structure [26]. The following equation can then calculate the total surface area:

$$S_{BET} = V_m \cdot L \cdot \sigma_{N_2} \tag{2.9}$$

Where the L is the Avogadro constant. The most widely used method to determine pore volume and pore size distribution are the Barrett, Joyner and Halend (BJH) method. This method is based on physisorption isotherm using adsorption-desorption techniques and should be determined over a wide range of relative pressure while allowing a slow reach of equilibrium at very low pressure [26].

2.9.3 CO Chemisorption

Chemisorption is one of the most important characterization techniques to determine the dispersion of metal in supported catalyst by using adsorption isotherms. Adsorption is a result of a chemical bond formed between the adsorbent and the adsorbate in a monolayer on the surface [23]. The dispersion of the metal is defined as:

$$D = \frac{\text{Number of metal atoms deposited on the surface}}{\text{Total number of metal atoms}} \tag{2.10}$$

Dispersion can be obtained by measuring the amount of gas adsorbed on a sample given that the adsorption stoichiometry is known. There are some various gases that can be used as adsorbate for chemisorption, but the most common ones are H_2, CO and O_2. The advantages of CO and O_2 as adsorbates is less chance of dissolution and low adsorption on oxide carrier, respectively. Ideally, the adsorbate gas should adsorb irreversibly, and hence have no or minimum adsorption on a support material. Choosing the adsorbate gas depends on nature of the metal and the working conditions. Adsorption isotherms are obtained by increasing pressure and determining the quantity of the reactive gas adsorbed while the catalyst is maintained at constant temperature. To calculate the quantity amount of gas adsorbed at monolayer coverage, a common practice is shown in Figure 2.12, showing that the isotherm is extrapolated back to zero pressure. The metal surface and metal dispersion are given by following equations [23]:

$$A = \frac{v_m}{22414} L \frac{n}{m} a_m \frac{100}{wt} \tag{2.11}$$

$$D = \frac{v_m n}{22414 m} / \frac{wt}{100M} \tag{2.12}$$

where, A is the specific metal surface area, v_m is expressed in cm^3 (STP), L is the Avogadro's number (6.022×10^{23} mol^{-2}), n the chemisorption stoichiometry, m the mass of the sample (g), a_m the surface area (m^2) occupied by a metal atom and wt (%) the metal loading and M is the atomic mass of the metal.
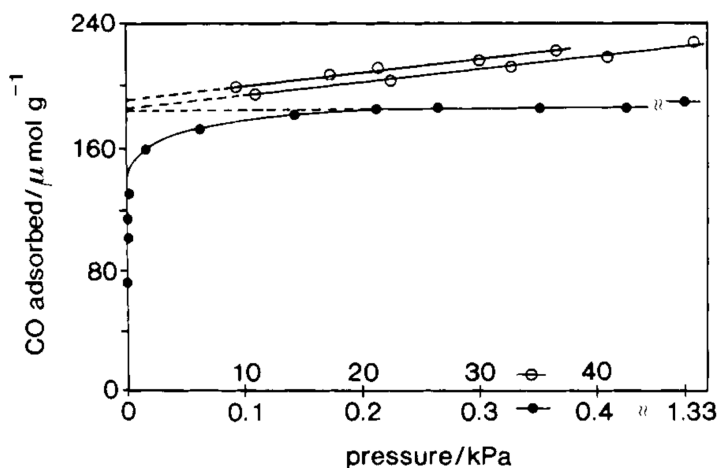
Figure 2.12: Illustration of the isotherms for the adsoprtion of CO on EUROPT-I Pt/SiO$_2$ at ambient conditions from a pressure range 0-1.33 kPa and 10-50 kPa [23].

2.9.4   X-Ray Diffraction (XRD)

X-ray diffraction is one of the oldest and most used characterization techniques in catalysis. This technique involves estimation of crystallite size and identification of crystalline phases inside catalysts. X-ray diffraction patterns are generated by illuminating the crystalline sample with a monochromatic beam of X-rays, which is then diffracted by the atoms. When the scattered monochromatic X-rays are in phase with each other, constructive interference is created and can be explained by Bragg's relation, as shown in Figure 2.13. This relation can be used to calculate the lattice spacing, allowing a further investigation of the crystalline phase [24]:

$$n\lambda = 2d \, sin\theta; \quad n = 1, 2, ... \tag{2.13}$$

where n is an integer also called the order of the reflection, λ is the wavelength of the X-rays, d is the distance between two lattice planes, θ is the angle between the incident X-rays and the normal to the reflecting lattice plane.
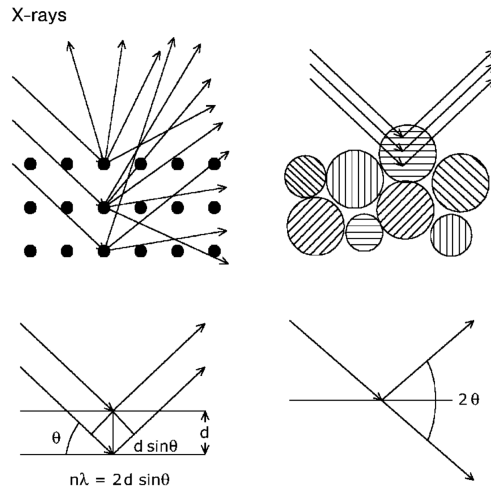
Figure 2.13: Illustration of constructive interference of scattered X-rays by atoms in a periodic lattice explained by Bragg's law [24].

By complementing the X-ray diffraction pattern of the crystalline sample with line broadening of the peaks, the crystallite size can be estimated. However, it has an important limitation. A clear diffraction peak of a sample is dependent of sufficient long-range order. The width of the peak carries information about the dimensions of the reflecting planes. The relationship between the width of the peak and the crystallite size can be expressed by Scherrer formula [27]:

$$< L > = \frac{K\lambda}{\beta cos\theta} \tag{2.14}$$

where $< L >$ is a measure for the dimension of the particle in the direction perpendicular to the reflecting plane, K is a constant often taken as 0.9, λ is the wavelength of the X-ray, β is the peak width and θ is the angle of the diffraction peak.

2.9.5 Temperature Programmed Reduction (TPR)

Temperature programmed reduction is a widely used characterization method that allows monitoring of hydrogen consumption of a reducible catalyst as a function of temperature. In a typical TPR experiment, a fixed bed reactor charged with catalyst is exposed to a specific flow rate of reducing gas mixture, while the temperature is set to increase linearly with time. A typical heating rate ranges from 0.1 to 20 °C min^{-1} [24]. The gas composition at the outlet of the furnace is monitored by quantitative techniques, either by a mass spectrometer (MS) or a thermal conductivity detector (TCD) [28]. A graphical representation of hydrogen consumption of a catalyst is recorded against temperature and shows as a reduction profile. The reduction profile can either be a single step or multiple steps. The reduction of metal oxides in a single step can be expressed by [24]:

$$MO_n + nH_2O \rightarrow M + nH_2 \tag{2.15}$$

The reduction processes are quite complex, TPR results are therefore typically discussed in qualitative manner [23]. The most important information obtained from the TPR plot is the temperatures at which complete reduction of the metal oxide occurs. However, the area under the TPR curve can also be calculated by integration, which is the total consumption of hydrogen gas during the reduction process.

By doing a pulse calibration of the TCD signal, a known amount of hydrogen consumption can be calculated. A known amount of hydrogen is used during the reaction to obtain a reference area on the TPR profile. The area under the TPR profile is then integrated and the amount of hydrogen gas consumed during the analysis is generated.

Chapter 3

Experimental

3.1 Catalyst preparation

Catalysts with 5 wt% platinum on γ-alumina support (Pt/Al$_2$O$_3$) and zirconia support (Pt/ZrO$_2$) were prepared by one step incipient wetness impregnation of γ-Al$_2$O$_3$ and ZrO$_2$ support (53-90 μm) with aqueous solutions of platinum(IV)nitrate, Pt(NO$_3$)$_4$. Prior to impregnation the catalysts support gamma alumina, γ-Al$_2$O$_3$ and zirconia, ZrO$_2$ were calcined at 600 °C for 2 hours at a ramp rate of 10°C/min.

The incipient wetness point of γ-Al$_2$O$_3$ and ZrO$_2$ support was estimated by drop wise addition of deionized water. The wetness point was used to calculate the amount of platinum nitrate precursor needed to give 5 wt% Pt. The precursor was further prepared and stirred until it was homogenized and drop wise added to the support. Impregnated samples were dried in a ventilated oven at 120 °C overnight. It was stirred every quarter in the first hour and every half an hour in the second hour. The dried sample was transferred to a fixed bed quartz reactor and calcined in air flow at 600 °C for 2 hours with a temperature ramp of 10 °C/min.
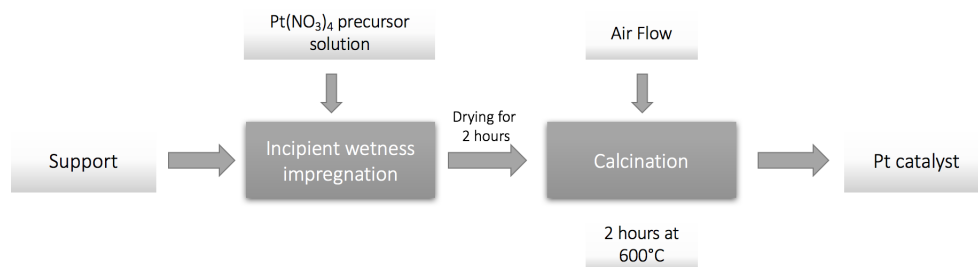
Figure 3.1: Block diagram of preparation of the two synthesized catalysts.

3.2 Catalyst characterization

The two synthesized catalyst, 5wt.% Pt/Al_2O_3 and 5wt.% Pt/ZrO_2 were characterized by CO chemisorption, nitrogen adsorption, temperature programmed reduction, X-ray diffraction and Raman spectroscopy.

3.2.1 Nitrogen Adsorption

BET surface area was measured by adsorption of liquid nitrogen at a temperature i.e -196 °C, using a Micromeritics TriStar II 3020 instrument. Prior to measurements, the samples were weighted to be around 60-80 mg and placed into the instrument sample glass tube, and further degassed at 200 °C overnight. The sample is completely degassed when the pressure is 100 torr or less and ready for analysis. After degassing, the sample tube was cooled down to room temperature and weighed again in case there is a decrease in weight during the degassing process. The nitrogen adsorption isotherm was obtained, and the BET surface area was calculated in according to the procedure mentioned in section 2.9.2

3.2.2 CO Chemisorption

Dispersion of active metal for different samples was measured using a Micrometics ASAP-2010N unit 1 instrument. A small amount of quartz wool was first loaded into a U-shaped quartz reactor, and approximately 100 mg of catalyst was introduced before the second layer of quartz wool was inserted. The quartz reactor was further mounted to the apparatus, and the temperature of the catalyst bed was monitored using a thermocouple placed outside the reactor at the same height as the catalyst. The reactor was then placed inside an electric furnace. The samples were first evacuated for at least two hours before a manual leak test was performed. This is to ensure that all the gases adsorbed on the surface are evacuated and the minimum pressure change did

not surpass more than 50 μHg/min.

After passing the leak test, the automatic analysis sequence was then started. The samples were first evacuated at 100 °C for 30 minutes in helium. The temperature was increased to 450 °C at a ramp rate of 10°C/min in a continuous flow of hydrogen for reduction of the catalyst. After the reduction, the samples were evacuated again for 30 minutes at 450 °C and cooled down to 35 °C. A leak test was then performed at 35 °C before an evacuation for 30 minutes at 35 °C, followed by an analysis step with carbon monoxide gas at 35 °C. The analysis sequence of the CO chemisorption with analysis conditions are summarized in Table 3.1.

Table 3.1: CO Chemisorption Analysis Conditions and Sequences.

Task Number	Analysis Step	Gas	Temperature [°C]	Time [min]
1	Evacuation	He	100	30
2	Flow	H_2	100	5
3	Flow	H_2	450	120
4	Evacuation		450	30
5	Leak Test		35	
6	Evacuation		35	30
7	Analysis	CO	35	

3.2.3 X-Ray Diffration (XRD)

The X-Ray Diffraction was measured using a Bruker D8 Advanced DaVinci X-Ray Diffractometer - D8 DaVinci 1 with CuKα radiation apparatus to obtain the XRD profiles spectra. The catalysts were prepared in the sample holders, with a chosen 2θ angles ranged from 15° to 105° with 15 seconds steps in 30 minutes with slit opening set to V6.

3.2.4 Temperature Programmed Reduction (TPR)

Temperature programmed reduction profiles for the catalysts were carried out using a Altamira Benchcat Hybrid-1000HP instrument. A layer of quartz wool was first loaded into a U-shaped quartz reactor and approximately 100-250mg catalyst was then introduced before the second layer of quartz wool was inserted. The quartz reactor was mounted in the apparatus, and a leak-test was performed using a reducing agent of 7% H_2/Ar gas mixture with a flow rate of 75mL/min. After passing the leak-test, an electric furnace was installed and the temperature of the catalyst bed was monitored using a thermocouple inserted in the reactor. The TPR was performed

using 7% H_2/Ar gas mixture by heating up to 800°C at a temperature rate of 10°C/min. A thermal conductivity detector was used to measure the consumption of hydrogen as a function of temperature.

3.3 Raman spectroscopy

The experiments on the selected catalyst were done with the Raman spectrometer, Horriba Jobin Yvon LabRam HR800 confocal microscope equipped with an internal laser of He-Ne (633 nm) and an external laser He-Cd (325 nm). The catalysts studied with Raman spectroscopy were 5wt.% Pt/Al_2O_3 and 5wt.% Pt/ZrO_2. The instrument was calibrated with a monocrystalline silicon sample before measurements. All *in situ* experiments were conducted using a Linkam TMS 94 temperature heating stage.

3.3.1 Calibration with silicon

Before acquiring a spectrum the instrument was calibrated with silicon sample. Monocrystalline silicon has a very strong peak at 520.7 cm^{-1} and is therefore ideal for calibration grid motor of Raman spectrometer. The calibration procedure of the instrument was followed by Horiba Jobin Yvon LabRAM HR800 manual [29]. This is a simple procedure involving two software parameters, zero and koeff. Zero is the number used to define the position of the zero order of the spectrum and can be seen as the number of motor steps to move away from the calibration sensor. Koeff is the number of nm moved. The Raman parameter used were 200 in hole size, D06 filter, 600 gr/mm grating and 50x objective.
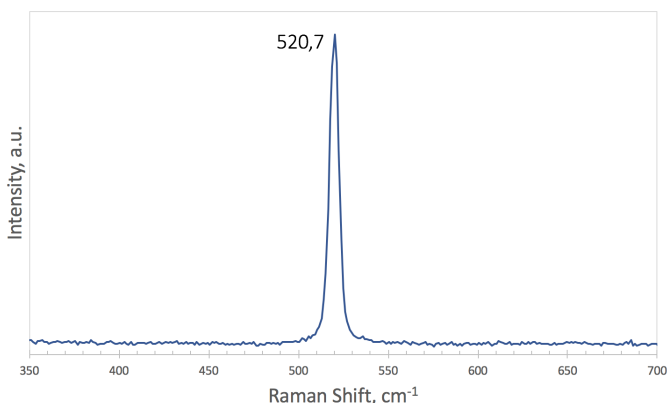
Figure 3.2: Calibration of Raman spectrometer with silicon shows a strong peak at 520.7 cm^{-1}.

3.3.2 Sample preparation for *in situ* cell

A small disc of the sample filter in the sample holder was needed to place the sample on. This filter fabric came as a sheet of alumina/silica (Al_2O_3 96%/SiO_2 4%) Non-Woven Fabric. When the filter was correctly pressed into position in the sample holder, it was then ready to load a sample into the sample holder using a sample loading base. The sample holder can then be carefully loaded into the heater assembly, CCR1000 Catalyst cell reactor. It was rotated to make sure that it was axially aligned with the cell. Once the sample holder was positioned and firmly in place, a quartz window (22x1mm) was placed over the sample holder, and then closed the cell with the lid.

3.3.3 Temperature calibration

Temperature calibration was executed in the specialization prior to this thesis, and validated with literature. The cubic boron nitride (c-BN) was used as the temperature calibrator for this experiment and was in the form of a powder of small crystallites. The experiment was carried out at atmospheric pressure to determine the temperature dependence of Raman frequency of c-BN up to 600 °C. The c-BN powder was loaded into the fixed bed reactor, CCR1000 , and heated up to 600 °C. The reactor was fed with synthetic air with a flow rate of 20mL/min. The Raman spectra were acquired every 50 °C and cooled down with a rate of 20 °C/min.

A 50x microscope objective was used for excitation and collection of Raman signal. The scattered photons were dispersed over a 600 gr/mm holographic transmission grating and collected on a cooled CCD detector. The confocal hole for the laser was set to 150 μm and the filter size was D06. The spectra were collected with an acquisition time of 100 seconds with an accumulation number of 3, and was measured from a wavenumber of 700 cm^{-1} to 1300 cm^{-1}.

In each experimental runs, the sample was heated to measure the shift of the TO mode of c-BN, and the Raman spectra were acquired at 300K, 573K and 873K. Figure F.1 shows the shift of the TO mode when heating the sample. An increase in temperature causes the peak, TO mode to shift to a lower wavenumber.
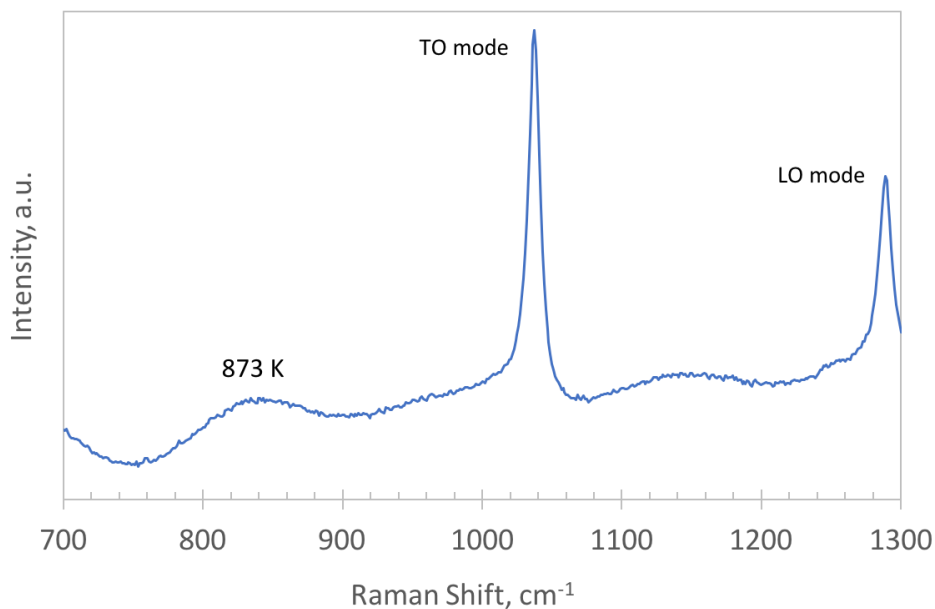
Figure 3.3: Raman spectrum of c-BN at atmospheric pressure and 873K in the region of 700-1300 cm^{-1}. Two intense peaks, which corresponds to the TO and the LO mode were identified at high temperature.

3.3.4 *Ex situ* measurement

The Raman spectra for the samples were recorded by projecting a continuous wave laser of He-Ne laser (633 nm) and He-Cd laser (325nm) through the samples under ambient conditions and collected between 100 and 1000 cm^{-1}. A 50x and 15NUV microscope objective was used for excitation of 633nm and 325nm laser, respectively. The scattered photons were dispersed over a 600 and 1800 gr/mm holographic transmission grating and collected on a CCD detector. The confocal hole for the laser was set to 200 μm and the filter size varied from D06 to D1. The spectra were collected with an acquisition time of 100 seconds with an accumulation number of 3. Both Labspec 5 and 6 were used, due to some technical error with the software. The only difference between the two software is that Labspec 6 has an auto calibration function, while in Labspec 5 the calibration was manually done. It is, therefore, not a significant deviation.

3.3.5 *In situ* measurement

An oxidation-reduction process by doing an oxidation, reduction and further a reoxidation of the sample was further investigated for 5wt.% Pt/ZrO$_2$ to form the desired product. All the *in situ* measurements were carried out using a quartz window cell in the reactor. The procedure for the *in situ* measurements, showing the temperature profile against the time used for one experiment is presented in Figure 3.4. The Raman parameter used were a confocal hole of 200 μm, D1 filter and an acquisition time of 100x3.

The Raman spectra for 5wt.% Pt/ZrO$_2$ of the *in situ* measurements were heated from room temperature to 500 °C using a heating ramp of 10 °C/min, and the gas oxidizer employed was a mixture of 7% O$_2$/Ar with total flow rate of 40 mL/min. The Raman spectra were continuously acquired every 100 °C, held for 2 hours and further flushed in argon before switching over to a reducing agent, 7% H$_2$/Ar at a temperature of 500 °C. The sample was reduced for two hours, flushed in argon and further cooled down to room temperature with a temperature rate of 20 °C/min.

After the sample was cooled down to room temperature, it was then reoxidized and heated up to a temperature of 500 °C with a heating ramp of 10 °C/min, the gas oxidizer employed was a mixture of 7%O$_2$/Ar with a flow rate of 40mL/min, controlled with their respective mass flow controllers. The Raman spectra were acquired every 100 °C, held at 500 °C for 2 hours and further cooled down to room temperature in the same gas mixture.
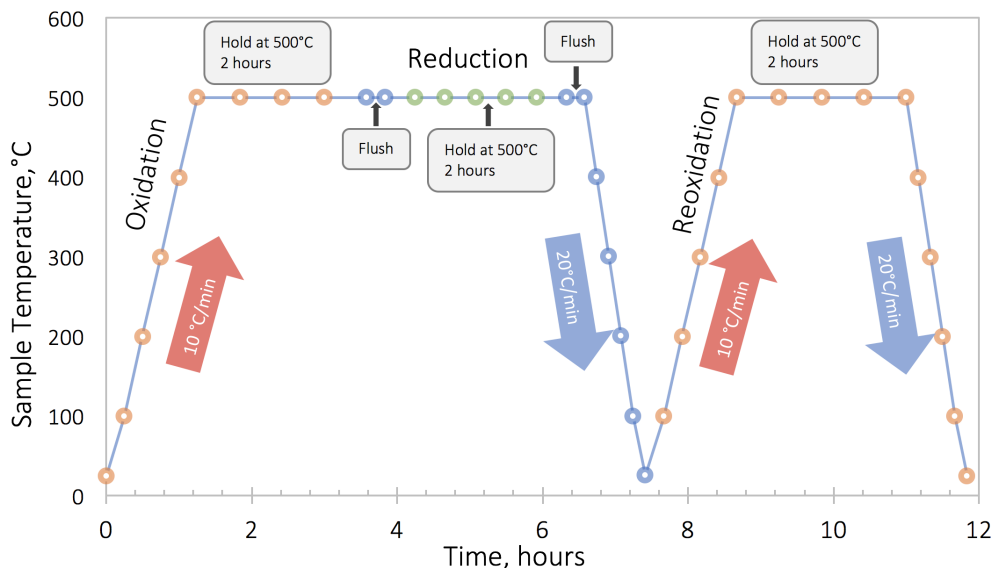
Figure 3.4: Temperature profile used for the *in situ* measurements. The sample is first heated up by oxidation 7%O_2/Ar, held for two hours and further flushed with Argon. It is then switched to a reducing agent, 7%H_2/Ar to reduce the sample at a temperature of 500 °C for two hours and flushed with argon. Furthermore, the sample is then reheated by reoxidation in 7%O_2/Ar and held for two hours before cooling down to room temperature. The orange, blue and green circles denote the Raman measurements point under oxidizing, inert and reducing conditions.

3.4 Experimental set-up

The set-up for the *in situ* cell Raman spectrometer consists of three main parts, illustrated as green, blue and red dotted lines in Figure 3.5. The green lines show how the signals are connected to the computer, while the red lines illustrate how the gas lines are connected to each other. The blue lines show the Raman spectrograph box consists of three different lasers, which are near UV-light, visible light and near infra-red with a wavelength of 325, 633 and 785nm, respectively. A detailed illustration of the inside of the Raman box is shown in Figure 3.6. Showing how the lasers irradiate a sample through the objective and onto the *in situ* cell. The scattered photons are further collected with a CCD detector, which is placed beside the Raman spectrometer and sends the signal to the computer where the spectrum is displayed. The *in situ* cell is connected to a water pump for cooling, in and out gas connection. The gases argon, hydrogen and air are controlled by their respective mass flow controllers (MFC) using National Instruments LabVIEW control written by Samuel K. Regli for control of MFCs.
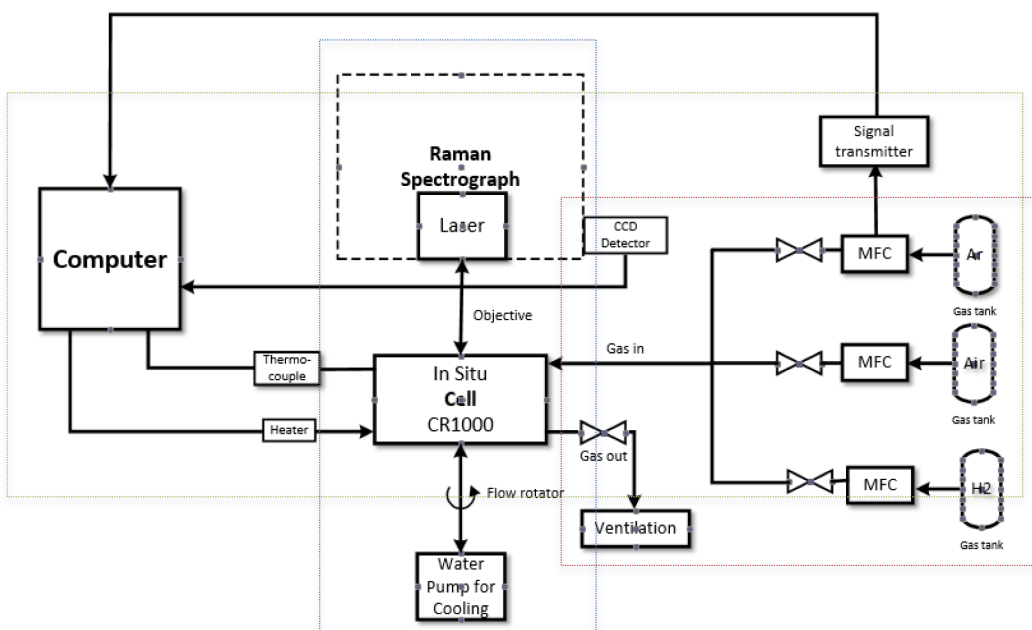
Figure 3.5: Schematic set-up of the *in situ* Raman spectroscopy. The blue lines show how the Raman box is connected to the *in situ* cell. The green lines show how the signals are connected to the computer, while the red lines illustrated how the gas lines are connected to each other. Three gases, argon, air and hydrogen are connected to the *in situ* cell and controlled with the respective mass flow controllers.
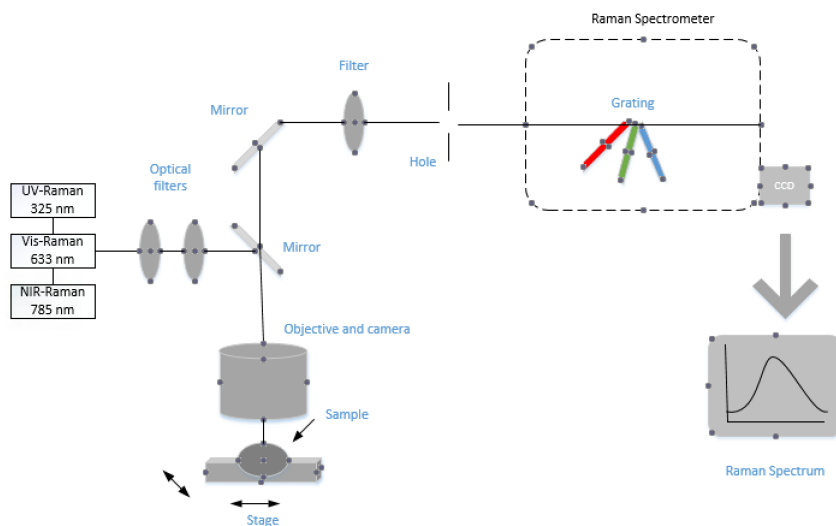
Figure 3.6: Illustration of the Raman spectrometer principle. A laser is beamed onto the sample and the optical filters block out the Rayleigh scattering, and only Raman scattering passes through. A CCD detector detects the Raman scattering and transforms the light into a spectrum.

Chapter 4

Results and Discussion

4.1 Catalyst Characterization

The characterization results of the two synthesized catalyst, 5wt.% Pt/Al_2O_3 and 5wt.% Pt/ZrO_2 are given in the following sections. The results of the same catalysts, containing different amount of Pt, 1wt.% Pt/Al_2O_3 and 1wt.% Pt/ZrO_2, provided by Ata ul Rauf Salman are also included for comparative purposes.

4.1.1 Nitrogen Adsorption

Table 4.1 shows the BET surface area, pore volume and average pore width for 5wt.% and 1wt.% Pt catalysts. The Micromeritics instrument summary reports including isotherms plot of the two prepared catalysts have been attached to Appendix B.

The alumina supported catalyst with 5wt.% has the highest BET surface area at 144 m^2/g while the zirconia has the lowest at 70 m^2/g , but larger pore diameter. As seen in Table 4.1 the surface area and pore volume of alumina supported platinum catalysts were measured to be within the range of other studies [30]–[33].The zirconia supported platinum catalyst was measured to be within the range of other studies as well [34], [35]. In general, the surface area is expected to decrease with increasing metal loading, however, it is not notably changed upon increasing the metal loading for this case. It is well known that the surface area for γ-alumina support is around 145 m^2/g, and the small increase of the metal loading may therefore not have any effect. The minor observed deviations of the alumina could be due to the measurement uncertainty.

Table 4.1: Surface area, pore volume and average pore width of both Pt/Al_2O_3 and Pt/ZrO_2 with two different loading, 5wt.% and 1wt.%. The calculation of pore volume and pore width are based on BJH desorption method.

Catalyst	BET Surface Area $[m^2/g]$	Pore Volume $[cm^3/g]$	Avg. Pore Diameter [nm]
5wt.% Pt/Al_2O_3	144*	0.36	9.2
1wt.% Pt/Al_2O_3	141	-	-
5wt.% Pt/ZrO_2	70	0.28	11.2
1wt.% Pt/ZrO_2	-	-	-

* Calculated manually using selected points from the BET surface area plot. The calculations are shown in Appendix B.

4.1.2 Dispersion

Table 4.2 shows the dispersion and crystallite size calculated from CO chemisorption performed for 5wt.% and 1wt.% Pt catalysts. Summarized instrument reports including isotherm plots of the two synthesized catalysts have been attached to Appendix C.

Table 4.2: Dispersion and crystallite size of both Pt/Al_2O_3 and Pt/ZrO_2 with two different metal loading, 5wt.% and 1wt.%. The calculations are based on CO chemisorption.

Catalyst	Dispersion [%]	Crystallite size* [nm]
5wt.% Pt/Al_2O_3	36	2.3
1wt.% Pt/Al_2O_3	18	4.6
5wt.% Pt/ZrO_2	52	1.6
1wt.% Pt/ZrO_2	50	1.6

* Calculated using $d_p = \frac{0.821}{D\%}$ [36].

As seen in Table 4.2 the dispersion values for zirconia supported catalyst are higher than for alumina supported catalysts. In principle, this fact could indicate that the interaction between the metallic precursor and the zirconia support is much higher compared with supports based on alumina [35]. The crystallite size estimated by CO chemisorption is much smaller than that estimated from XRD profiles in section 4.1.3. The crystallite size from the CO chemisorption was estimated to be ~2nm for the higher loading catalysts, while the estimated crystallite sizes from XRD are >7nm. This observation shows that both small and large crystallites are present in the catalyst. However, chemisorption and XRD line broadening do not necessarily

result in the same estimation. It should, however, be noted that they are not directly comparable since it is two different measurement. Besides, chemisorption is a surface-area-average measurement while line broadening is a volume-averaged based measurement [37]. Another thing to notice that in CO chemisorption a reduction treatment was done prior to the CO analysis, which is not done for XRD. It does however, indicate that both small and large crystallites are detected by chemisorption and XRD analysis, respectively. This could be explained by the fact that diffract X-Ray are only able to identify crystallites larger than >5nm [37].

4.1.3 X-Ray Diffraction (XRD)

Figure 4.1 and Figure 4.2 shows the XRD profiles of the two synthesized catalysts. The suggested crystalline phases of the catalyst are matched to reference patterns using the DIFFRAC. EVA V4.1 software, and have been attached to Appendix E. No experimental data were generated for 1wt.% catalysts due to the low metal loading which can not be detected by the instrument.
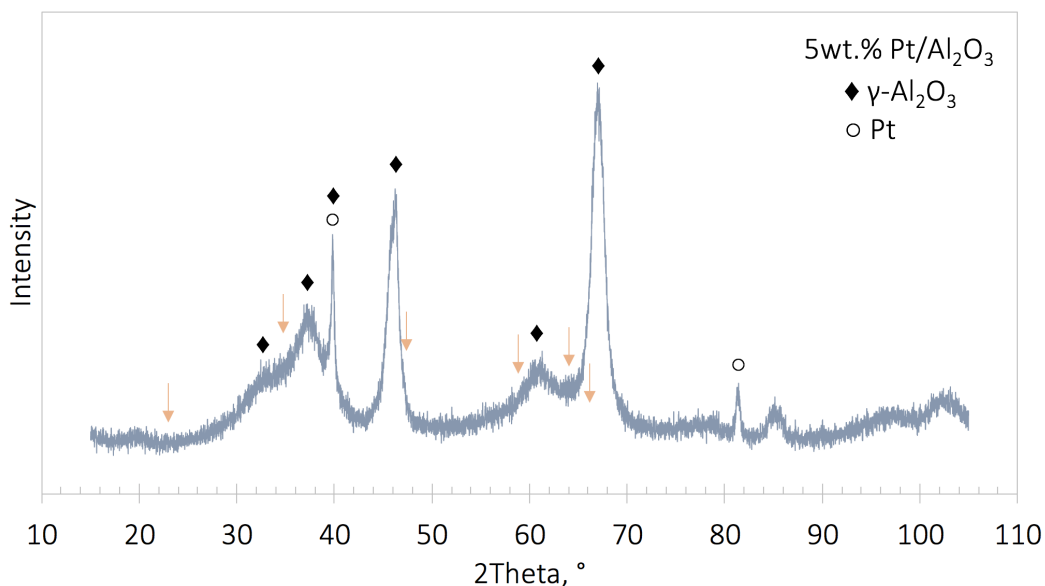
Figure 4.1: XRD profile of 5wt.% Pt/Al_2O_3. The ♦ and the ◯ denotes γ-Al_2O_3 and Pt peaks, respectively. The orange arrows denotes the suggested reference patterns for PtO_2 using the DEFFRAC. EVA V4.1 software.

The XRD profile of 5wt.% Pt/Al$_2$O$_3$ in Figure 4.1 shows peaks at 32°, 42°, 40°, 46°, 61°, 67.5° and 81.2°. The γ-alumina phase matches well with the diffraction peak, being identified at the major peaks. The suggested peak fitted for Pt is also observed at 40° and 81.2° which is in accordance with previously conducted studies [32], [33], [38]. However, no peaks fitted for PtO$_2$ are observed, which can be expected at 33.3° and 55.9° [38]. At around 40 degrees region it is observed that the spinel reflections of platinum are overlapping with that of alumina, which indicates that both alumina and Pt are present in the XRD profile. However, it is observed that the alumina peak dominates the Pt peak, it can, therefore, be seen as an overlapped Pt diffraction peak with a contribution of alumina, since it is clear that the major peaks belong to alumina peaks. The presence of detected platinum phase for the 5wt.% catalyst at 81.2 ° is quite crystalline with a crystallite size of 26.5nm. This could hence indicate that the catalyst contains both small and large particles, as discussed in the previous section. The estimated crystallite size from the XRD data is shown in Table 4.3.
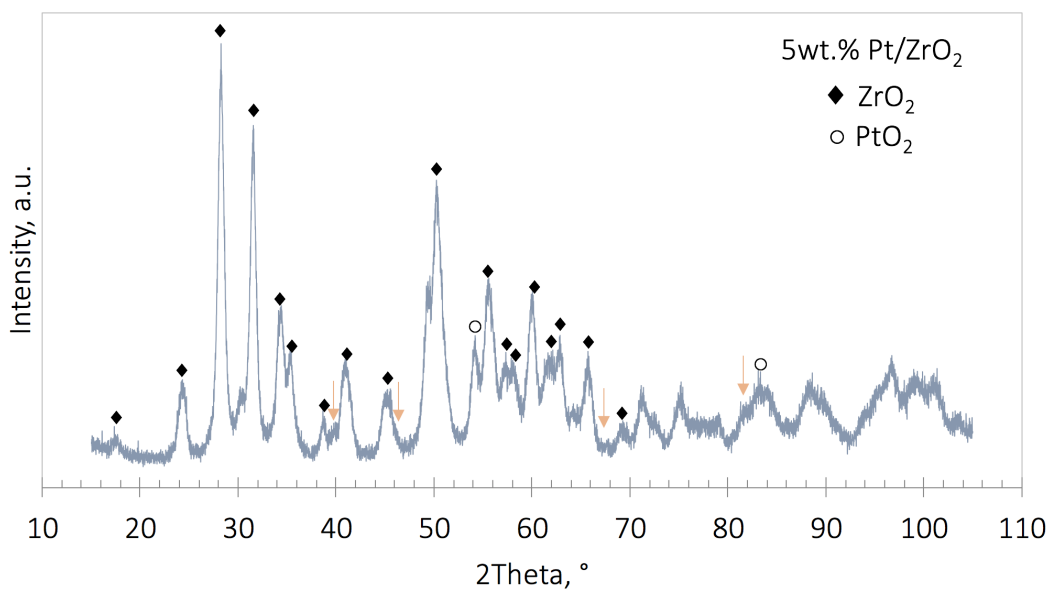
Figure 4.2: XRD profile of 5wt.% Pt/ZrO$_2$. The ◆ and the ◯ denotes ZrO$_2$ and PtO$_2$ peaks, respectively. The orange arrows denotes the suggested reference patterns for Pt using the DEFFRAC. EVA V4.1 software.

The zirconia phases match pretty well with the suggested reference diffraction peaks as shown in Figure 4.2, being identified at all the major peaks. No Pt species could be detected for this catalyst. However, the absence of Pt peaks in the XRD profile for zirconia supported catalyst could hence indicate the presence of finely dispersed platinum particles compared to alumina supported Pt. This is in compliance with the

CO chemisorption results in Table 4.2, showing higher dispersion and smaller crystallite size for zirconia. The absence of Pt in the XRD profile could be explained by that it is probably attributed to the metal loading being low or overlapping of zirconia diffraction peaks.

The peaks fitted for PtO_2 in the XRD profile of zirconia supported catalyst are observed. Some of the suggested peaks are present nearly at the same angles as some of the identified zirconia peaks, indicating dominance of zirconia peaks, making the phase identification difficult. The suggested peaks of PtO_2 which are not overlapped by zirconia peaks are observed at 83.5 °, which is notable broad compared to the other peaks. The XRD peak width is inversely related to the crystalline size [37], i.e., the smaller crystallite size, the broader the XRD. This is in compliance with the crystallite size estimated from XRD data presented in Table 4.3. Compared to the alumina based catalyst, the estimated crystallite sizes are noticeably larger than for zirconia based catalyst, which is reflected by the narrow Pt peaks in the XRD profile 5wt.% Pt/Al_2O_3. For the sake of simplicity, particle sizes are referred to crystalline sizes in the following sections.

Table 4.3: Crystallite sizes of Pt and PtO_2 of 5wt.% Pt/Al_2O_3 and 5wt.% Pt/ZrO_2.

Catalyst	Crystallite sizes[nm]	
	Pt	PtO$_2$
5wt.% Pt/Al$_3$O$_3$	26.5	
5wt.% Pt/ZrO$_2$		7.3

4.1.4 Temperature Programmed Reduction (TPR)

The TPR profiles obtained for the two synthesized catalysts are presented in Figure 4.3 and Figure 4.4. The experiments were carried out with 7% H_2/Ar gas in order to find the optimal reduction temperature and to investigate the reducibility of the catalysts. No experimental data were generated for 1wt.% catalysts due to the low metal loading which can not be detected by the instrument. For the alumina supported Pt catalyst, two TPR profiles with two different loading of catalyst were generated. The TPR profile with a catalyst loading of 100mg has been attached to Appendix D.

Figure 4.3 shows TPR profile of 5wt.% Pt/Al_2O_3 with a catalyst loading of 250mg, measured from ambient temperature to 800°C. The reduction peaks for the higher sample loading of catalyst are much more distinct compared to the lower loading of the catalyst. This could, however, be explained by the low degree of reduction of the catalyst,

and therefore, a higher loading of catalyst sample must be used. Furthermore, a larger detection region will greatly enhance the signal. The observed dips in the TPR curve can either be explained by a low sampling rate or alternatively the number of data points. The alumina based catalyst showed two reduction peaks at 150°C and 375°C, which is in agreement with literature [30], [31], [39]–[41]. The reduction peak near 150°C is due to the reduction of the surface PtO_x species, while the peak around 375°C is due to the interaction between the PtO_x and the support [31], [42].
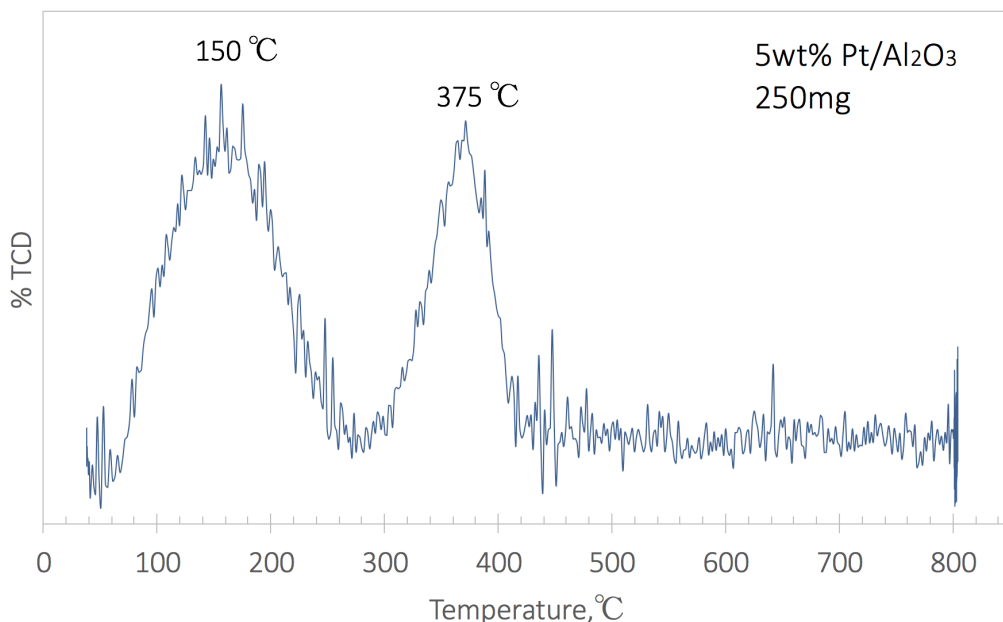
Figure 4.3: TPR profile of 5wt.% Pt/Al_2O_3 with a loading of 250mg catalyst. TPR profile measured from ambient temperature to 800 °C, showing two reduction peaks at ~150 °C and 375 °C.

Figure 4.4 shows the TPR profile of 5wt.% Pt/ZrO_2 with a loading of 100mg catalyst. Two reductions peaks at 150°C and 320°C are shown by the TPR curve and measured to be within the range of other studies [35], [42], [43]. The first reduction peak at 150°C which according to literature data would be assigned to the reduction of PtO_2 interacting weakly with the support. The second peak at 320°C is possibly assigned to the reduction of platinum oxide interacting strongly with the support [35], [42], [43].

150 ℃

320 ℃

5wt% Pt/ZrO$_2$
100mg

% TCD
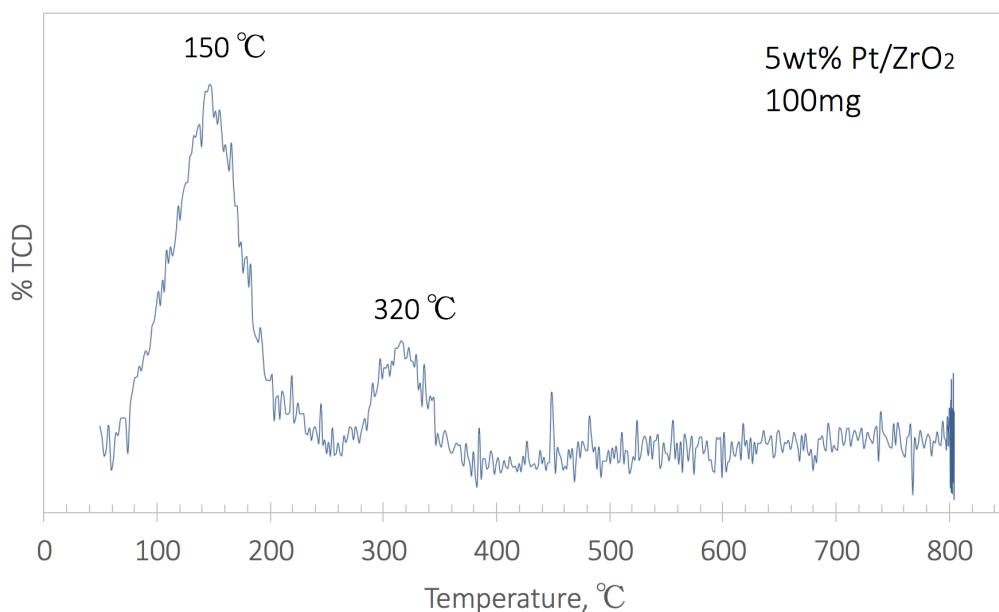
Temperature, ℃

Figure 4.4: TPR profile of 5wt.% Pt/ZrO$_2$ with a loading of 100mg catalyst. TPR profile measured from ambient temperature to 800 °C, showing two reduction peaks at ~150 °C and 320 °C.

The reducibility of the surface PtO$_x$ species was assessed by integrating the reduction peaks from the TPR curve by pulse calibration method. Table 4.4 shows the calculated hydrogen consumption for the two synthesized catalyst. Summarized reports obtained after the hydrogen consumption was calculated and have been attached to Appendix D.

Table 4.4: Hydrogen consumption and % reduction obtained by pulse calibration from H$_2$-TPR curve.

Catalyst	H$_2$ Consumption [μmol/g]	Reduction [%]
5wt.% Pt/Al$_2$O$_3$ (250mg)	72	28
5wt.% Pt/Al$_2$O$_3$ (100mg)	65	26
5wt.% Pt/ZrO$_2$(100mg)	139	54

Koo et al. [31], studied the reducibility of Pt/Al_2O_3 with two different preparation method and reported that catalyst with higher metal dispersion and low-temperature reducibility would exhibit better reducibility. A similar explanation could be given in this case. As shown in Table 4.2 the dispersion for zirconia based catalyst is higher than that is for alumina based catalyst. In addition, the reducibility temperature of alumina based is also a bit higher than for zirconia based catalyst, whereas, the calculated H_2 consumption for 5wt.% Pt/ZrO_2 is about twice as much as that is of 5wt.% Pt/Al_2O_3. Furthermore, according to Koo et al., it could then indicate that zirconia supported catalyst can exhibit better reducibility of PtO_x species.

It is observed two reduction peaks in the TPR profile for the alumina supported catalyst, which is according to literature assigned to the reduction of PtO_2, which means that PtOx species should be present in the alumina based catalyst too, although there were no PtOx peaks identified in the XRD profile. This could most likely indicate that the catalyst contains small amounts of Pt and PtO_2. Furthermore, the low H_2 consumption could indicate that Pt is not fully reduced, besides, this is also reflected by the calculated % reduction in Table 4.4. Zirconia however, exhibits better reducibility, but due to the high dispersion combined with the low metal loading, could be the explanation of why no metallic Pt is observed.

In summarizing, the CO chemisorption and the XRD results could indicate the presence of both small of large particle, explained by the observed Pt peaks in XRD for alumina based catalyst. In addition, the absence of Pt for zirconia based catalyst, could be due to finely dispersed Pt, which could be explained by the high dispersion measured by CO chemisorption compared to alumina based catalyst. Furthermore, two reductions peaks, attributed to PtOx species together with the low H_2 loading and % reduction, could indicate that Pt is not fully reduced and that the catalyst contains of small loading of Pt and PtOx species. The absence of metallic platinum in the zirconia based catalyst could hence be explained by the low metal loading.

4.2 Raman Spectroscopy

Ex situ Raman measurements were carried out on the selected catalyst mentioned above and their respective carriers, using as a reference. A spectrum of α-PtO2 is shown for comparison. *In situ* Raman measurements were further carried out for 5wt.% Pt/ZrO_2 and 5wt.% Pt/Al_2O_3. Due to some complications with *in situ* window cell, the *in situ* results of 5wt.% Pt/Al_2O_3 shall not be included in the main report. However, the results have been attached to Appendix H. All the Raman spectra presented in the following sections are scaled all the same, but the baseline has been shifted up for clarity.

4.2.1 *Ex situ Raman*

Ex situ Raman was conducted to get an overview of the identified Raman bands and to probe the state of the supported noble Pt metal. Moreover, optimization of the Raman parameters prior to further *in situ* investigation was executed.

In order to determine the optimal experimental Raman parameters to use for this Raman study, *ex situ* measurements are necessary before any *in situ* measurements. These measurements were conducted to establish and gain an understanding of the principle and the Raman parameters. The Raman parameters used in this study are based on the specific catalyst and instrument used and it must be taken into account that the selected Raman parameters will vary for different experiments. The Raman parameters consist of, laser power, acquisition time, the number of accumulation and the objective.

The laser power, acquisition, and the number of accumulations all have similar effects. Increasing the laser power will increase the signal to noise ratio, however, if much laser power is used, it could be destructive, i.e. it can burn you sample and prevent analysis. Such damage can be seen as a degradation or deformation of the sample, where degradation is caused by discoloration of the sample. Increasing the number of accumulation can also be advantageous to obtain a better signal to noise ratio. In principle, the software simply sums the spectra recorded from each accumulation to obtain the overall spectra. An example done in the specialization project prior to this thesis shows how the desired Raman spectrum is optimized by adjusting the different Raman parameters are shown in Appendix G. On the other hand, increasing the number of accumulation will in principle just take more Raman measurements, which requires more time and increases the total exposure time.

There are several considerations to take into account when selecting the optimum acquisition time. As stated in section 2.7.3 the CCD detectors are sensitive to other forms of radiation, such as cosmic rays, which is detected as random spikes in the Raman spectrum. One way to eliminate the cosmic rays reaching to the detector is to use more than one scan to collect the data. For a sample that shows a high degree of fluorescence or a strong Raman scattering, there is a chance that the CCD detector becomes saturated due to the long exposure time, which is undesired.

The choice of the objective depends on the type of sample to be examined. In this study, both 15xNUV and 40xNUV were tested to see which objective gave the best Raman spectra. In principle, using 40xNUV should give a better spectral resolution than using 15xNUV. The 40xNUV with higher magnification and higher numerical aperture number (NA) should hence record a better spectrum. This is not the case for this study.

It is observed that using 15xNUV on the zirconia based catalyst, a better spectral resolution is recorded, and was therefore selected for this study. The deviation could be due to the lifetime of the objective. The 40xNUV is much older than the 15xNUV, and may, therefore, be the reason why the spectral resolution is not optimal.

Raman Spectra under Ambient Conditions

Figure 4.5 shows Raman spectra of the Pt/ZrO_2 catalyst with two different loading and the corresponding support for comparison. A spectrum of α-PtO_2 is shown as a reference. The series of spectra were measured under ambient conditions using excitation radiation at 633nm.

Under ambient conditions, a series of major Raman bands are observed at ~173, 329, 468 and 630 cm^{-1} for both Pt/ZrO_2 catalyst, marked with red in Figure 4.5, which are characteristic bands of monoclinic zirconia. This can be explained by the intensity of the two different peaks. For monoclinic phase, the intensity of the band at 468 cm^{-1} is much stronger than that of the band at 630 cm^{-1} [34], [44]. The support was measured for comparative reasons, and to identify other peaks that do not belong to ZrO_2. However, the peaks for both the catalyst and the support are almost identical, except for the doublet at ~330 cm^{-1}, which is not visible for 1wt.% Pt/ZrO_2. In addition to the support, a spectrum of PtO_2 sample was recorded under the same conditions. The crystalline reference Raman spectrum exhibit two sharp bands at 505 and 547 cm^{-1}, which have been assigned to A_{1g} + E_g vibrational modes [45], [46].
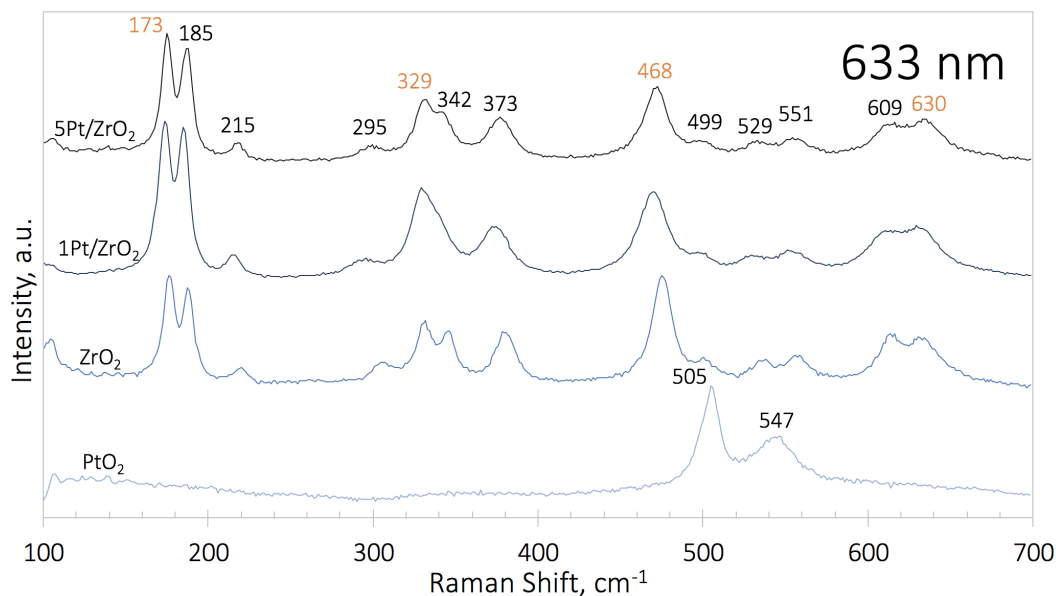
Figure 4.5: *Ex situ* Raman measurements of PtO_2, ZrO_2-support, 1wt.% and 5wt.% Pt/ZrO_2 at ambient conditions using visible laser. The major bands for ZrO_2 are marked with red. No visible peaks of PtO_2 are present in the two zirconia supported catalysts.

The Raman spectra of the Pt/ZrO_2 catalyst with two different loading and the crystalline PtO_2 reference under ambient conditions are presented in Figure 4.6. The corresponding support was not measured due to the downtime of the Raman instrument. Compared to the spectra measured with visible laser, the spectra recorded with near UV laser weakens with increasing metal loading. Moreover, the major peaks below $\sim 200 cm^{-1}$ are no longer visible in this excitation range. UV Raman spectroscopy is known for its sensitivity compared to visible Raman, particularly the surface region. According to Li et al. [44] it is found that UV Raman spectroscopy is a surface-sensitive technique for ZrO_2 because ZrO_2 has UV absorption. In general, most of the transition metal oxides strongly absorb UV laser light, making UV Raman spectroscopy more sensitive to the surface region than to the bulk for zirconia. Visible Raman spectroscopy gives, however, more information from both the bulk and the surface of zirconia due to no electronic absorption in the visible region [44], [47].

The crystalline PtO_2 reference Raman spectrum exhibits two sharp bands at ~ 516 and $558 cm^{-1}$ along with two less sharp bands located at ~ 325 and $878 cm^{-1}$. Further, these weak bands are also present in the 5wt.% Pt/ZrO_2 catalyst located at almost the same Raman shift. According to Deswardani et al. [48] the metal oxide, M-O, stretch should be expected in the vibrational region from 300-600 cm^{-1}, which could indicate

that the peak located at 878 cm^{-1} could be due to impurities as discussed in section 4.3 below. Whereas the peak located 325 cm^{-1} is not identified in the Raman spectra measured with a laser excitation at 325nm.
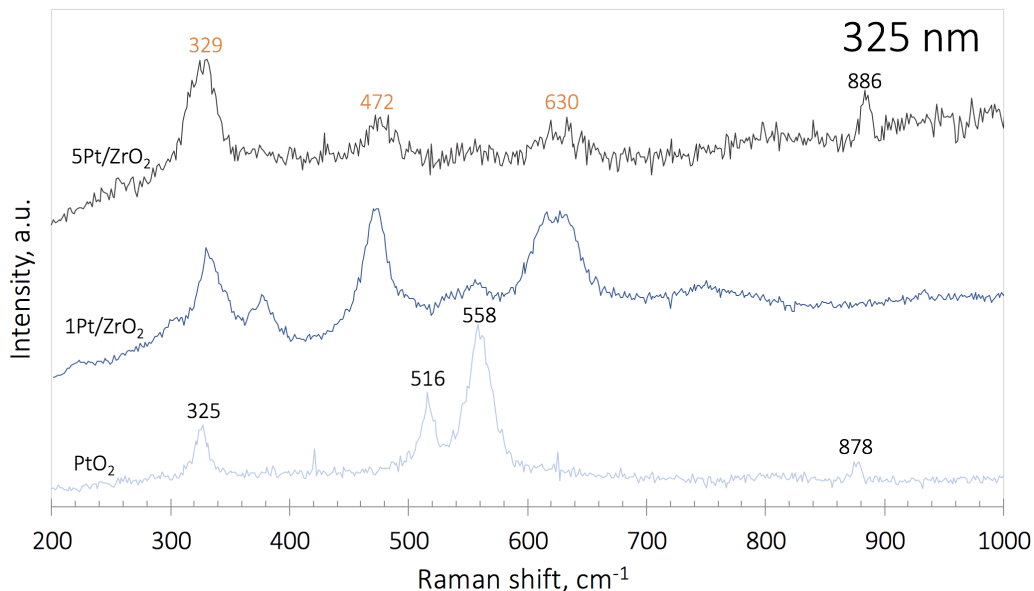
Figure 4.6: *Ex situ* Raman measurements of PtO$_2$, ZrO$_2$-support, 1wt.% and 5wt.% Pt/ZrO$_2$ at ambient conditions using near UV laser. The ZrO$_2$ peaks are less pronounce compared with visible laser due to the UV absorption. Higher loading of platinum reduces the ZrO$_2$ peak. An additional peak at ~ 880 cm$^-$1 is observed on 5wt.% Pt/ZrO$_2$ and PtO$_2$.

The Raman spectra of the Pt/Al$_2$O$_3$ catalyst with two different loading, the corresponding support and the crystalline PtO$_2$ reference under ambient conditions are presented in Figure 4.7. It can be seen from the figure that, apart from the spectrum of PtO$_2$, all spectra show a typical fluorescence background recorded with 633nm excitation. It is well known that spectra of alumina are quite fluorescent, and therefore expected to see these results. This has been a subject the past decades, and it has been believed that the fluorescence is due to either hydrocarbons, iron ion impurities, hydroxy groups or a combination of these. [49]. Using near UV excitation can, therefore, be an advantage for Raman studies of γ-alumina.

Figure 4.7: *Ex situ* Raman measurements of PtO_2, γ-alumina-support, 1wt.% and 5wt.% Pt/Al_2O_3 at ambient conditions using visible laser, showing a typical fluorescence background. No visible peaks assigned to PtO_2 are observed for the two Pt/Al_2O_3 catalysts.

The overall Raman spectra of alumina based catalyst with the corresponding support and the crystalline PtO_2 are presented in Figure 4.8(a) recorded with near UV laser at a wavelength of 325 nm. As the fluorescence is produced mainly from the transition from the ground state to the high vibrational state, fluorescence band primarily appears in the range from 300 to 700 nm or at the longer wavelength region as explained in section 2.5. Choosing a laser with a lower wavelength, such as UV-light can be used to avoid fluorescence. While the spectra excited at 633 nm are dominated by fluorescence, switching to excitation of 325 nm, the Raman signal with weaker fluorescence background can be collected. Near UV-light in the region of 325 nm is still in the range of fluorescence, and may, therefore, have a weak fluorescence background. Furthermore, to avoid the fluorescence background, an excitation with 244 nm is usually used. Another attempt to try to avoid or reduce the fluorescence background is to burn out the fluorescence. Fluorescence arising from an impurity, may in some cases be attempted to be burnt out by leaving the sample under the laser beam for some time. However, it is not guaranteed that it would work, it may occur after a few minutes, or even overnight. The reason for why this may work is because there is a specific absorption of the light into the fluorophore, that is preferentially degraded. Moreover, in some cases, especially for colored samples, absorption by the sample may cause a degradation [50]. However, this could potentially be reduced by rotating the sample, although this would require a proper instrument that can perform
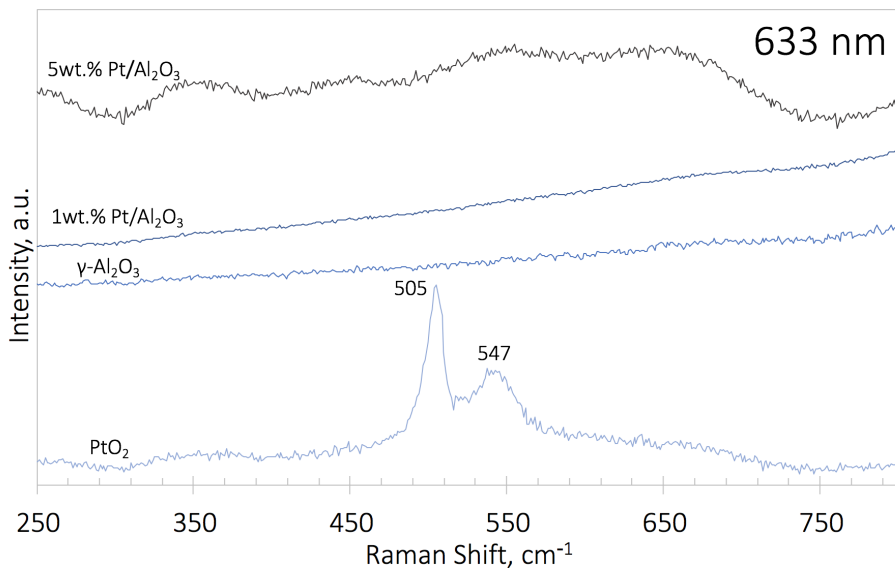
this.
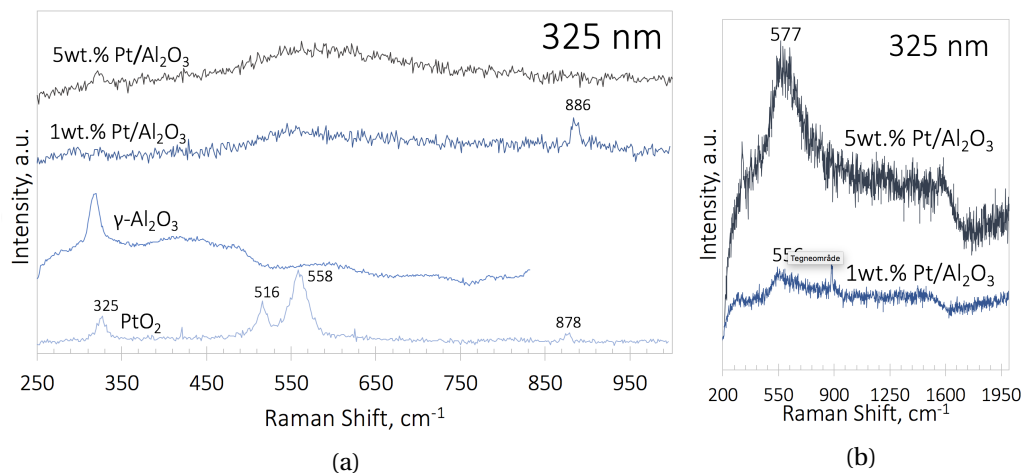
Figure 4.8: *Ex situ* Raman measurements of PtO$_2$, γ-alumina-support, 1wt.% and 5wt.% Pt/Al$_2$O$_3$ at ambient conditions using near UV laser. Overall Raman spectra (a) and zoom of 5wt.% and 1wt.% Pt/Al$_2$O$_3$ (b), showing peaks at 577cm^{-1} and 556cm^{-1}, respectively.

Due to the scaling, the two peaks observed for both of the alumina supported catalysts are no longer visible. It is, therefore, for the sake of clarity presented a zoom of 5wt.% and 1wt.% Pt/Al$_2$O$_3$ in Figure 4.8(b). Under ambient conditions only a broad peak located at 577 cm^{-1} for 5wt.% Pt/Al$_2$O$_3$ and 556 cm^{-1} for 1wt.% Pt/Al$_2$O$_3$ are present, which can be attributed to PtOx species. According to Uy et al. they reported a broad at 571 $\pm$4, which is assigned to the vibrational mode of atomic O on Pt [8]. This observation could pave the way for *in situ* Raman measurements to study the reversibility of the Pt-O mode, by doing oxidation-reduction treatment. Due to some complications with the in situ cell window, which will be further discussed in section 4.3, the *in situ* results recorded for 5wt.% Pt/Al$_2$O$_3$ are not shown or discussed in this chapter, however the results have been attached to Appendix H. The broad Raman band could also suggest presence of smaller particles.

As the metallic Pt is more active than PtOx species in NO oxidation, it is desired to be able to identify the noble metal [51]. However, pure metals as platinum do not exhibit Raman scattering, i.e. pure metals are not Raman active. In order to observe Raman scattering a change in the polarizability of a molecule must occur and thus the vibration is Raman active [11]. In a single crystal, the Raman mode is inactive due to the changes in polarizability which cancel over the crystal. However, for small crystallites, the mode could be activated by disorder [10]. As discussed in the other characterization methods, it is believed that the alumina based catalyst contains of small amount

of both Pt and PtOx, whereas Pt was identified in the XRD results, meaning that there are traces of Pt in the catalyst, but can not be detected by Raman spectroscopy due to no change in polarizability.

According to Lin et al. [46] they reported the vibration of amorphous PtO_2 nanoparticle in the Raman shift region of 610 cm^{-1} with an estimated particle size of ~1.5nm on Pt/Al_2O_3. This peak could resemble the peak observed in this study for alumina based catalyst, and the detected small nanoparticles could hence explain the broad Raman band. The smaller particles, the broader the Raman bands, and since it is detected even smaller particles for zircona based catalyst, which could explain why no peaks of PtO_2 are observed in Raman spectroscopy.

4.2.2 *In situ* Raman

In situ Raman measurements have been employed to investigate the metal support interaction in the supported noble Pt metal catalyst and to examine the simultaneous oxidation-reduction behavior of the metal and the oxide support. Prior to exposure to the reducing H_2/Ar environment, the samples were initially calcined in flowing O_2/Ar at 500 °, and further reoxidized.

Raman Spectra under Oxidation

A peak shift due to laser heating was not observed, but according to the temperature calibration, which was verified in the specialization project done prior to this thesis. The calcination of the sample, should according to the temperature calibration be accurate. The Raman spectra of 5wt.% Pt/ZrO_2 catalyst at elevated temperatures under oxidizing conditions recorded with 633nm and 325nm excitation are presented in Figure 4.9 and Figure 4.10, respectively. For the sake of clarity a zoom of 5wt.% Pt/ZrO_2 catalyst in the region 400-600 cm^{-1} are presented in Figure 4.9b. As seen in these figures no peaks attributed to Pt or PtO_2 are identified in the Raman spectra. In XRD, the X-ray penetrates through the whole sample and may give a more overall picture of the structure, and hence could be the reason why PtO_2 diffraction peaks are identified in the XRD pattern. While the Raman measurement technique is known to be limited to the surface of the sample, and may not be excepted to be able to detect PtO_2 in such low metal loading catalyst.
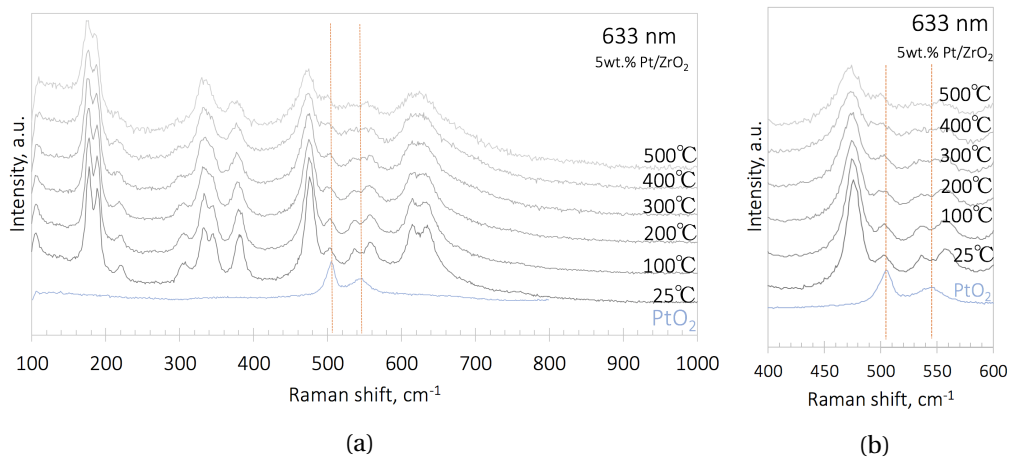
Figure 4.9: *In situ* Raman spectra of 5wt.% Pt/ZrO$_2$ measured at different temperatures, from ambient up to 500°C using visible laser, with a flow of 40ml/min 7% O$_2$/Ar. Increasing the temperature increases the noise level. No PtO$_2$ peaks are observed while increasing the temperature.

As stated above in the *ex situ* section, no metallic Pt nor PtOx species were present in the zirconia supported catalyst under ambient conditions. It is believed that the Raman signature does not seem to be able to distinguish between small and larger platinum particles with a size of <2nm and ~5nm, respectively. According to Uy et al. [8] the smaller particles may have been completely oxidized, i.e. leads to the loss of observable Pt-Pt bonds, and the larger particles may be more appropriately seen as bulk Pt covered with a chemisorbed layer of O, which could explain why only PtO$_2$ is detected for zirconia based catalyst in XRD. As shown in the chemisorption results the estimated particle size, were a size of <2nm, and most Pt atoms in the size range are most likely surface atoms and therefore hard to distinguish between a particle that is completely oxidized covered in atomic O. According to similar study reported by Baylet et al. [9] it can be expected that Raman spectroscopy should only give useful information on the smaller particles with a size of <4nm, while XRD measurements should be more sensitive to larger particles with a size of >4-5nm. The reason why no Pt or PtO$_2$ are not identified could be the fact that the Pt metal loading is not high enough, and hence no platinum species could be detected.
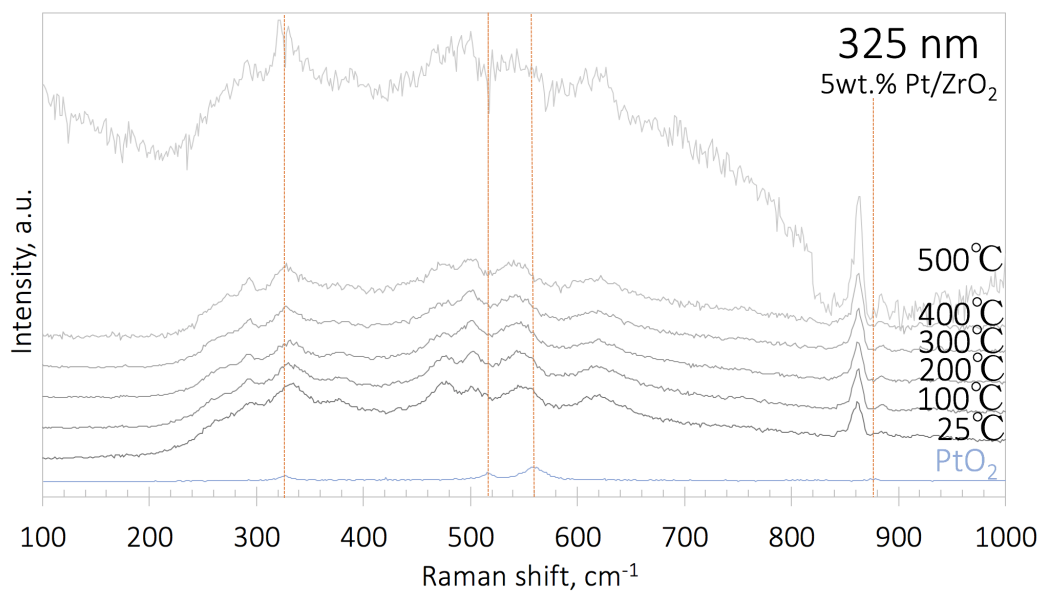
Figure 4.10: *In situ* Raman spectra of 5wt.% Pt/ZrO_2 measured at different temperatures using near UV-light. Increasing noise level is observed with increasing temperature. No PtO_2 peaks are observed while increasing the temperature.

As observed in both Figure 4.9 and Figure 4.10 the noise level increases with increasing temperature. It is especially noticeable for the Raman spectra acquired with the excitation radiation at 325nm. It is clear that at a temperature of 500°C, the Raman spectrum is quite noisy and has a fluorescence behavior and is thermally unstable. It is also observed that the zirconia peak detected with excitation radiation at 633nm decreases in intensity and broadens, which is better visualized under cooling after the reduction step, shown in Appendix H. This can be explained by that, for dispersed metal oxides, due to the influence of temperature, the intensity of the spectra becomes less severe as the volume fraction of oxides lowers. This effect could be attributable to thermal expansion and changes in occupants of the vibrational energy levels with increasing temperature reported by Xie et al. [52]. According to Chan et al. [53] they reported a thermal broadening at elevated temperatures, and further that the thermal treatment was reversible. This behavior is also observed in this study after the reduction step, under cooling of the sample, showing a very significant observation of this reversibility, shown in Appendix H. The Raman bands are reversed by cooling the sample to ambient temperatures. In addition, a quite intense Raman band is observed at ~860cm^{-1}, which is not expected since no bands above 700 cm^{-1} are identified when using the laser excitation at 633nm. Practically, the Raman shift should be the same for the different laser wavelengths, but could slightly deviate due to some

instrumentation reasons, which is discussed in the sections further below.

Raman Spectra under H$_2$ Reducing Conditions

The Raman spectra of 5wt.% Pt/ZrO$_2$ catalyst at 500°C held for two hours under H$_2$ reducing conditions recorded with 633nm and 325nm excitation are presented in Figure 4.11 and Figure 4.12, respectively. A spectrum of PtO$_2$ is shown for comparison.

In general, if there was observed any PtOx species in the Raman spectra the reduction of these particles into metallic Pt would be reduced already at 150 °C, according to the TPR results. In principle, at this temperature, the particle would be completely reduced i.e. the relative Raman signal being equal to 0, as discussed above, due to no change in polarizability. According to a similar study, they reported that the observed Pt-O mode could easily be removed with H$_2$ at room temperature [8]. This also applies to another study and reported that bulk PtO$_2$ was readily reduced to metallic Pt at 50°C by exposure to H$_2$ [9]. This could hence be in compliance with this study and as discussed above in section TPR, the low amount of H$_2$ consumption could indicate that Pt is not fully reduced, and that Pt is already in a reduced state at room temperature.
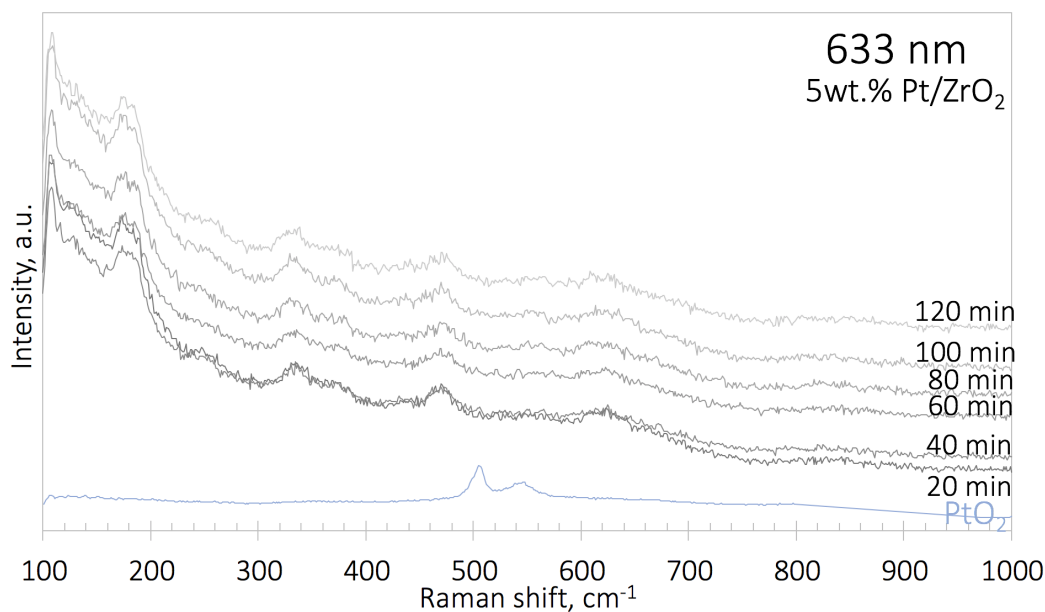
Figure 4.11: *In situ* Raman spectra of 5wt.% Pt/ZrO$_2$ measured at a temperature of 500°C for two hours under a reductive environment, using visible laser.

According to Su et al. that investigated the reduction of zirconia supported Pd. Where they observed that the features of the zirconia weaken upon reducing of the sample under H_2 flow [54]. This trend could also be seen in this study. Moreover, this observation is more noticeable for excitation radiation at 633nm, which can be seen in Figure 4.15a). The explanation for this could be due to the high temperature, or the reducing gas flow combined with the total contact time with the sample. Due to the scaling and the change in baseline in Figure 4.11 and Figure 4.12 it can look like the peaks associated with zirconia oxides are reduced, but for the sake of clarity an overall Raman spectra in Figure 4.13 with a better vision of the spectra are shown. It is expected that the zirconia peaks are not reduced at a temperature of 500 °C, the reported reduction temperature of ZrO_2 should start around 690°C [35].
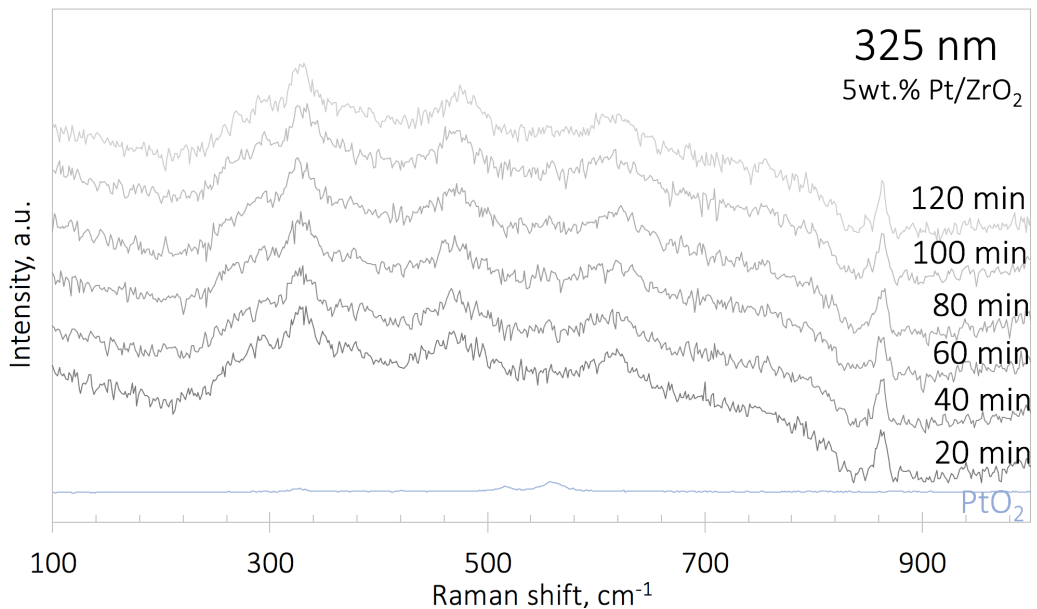
Figure 4.12: *In situ* Raman spectra of 5wt.% Pt/ZrO_2 measured at a temperature of 500°C for two hours under a reductive environment, using near UV-laser.

Raman Spectra under Reoxidation

In situ Raman under reoxidation was further conducted after the reduction step. No significant change was observed under this process, and therefore, not shown in this chapter. However, the results have been attached to Appendix H. As shown in Figure 4.13 a comparison of the oxidation-reduction process is shown for both excitation radiation at 633 and 325nm. From this summary it is quite noticeable that there is no significant change between the different conditions.

According to Uy et al. [8] it can be expected that the oxidation-reduction process could be completely reversible. It is reported that the reoxidation of platinum supported on alumina was completely reversible. The Pt-O peak could easily be removed by CO or H_2 and reoxidized at room temperature. A similar study on a different noble metal, palladium, did also report a completely reversible process for PdO under gas flows of O_2 and H_2. The reduction of the small PdO particles was reduced at room temperature, whereas the larger particles were reduced at 100°C, furthermore, the smaller particles were reoxidized at room temperature, while larger particles were oxidized at 300° [9]. According to these studies, it may seem that it is quite high probability that a reoxidation of this system may occur at low temperature or even at ambient temperature. However, as reported by Lin et al. [46] the reoxidation of the reduced Pt nanoparticle supported on alumina support could not be reversed, because the bulk PtO_2 phase was unstable at elevated temperatures. It may, therefore, not be said with certainty that reoxidation is entirely reversible, a further investigation of *in situ* Raman spectroscopy of PtO_2 is, therefore, necessary to study how the metal oxides behave under specific conditions.
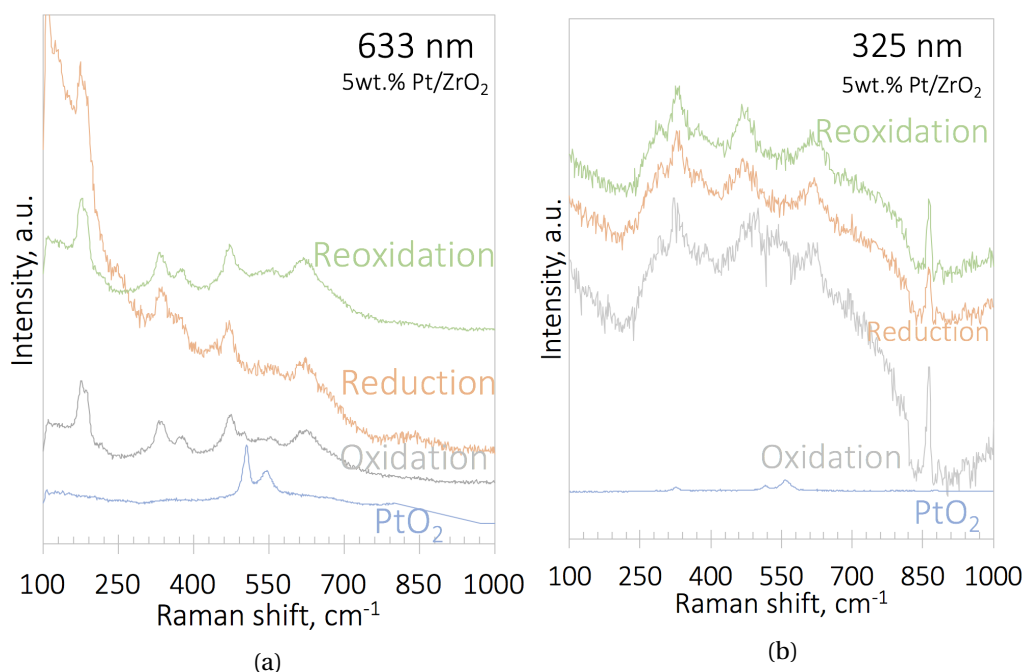
Figure 4.13: Summary of the *in situ* Raman measurements by doing a procedure of oxidation, reduction and further reoxidation using excitation radiation at 633nm and 325nm. All Raman spectra are recorded at 500 °C.

4.3 Complications with *in situ* cell window

The Raman spectra of 5wt.% Pt/Al$_2$O$_3$ and 5wt.% Pt/ZrO$_2$ with quartz, ZnSe and without *in situ* cell window with an excitation radiation at 325nm and 633nm are presented in Figure 4.14. Two window cell for the *in situ* set up is available for this study, ZnSe, and a quartz window. The choice of cell window type will depend upon the laser excitation wavelength employed. With a laser beam in the region near IR, ZnSe is usually selected because of its high transmission [55]. No visible complications with the window cell with the excitation radiation at 633nm were observed as seen in Figure 4.14b, besides only fluorescence was observed on the alumina based catalyst at the excitation radiation at 633nm, and is therefore chosen not show in this study.

According to Bourdon et al., a ZnSe window for a *in situ* measurement on Pd/Al$_2$O$_3$ was employed. However, no complications regarding the window cell were reported. They reported that ZnSe exhibit an intense Raman band at 252 cm^{-1}, and possible interference of these features could potentially of interest be avoided by using a confocal restriction. In principle, this would allow selecting a restricted collection volume by filtering out the signal coming from out-of-focus or adjacent region [55]. For this study, the confocal restriction was not the issue. As seen in Figure 4.14a an obvious trend is observed in every Raman spectra, which is the Raman band located around 860 cm^{-1}. Since this peak shows upon all the Raman spectra recorded with the excitation radiation at 325nm, it is then believed that this could indicate a disruption of the UV signal or other contamination of the Raman instrument. This trend is not visible for the Raman spectra using the excitation radiation at 633nm.
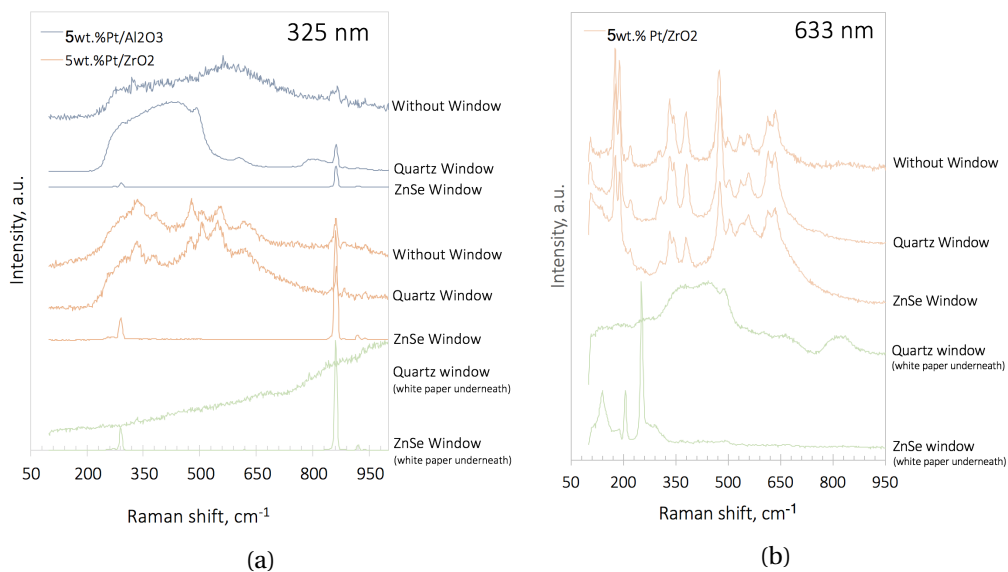
Figure 4.14: Raman spectra of 5wt.% Pt/Al_2O_3 and 5wt.% Pt/ZrO_2 with quartz, ZnSe and without *in situ* cell window. The blue, orange and the green Raman spectra illustrates the spectra of 5wt.% Pt/Al_2O_3, 5wt.% Pt/ZrO_2 and windows without sample underneath, respectively.

The fact that a Pt-O stretch is observed in the alumina supported Pt could pave the way for a *in situ* measurements, but due to the complication with the window cell used no measurements could be executed. It is observed that both the Raman spectra of ZnSe window with and without sample underneath shows the same spectra. The reason for this error could be due to the difficulty of the laser and camera focusing. With the ZnSe window, the camera could not detect any picture of the sample, and therefore, hard to know if it is focused on the window or the sample. Besides, as observed all the spectra recorded with the ZnSe all look alike, which indicates that the focus is primarily focused on the window and not the sample, and therefore weakens the signal of the alumina supported Pt. It is, therefore, recommended to try another *in situ* cell window, such as CaF_2 and BaF_2, which has high transmission in this region and hence could give a better signal. The quartz window on the other hand does not seem to provide the same problems, the spectrum at laser excitation at 325nm of alumina supported Pt appears to be due to a background of fluorescence.

Chapter 5

Conclusion

This research work focused on the advanced characterization method, *in situ* Raman spectroscopy on active platinum based catalysts for NO oxidation. The catalysts, alumina, and zirconia supported platinum catalyst, with metal loading of 5wt.%, have been synthesized by incipient wetness impregnation and characterized by nitrogen adsorption, CO chemisorption, XRD, and TPR.

The characterization techniques indicate that the catalysts contain both small and large particles detected by CO chemisorption and XRD, respectively. Both Pt and PtO_2 are identified, but due to the low metal loading, the associated Raman band could not be detected. However, a Raman band located at 577 cm^{-1} attributed to a Pt-O stretch, was identified in the Raman spectra of 5wt.% Pt/Al_2O_3, but due to the complications with the *in situ* cell window the experiment could not be further carried out. It is recommended to try more suitable *in situ* cell windows to optimize the Raman signal. Using more suitable diffraction gratings could also be a good idea, for instance, 1800 gr/mm for 633nm and 2400 gr/mm for 325nm.

In this project both *ex situ* and *in situ* Raman measurement were carried out. *Ex situ* Raman measurements were well established to gain an understanding of the principle of Raman spectroscopy and Raman parameters. A quite complex *In situ* Raman spectroscopic characterization procedure of 5wt.% Pt/ZrO_2 under certain reaction conditions have been successfully carried out using a quartz *in situ* cell window. However, this could be adapted to some other materials which can be more Raman active.

Chapter 6

Further Work

This work should carry on with the Pt system using NIR laser in the region 785nm, where fluorescence could be avoided. *In situ* Raman measurements on platinum oxides are encouraged to look into, to investigate how the metal oxides behave under specific conditions. A M-O stretch should be expected in the vibrational region from 300-600 cm^{-1}. Furthermore, it could be interesting to adapt this research to some other materials which may be more Raman active.

A NO adsorption experiment was planned for this study, but, unfortunately, due to a technical downtime right when this experiment was planned, further investigation was not possible, and therefore not executed. The evolution of the Raman spectra under NO gas flow could be further tested to study the ability of Pt to dissociate adsorbed NO molecules. A suggested procedure for this experiment can be seen in Appendix I.1. To avoid the complications with the *in situ* cell window, it is recommended to try other windows which may be more suitable, such as CaF_2 and BaF_2. It could also be a good idea to mix in a sample which is easily focused and detected by the Raman instrument, to enhance the focus of the sample itself.

If the above mentioned work is successfully run, it would be interesting to move forward to reactions, i.e., *operando* spectroscopy. Measurements of simultaneous catalytic activity and selectivity under reaction conditions could hence provide critical information and enables to study the structure-activity/selectivity relationship at the molecular level for supported metal oxides catalyst.

Bibliography

[1] I. E. Wachs, "In situ raman spectroscopy studies of catalysts," *Topics in Catalysis*, vol. 8, no. 1, pp. 57–63, 1999.

[2] G. S. Bumbrah and R. M. Sharma, "Raman spectroscopy–basic principle, instrumentation and selected applications for the characterization of drugs of abuse," *Egyptian Journal of Forensic Sciences*, vol. 6, no. 3, pp. 209–215, 2016.

[3] J. R. Ferraro, *Introductory raman spectroscopy*. Academic press, 2003.

[4] G. Mestl, "In situ raman spectroscopy—a valuable tool to understand operating catalysts," *Journal of Molecular Catalysis A: Chemical*, vol. 158, no. 1, pp. 45–65, 2000.

[5] K. Skalska, J. S. Miller, and S. Ledakowicz, "Trends in nox abatement: A review," *Science of the total environment*, vol. 408, no. 19, pp. 3976–3989, 2010.

[6] Z. P. Deng, J. Li, H. He, and L. D. Zhang, "The activities of no oxidation over the pt/γ-al$_2$o$_3$ catalyst," in *Applied Mechanics and Materials*, Trans Tech Publ, vol. 281, 2013, pp. 385–388.

[7] M. Banares and I. Wachs, "Molecular structures of supported metal oxide catalysts under different environments," *Journal of Raman Spectroscopy*, vol. 33, no. 5, pp. 359–380, 2002.

[8] D. Uy, A. E. O'Neill, and W. H. Weber, "Uv raman studies of adsorbed oxygen and nox species on pt/γ-alumina catalysts," *Applied Catalysis B: Environmental*, vol. 35, no. 3, pp. 219–225, 2002.

[9] A. Baylet, P. Marecot, D. Duprez, P. Castellazzi, G. Groppi, and P. Forzatti, "In situ raman and in situ xrd analysis of pdo reduction and pd° oxidation supported on γ-al$_2$o$_3$ catalyst under different atmospheres," *Physical Chemistry Chemical Physics*, vol. 13, no. 10, pp. 4607–4613, 2011.

[10] J. F. Haw, *In situ Spectroscopy in Heterogeneous Catalysis*. Wiley Online Library, 2002.

[11] P. Larkin, *Infrared and Raman spectroscopy: principles and spectral interpretation*. Elsevier, 2017.

[12] Nanophoton, "What is raman spectroscopy," (Accessed December 12, 2017). [Online]. Available: http://www.nanophoton.net/raman/raman-spectroscopy.html.

[13] H. H. Jaffe and A. L. Miller, "The fates of electronic excitation energy," *Journal of Chemical Education*, vol. 43, no. 9, p. 469, 1966.

[14] S. Jin, Z. Feng, F. Fan, and C. Li, "Uv raman spectroscopic characterization of catalysts and catalytic active sites," *Catalysis Letters*, vol. 145, no. 1, pp. 468–481, 2015.

[15] HORIBA, "What laser wavelengths are used for raman spectroscopy?," (Accessed December 11, 2017). [Online]. Available: http://www.horiba.com/scientific/.

[16] Semrock, "Filter types for raman spectroscopy applications," (Accessed December 12, 2017). [Online]. Available: https://www.semrock.com/filter-types-for-raman-spectroscopy-applications.aspx.

[17] D. Wieboldt, "Understanding raman spectrometer parameters," 2010 (Accessed December 17, 2017). [Online]. Available: http://www.spectroscopyonline.com/understanding-raman-spectrometer-parameters?id=&pageID=1&sk=&date=.

[18] P. Beato, E. Schachtl, K. Barbera, F. Bonino, and S. Bordiga, "Operando raman spectroscopy applying novel fluidized bed micro-reactor technology," *Catalysis today*, vol. 205, pp. 128–133, 2013.

[19] C. Palmer and E. G. Loewen, *Diffraction grating handbook*. Newport Corporation New York, 2005.

[20] U. B. Cappel, I. M. Bell, and L. K. Pickard, "Removing cosmic ray features from raman map data by a refined nearest neighbor comparison method as a precursor for chemometric analysis," *Applied spectroscopy*, vol. 64, no. 2, pp. 195–200, 2010.

[21] Linkam, *CCR1000 Catalyst Cell Reactor, USER GUIDE*. 2017.

[22] E. Marceau, X. Carrier, and M. Che, "Impregnation and drying," *Synthesis of Solid Catalysts*, pp. 59–82, 2009.

[23] C. R. Second, E. Edition, G. Ertl, H. Knözinger, F. Schüth, J. Weitkamp, and W.-V.V.G. C. KGaA, *Handbook of heterogeneous catalysis*, 2008.

[24] J. W. Niemantsverdriet, *Spectroscopy in catalysis: an introduction*. John Wiley & Sons, 2007.

[25] J. M. Thomas and W. J. Thomas, *Principles and practice of heterogeneous catalysis*. John Wiley & Sons, 2014.

[26] K. Sing, "The use of nitrogen adsorption for the characterisation of porous materials," *Colloids and Surfaces A: Physicochemical and Engineering Aspects*, vol. 187, pp. 3–9, 2001.

[27] I. Chorkendorff and J. W. Niemantsverdriet, *Concepts of modern catalysis and kinetics*. John Wiley & Sons, 2017.

[28] M. Che and J. C. Védrine, *Characterization of solid materials and heterogeneous catalysts: From structure to surface reactivity*. John Wiley & Sons, 2012.

[29] H. J. Yvon, *LabRAM User Guide. An Introduction to the Software and Hardware*. 2004.

[30] S. Gómez-Quero, T. Tsoufis, P. Rudolf, M. Makkee, F. Kapteijn, and G. Rothenberg, "Kinetics of propane dehydrogenation over pt-sn/al$_2$o$_3$," *Catalysis Science & Technology*, vol. 3, no. 4, pp. 962–971, 2013.

[31] K. Y. Koo, U. H. Jung, and W. L. Yoon, "A highly dispersed pt/γ-al$_2$o$_3$ catalyst prepared via deposition–precipitation method for preferential co oxidation," *international journal of hydrogen energy*, vol. 39, no. 11, pp. 5696–5703, 2014.

[32] M. Goula, N. Charisiou, K. Papageridis, A Delimitis, E Papista, E Pachatouridou, E. Iliopoulou, G Marnellos, M Konsolakis, and I. Yentekakis, "A comparative study of the h$_2$-assisted selective catalytic reduction of nitric oxide by propene over noble metal (pt, pd, ir)/γ-al$_2$o$_3$ catalysts," *Journal of Environmental Chemical Engineering*, vol. 4, no. 2, pp. 1629–1641, 2016.

[33] E. Pachatouridou, E. Papista, E. F. Iliopoulou, A. Delimitis, G. Goula, I. V. Yentekakis, G. E. Marnellos, and M. Konsolakis, "Nitrous oxide decomposition over al$_2$o$_3$ supported noble metals (pt, pd, ir): Effect of metal loading and feed composition," *Journal of Environmental Chemical Engineering*, vol. 3, no. 2, pp. 815–821, 2015.

[34] X. Yang, X. Yu, M. Lin, M. Ge, Y. Zhao, and F. Wang, "Interface effect of mixed phase pt/zro$_2$ catalysts for hcho oxidation at ambient temperature," *Journal of Materials Chemistry A*, vol. 5, no. 26, pp. 13 799–13 806, 2017.

[35] F. Pompeo, N. N. Nichio, M. M. Souza, D. V. Cesar, O. A. Ferretti, and M. Schmal, "Study of ni and pt catalysts supported on α-al$_2$o$_3$ and zro$_2$ applied in methane reforming with co$_2$," *Applied Catalysis A: General*, vol. 316, no. 2, pp. 175–183, 2007.

[36] E Xue, K. Seshan, and J. Ross, "Roles of supports, pt loading and pt dispersion in the oxidation of no to no$_2$ and of so$_2$ to so$_3$," *Applied Catalysis B: Environmental*, vol. 11, no. 1, pp. 65–79, 1996.

[37] C. H. Bartholomew and R. J. Farrauto, *Fundamentals of industrial catalytic processes*. Blackie Academic & Professional, 1997.

[38] K.-C. Chiang, K.-L. Chen, C.-Y. Chen, J.-J. Huang, Y.-H. Shen, M.-Y. Yeh, and F. F. Wong, "Recovery of spent alumina-supported platinum catalyst and reduction of platinum oxide via plasma sintering technique," *Journal of the Taiwan Institute of Chemical Engineers*, vol. 42, no. 1, pp. 158–165, 2011.

[39] S. S. Kim, S. H. Choi, S. M. Lee, and S. C. Hong, "Enhanced catalytic activity of pt/al_2o_3 on the ch_4 scr," *Journal of Industrial and Engineering Chemistry*, vol. 18, no. 1, pp. 272–276, 2012.

[40] J. Feng, M. Zhang, and Y. Yang, "Dehydrogenation of propane on pt or ptsn catalysts with al_2o_3 or sba-15 support," *Chinese Journal of Chemical Engineering*, vol. 22, no. 11-12, pp. 1232–1236, 2014.

[41] P. T. Do, M. Chiappero, L. L. Lobban, and D. E. Resasco, "Catalytic deoxygenation of methyl-octanoate and methyl-stearate on pt/al_2o_3," *Catalysis letters*, vol. 130, no. 1-2, pp. 9–18, 2009.

[42] H.-S. Roh, D.-W. Jeong, K.-S. Kim, I.-H. Eum, K. Y. Koo, and W. L. Yoon, "Single stage water–gas shift reaction over supported pt catalysts," *Catalysis letters*, vol. 141, no. 1, pp. 95–99, 2011.

[43] H. C. Lee, D. Lee, O. Y. Lim, S. Kim, Y. T. Kim, E.-Y. Ko, and E. D. Park, "Zro_2-supported pt catalysts for water gas shift reaction and their non-pyrophoric property," in *Studies in Surface Science and Catalysis*, vol. 167, Elsevier, 2007, pp. 201–206.

[44] C. Li and M. Li, "Uv raman spectroscopic study on the phase transformation of zro_2, y_2o_3–zro_2 and $so_4 2- /zro_2$," *Journal of Raman Spectroscopy*, vol. 33, no. 5, pp. 301–308, 2002.

[45] J. McBride, G. Graham, C. Peters, and W. Weber, "Growth and characterization of reactively sputtered thin-film platinum oxides," *Journal of applied physics*, vol. 69, no. 3, pp. 1596–1604, 1991.

[46] W. Lin, A. Herzing, C. Kiely, and I. Wachs, "Probing metal- support interactions under oxidizing and reducing conditions: In situ raman and infrared spectroscopic and scanning transmission electron microscopic- x-ray energy-dispersive spectroscopic investigation of supported platinum catalysts," *The Journal of Physical Chemistry C*, vol. 112, no. 15, pp. 5942–5951, 2008.

[47] M. Li, Z. Feng, G. Xiong, P. Ying, Q. Xin, and C. Li, "Phase transformation in the surface region of zirconia detected by uv raman spectroscopy," *The Journal of Physical Chemistry B*, vol. 105, no. 34, pp. 8107–8111, 2001.

[48] F Deswardani, R Maulia, and E Suharyadi, "Study of structural and magnetic properties of silica and polyethylene glycol (peg-4000)-encapsulated magnesium nickel ferrite (mg0. 5ni0. 5fe2o4) nanoparticles," in *IOP Conference Series: Materials Science and Engineering*, IOP Publishing, vol. 202, 2017, p. 012 047.

[49] A Aminzadeh, "Excitation frequency dependence and fluorescence in the raman spectra of al$_2$o$_3$," *Applied spectroscopy*, vol. 51, no. 6, pp. 817–819, 1997.

[50] E. Smith and G. Dent, *Modern Raman spectroscopy: a practical approach.* John Wiley & Sons, 2013.

[51] H.-F. Wang, Y.-L. Guo, G. Lu, and P Hu, "No oxidation on platinum group metals oxides: First principles calculations combined with microkinetic analysis," *The Journal of Physical Chemistry C*, vol. 113, no. 43, pp. 18 746–18 752, 2009.

[52] T.-c. Xiao, S.-f. Ji, H.-t. Wang, K. S. Coleman, and M. L. Green, "Methane combustion over supported cobalt catalysts," *Journal of Molecular Catalysis A: Chemical*, vol. 175, no. 1, pp. 111–123, 2001.

[53] S. S. Chan and I. E. Wachs, "In-situ laser raman spectroscopy of nickel oxide supported on. gamma.-al$_2$o$_3$," *J. Catal.;(United States)*, vol. 103, no. 1, 1987.

[54] S. C. Su, J. N. Carstens, and A. T. Bell, "A study of the dynamics of pd oxidation and pdo reduction by h$_2$and ch$_4$," *Journal of Catalysis*, vol. 176, no. 1, pp. 125–135, 1998.

[55] G Le Bourdon, F Adar, M Moreau, S Morel, J Reffner, A.-S. Mamede, C Dujardin, and E Payen, "In situ characterization by raman and ir vibrational spectroscopies on a single instrument: Deno x reaction over a pd/γ-al$_2$o$_3$ catalyst," *Physical Chemistry Chemical Physics*, vol. 5, no. 20, pp. 4441–4444, 2003.

[56] A. Alvarenga, M Grimsditch, and A Polian, "Raman scattering from cubic boron nitride up to 1600 k," *Journal of applied physics*, vol. 72, no. 5, pp. 1955–1956, 1992.

[57] H Herchen and M. Cappelli, "Temperature dependence of the cubic boron nitride raman lines," *Physical Review B*, vol. 47, no. 21, p. 14 193, 1993.

[58] T. Kawamoto, K. N. Matsukage, T. Nagai, K. Nishimura, T. Mataki, S. Ochiai, and T. Taniguchi, "Raman spectroscopy of cubic boron nitride under high temperature and pressure conditions: A new optical pressure marker," *Review of scientific instruments*, vol. 75, no. 7, pp. 2451–2454, 2004.

[59] F. Datchi and B. Canny, "Raman spectrum of cubic boron nitride at high pressure and temperature," *Physical Review B*, vol. 69, no. 14, p. 144 106, 2004.

Appendix A

Calculation for catalyst preparation

NO oxidation catalysts with 5 wt.% platinum on γ-alumina and zirconia were prepared by one step incipient wetness impregnation of γ-Al$_2$O$_3$ and ZrO$_2$ supports with an aqueous solution of platinum nitrate, Pt(NO$_3$)$_4$. Necessary properties of platinum precursor salt are summarized in table A.1.

Table A.1: Chemical properties of metal precursor required for preparing catalysts with 5 wt.%Pt.

Property	Platinum
Chemical formula	Pt(NO$_3$)$_4$
Physical state	Solution
Molecular weight	443.1036 g/mole
Percentage solution	15% w/w

A.1   Catalyst preparation

The calculations to determine the amount of deionized water and precursor salt needed for one step incipient impregnation of 5g γ-Al$_2$O$_3$ to get a metal loading of 5 wt.% platinum is shown below. Same procedure for 5 wt.% platinum on zirconia was used, with a pore volume of 0,7810 cm^3/g. A summary of measured components is shown in table A.2.

$$\text{Amount of catalyst}: m_{catalyst} = 5g$$

$$\text{Mass of platinum}: m_{Pt} = \frac{5}{100} \cdot m_{catalyst}$$

$$\text{Mass of platinum}: m_{Pt} = \frac{5}{100} \cdot m_{catalyst}$$

$$m_{Pt} = 0.25g$$

$$\text{Mass of alumina support}: m_{support} = m_{Pt} - m_{catalyst}$$

$$m_{support} = 4.75g$$

$$\text{Pore volume of alumina support} = 1.33 \frac{cm^3}{g_{support}}$$

$$\text{Incipient wetness point}: IWP = 6.3175 cm^3$$

$$\text{Mass required platinum precursor}: m_{Pt_{precursor}} = \frac{m_{Pt}}{0.15}$$

$$m_{Pt_{precursor}} = 1.67g$$

$$\text{Water in platinum precursor}: m_{Pt_{precursor_{liquid}}} = m_{Pt_{precursor}} \cdot (1 - 0.15)$$

$$m_{Pt_{precursor_{liquid}}} = 1,416g$$

$$\text{Amount of water needed} = IWP - m_{Pt_{precursor_{liquid}}}$$

$$= 4.901g$$

Table A.2: A summary of measured amounts of water and chemicals needed for preparing catalysts with 5 wt.%Pt.

Component	Amount [g]
γ-Al_2O_3	4.7513
ZrO_2	4.7524
Pt-precursor$_{Al_2O_3}$	1.6688
Pt-precursor$_{ZrO_2}$	1.6745
Water$_{Al_2O_3}$	4.9052
Water$_{ZrO_2}$	2.2984

Appendix B

BET surface area calculations and N_2 adsorption summary reports

Summary reports were obtained using the BET instrument, Micromeritics. The BET surface area for 5wt.% Pt/Al_2O_3 was reported to be 63 m^2, which seemed to be wrong. The surface area was therefore calculated manually using selected points from the BET surface area plot. The calculations were not necessary for 5wt.% Pt/ZrO_2 because the isotherm plot was already linear. The calculations using Eq. 2.8 and Eq. 2.9 are shown below together with the summary reports.
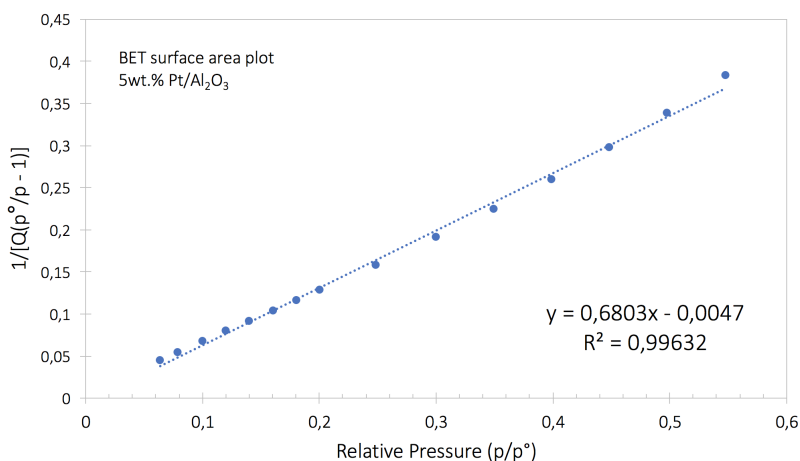
Figure B.1: Selected points from BET surface area plot of 5wt.% Pt/Al_2O_3 used to calculate the BET surface area. A slope of 0.6802 and an intercept of -0.0047 are obtained from the plot.

- Calculation of BET constant C:

$$\frac{C-1}{V_m C} = 0.6803$$

$$(C-1) \cdot \frac{1}{V_m C} = 0.6803$$

$$C = \frac{0.6803}{-0.0047} + 1$$

$$C = -143.74$$

- Calculation of the volume of the adsorbed monolayer, V_m:

$$\frac{1}{V_m C} = -0.0047 \tag{B.1}$$

$$V_m = \frac{\frac{1}{C}}{-0.0047} \tag{B.2}$$

$$V_m = \frac{\frac{1}{-143.74}}{-0.0047} \tag{B.3}$$

$$V_m = 1.48 mmol/g \tag{B.4}$$

$$V_m = 0.00148 mol/g \tag{B.5}$$

- Calculation of S_{BET}:

Using L, Avogadro's number=$6.022 \cdot 10^{23}$ and $\sigma_{N_2} = 16.2 \cdot 10^{-20}$ m^2.

$$S_{BET} = V_m \cdot L \cdot \sigma_{N_2} \tag{B.6}$$

$$S_{BET} = 144,40 m^2/g \tag{B.7}$$

Sample: 5wtPt/Al2O3
Operator: My
Submitter:
File: C:\TriStar II 3020\data\My\000-218_2.SMP

Started: 01.05.2018 15:11:06
Completed: 01.05.2018 18:48:20
Report Time: 02.05.2018 09:52:35
Sample Mass: 0,0622 g
Cold Free Space: 35,0095 cm³
Low Pressure Dose: None
Automatic Degas: No

Analysis Adsorptive: N2
Analysis Bath Temp.: -195,800 °C
Thermal Correction: No
Warm Free Space: 11,7102 cm³ Measured
Equilibration Interval: 5 s
Sample Density: 1,000 g/cm³

Summary Report

Surface Area

Single point surface area at p/p° = 0,300156096: 153,1973 m²/g

BET Surface Area: 63,3629 m²/g

BJH Adsorption cumulative surface area of pores
between 17,000 Å and 3 000,000 Å width: 152.015 m²/g

BJH Desorption cumulative surface area of pores
between 17,000 Å and 3 000,000 Å width: 156,3032 m²/g

Pore Volume

BJH Adsorption cumulative volume of pores
between 17,000 Å and 3 000,000 Å width: 0,311690 cm³/g

BJH Desorption cumulative volume of pores
between 17,000 Å and 3 000,000 Å width: 0,359701 cm³/g

Pore Size

BJH Adsorption average pore width (4V/A): 82,016 Å

BJH Desorption average pore width (4V/A): 92,052 Å

D-H Adsorption average pore width (4V/A): 82,085 Å

D-H Desorption average pore width (4V/A): 92,485 Å

APPENDIX B. BET SURFACE AREA CALCULATIONS AND N$_2$ ADSORPTION SUMMARY REPORTS

Sample: 5Pt/ZrO2
Operator: MNT
Submitter:
File: C:\TriStar II 3020\data\My\000-122.SMP

Started: 06.04.2018 17:09:38
Completed: 06.04.2018 22:45:16
Report Time: 01.05.2018 14:51:20
Sample Mass: 0,0556 g
Cold Free Space: 32,4465 cm³
Low Pressure Dose: None
Automatic Degas: No

Analysis Adsorptive: N2
Analysis Bath Temp.: -195,850 °C
Thermal Correction: No
Warm Free Space: 11,0303 cm³ Measured
Equilibration Interval: 5 s
Sample Density: 1,000 g/cm³

Summary Report

Surface Area

Single point surface area at p/p° = 0,299189518: 75,7335 m²/g

BET Surface Area: 70,6056 m²/g

BJH Adsorption cumulative surface area of pores
between 17,000 Å and 3 000,000 Å width: 83.449 m²/g

BJH Desorption cumulative surface area of pores
between 17,000 Å and 3 000,000 Å width: 99,1238 m²/g

Pore Volume

Single point adsorption total pore volume of pores
less than 729,386 Å width at p/p° = 0,972326096: 0,231588 cm³/g

BJH Adsorption cumulative volume of pores
between 17,000 Å and 3 000,000 Å width: 0,263876 cm³/g

BJH Desorption cumulative volume of pores
between 17,000 Å and 3 000,000 Å width: 0,276716 cm³/g

Pore Size

Adsorption average pore diameter (4V/A by BET): 131,2006 Å

BJH Adsorption average pore width (4V/A): 126,485 Å

BJH Desorption average pore width (4V/A): 111,665 Å
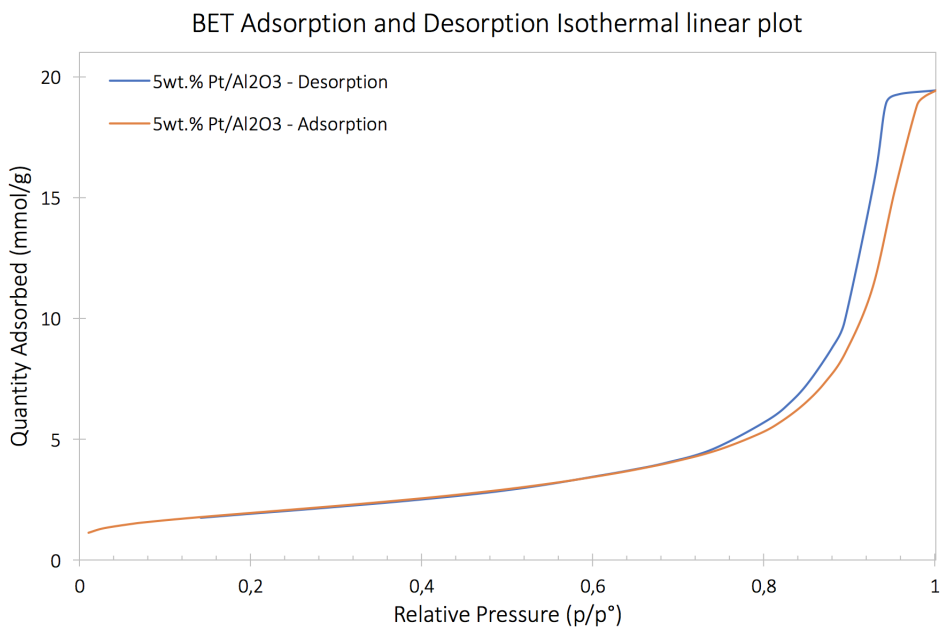
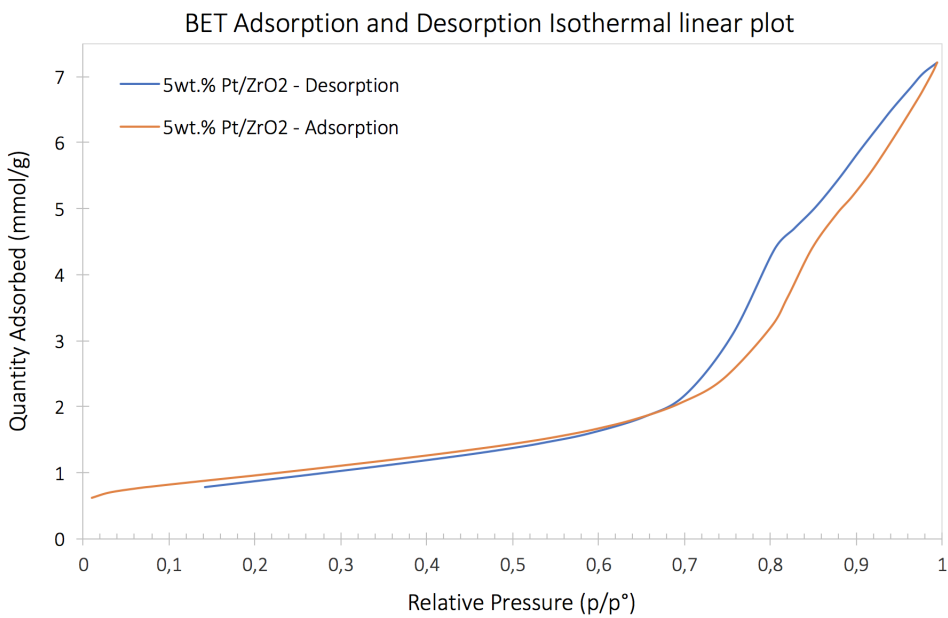Figure B.2: BET adsorption and desorption isotherms linear plot of 5wt.% Pt/Al$_2$O$_3$.

Figure B.3: BET adsorption and desorption isotherms linear plot of 5wt.% Pt/ZrO$_2$.

Appendix C

CO Chemisorption summary reports and isotherms

The reports below show the summary of the CO chemisorption results of 5wt.% Pt/Al_2O_3 and 5wt.% Pt/ZrO_2, respectively. The respective CO chemisorption isotherm line fit plot is shown as well.

Analysis Summary

Element	Percent of Sample Weight (%)	Atomic Weight	Stoichiometry Factor	Atomic Cross-Sectional Area (nm²)	Density (cm³/g)
platinum	5.000	195.090	1.000	0.0800	21.450

Analysis Results

Metal Dispersion: 34.6189 %
Metallic Surface Area: 4.2751 m²/g sample
Metallic Surface Area: 85.5030 m²/g metal
Crystallite Size (6.000 V / A): 3.27147 nm
Y-Intercept Quantity Adsorbed: 1.9887 ± 0.0084 cm³/g STP
Slope: 0.001266 ± 0.000044
Correlation Coefficient: 9.92197E-01

Difference Results

Metal Dispersion: 29.7530 %
Metallic Surface Area: 3.6742 m²/g sample
Metallic Surface Area: 73.4849 m²/g metal
Crystallite Size (6.000 V / A): 3.80650 nm
Y-Intercept Quantity Adsorbed: 1.7092 ± 0.0050 cm³/g STP
Slope: -0.000119 ± 0.000026
Correlation Coefficient: -7.80371E-01

Analysis Tabular Report

Pressure (mmHg)	Quantity Adsorbed (cm³/g STP)	Pressure (mmHg)	Quantity Adsorbed (cm³/g STP)	1st - Repeat (cm³/g STP)
0.9634	1.8272	1.1071	0.1821	1.6450
5.2213	1.9258	5.2923	0.2375	1.6883
10.5093	1.9640 *	10.4152	0.2669 *	1.6971 *
17.8623	1.9956 *	17.6372	0.2973 *	1.6983 *
21.5250	2.0017 *	21.1782	0.3004 *	1.7013 *
28.2087	2.0198 *	27.8461	0.3144 *	1.7054 *
31.9504	2.0241 *	34.2530	0.3248 *	1.6993 *
42.9705	2.0435 *	41.6271	0.3379 *	1.7055 *
52.5957	2.0587 *	53.3623	0.3572 *	1.7015 *
79.0046	2.1048 *	78.8841	0.3983 *	1.7065 *
106.1681	2.1484 *	106.0768	0.4457 *	1.7028 *
155.7283	2.2174 *	155.5831	0.5226 *	1.6948 *
205.4773	2.2821 *	205.5613	0.5697 *	1.7124 *
255.8273	2.3274 *	256.0953	0.6373 *	1.6901 *
306.1249	2.3761 *	305.1922	0.7130 *	1.6630 *
356.1313	2.4257 *	356.9843	0.7461 *	1.6796 *
405.8086	2.4696 *	406.5224	0.8372 *	1.6324 *

* Included in calculation of line fit and difference data.

Analysis Summary

Element	Percent of Sample Weight (%)	Atomic Weight	Stoichiometry Factor	Atomic Cross-Sectional Area (nm²)	Density (cm³/g)
platinum	5.000	195.090	1.000	0.0800	21.450

Analysis Results

Metal Dispersion: 41.7551 %
Metallic Surface Area: 5.1564 m²/g sample
Metallic Surface Area: 103.1283 m²/g metal
Crystallite Size (6.000 V / A): 2.71235 nm
Y-Intercept Quantity Adsorbed: 2.3986 ± 0.0710 cm³/g STP
Slope: 0.004912 ± 0.000374
Correlation Coefficient: 9.64311E-01

Difference Results

Metal Dispersion: 23.0835 %
Metallic Surface Area: 2.8506 m²/g sample
Metallic Surface Area: 57.0124 m²/g metal
Crystallite Size (6.000 V / A): 4.90630 nm
Y-Intercept Quantity Adsorbed: 1.3260 ± 0.0099 cm³/g STP
Slope: 0.000370 ± 0.000052
Correlation Coefficient: 8.92060E-01

Analysis Tabular Report

Pressure (mmHg)	Quantity Adsorbed (cm³/g STP)		Pressure (mmHg)	Quantity Adsorbed (cm³/g STP)	1st - Repeat (cm³/g STP)
1.0342	1.5102		1.0019	0.2816	1.2286
4.8151	1.8452		4.9075	0.5656	1.2796
15.3975	2.2231 *		15.2917	0.9046 *	1.3185 *
15.3975	2.2231 *		15.2917	0.9046 *	1.3185 *
20.8494	2.3491 *		21.7886	1.0348 *	1.3143 *
24.6236	2.4233 *		28.2878	1.1302 *	1.2931 *
30.3612	2.5104 *		31.4839	1.1689 *	1.3416 *
40.0411	2.6371 *		42.5796	1.2918 *	1.3453 *
50.3312	2.7466 *		55.9614	1.4198 *	1.3268 *
78.9993	2.9899 *		79.0028	1.6017 *	1.3882 *
104.8428	3.1614 *		106.2639	1.7652 *	1.3963 *
156.2453	3.4161 *		156.3600	1.9973 *	1.4188 *
205.6211	3.6054 *		205.2375	2.1772 *	1.4282 *
256.6954	3.7727 *		255.7415	2.3306 *	1.4422 *
305.2006	3.9054 *		305.7047	2.4605 *	1.4449 *
355.9028	4.0221 *		355.7004	2.5825 *	1.4396 *
405.7717	4.1430 *		407.0090	2.7038 *	1.4392 *

* Included in calculation of line fit and difference data.

Figure C.1: CO chemisorption line fit plot isotherms of 5wt.% Pt/Al_2O_3. The red curve shows the first analysis data, while the green line shows the repeated analysis. The blue line represents strongly adsorbed CO.
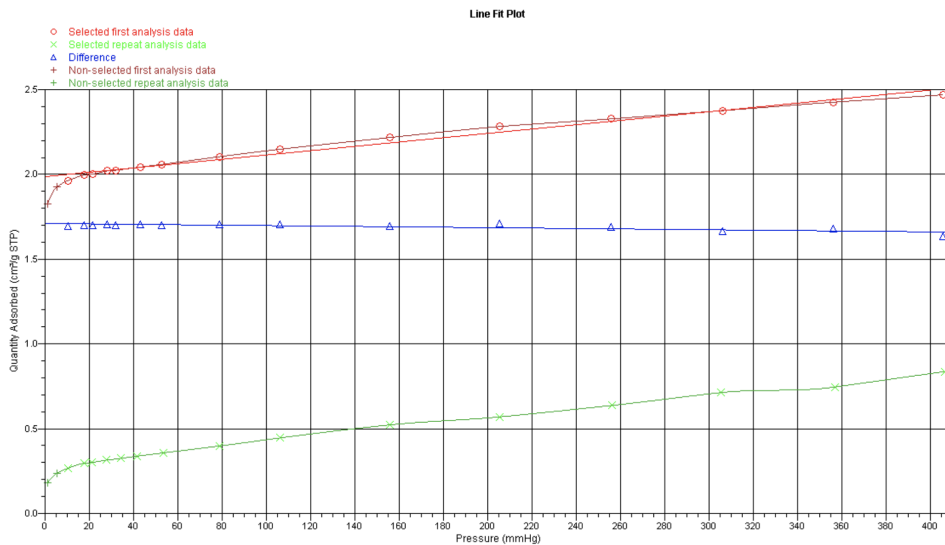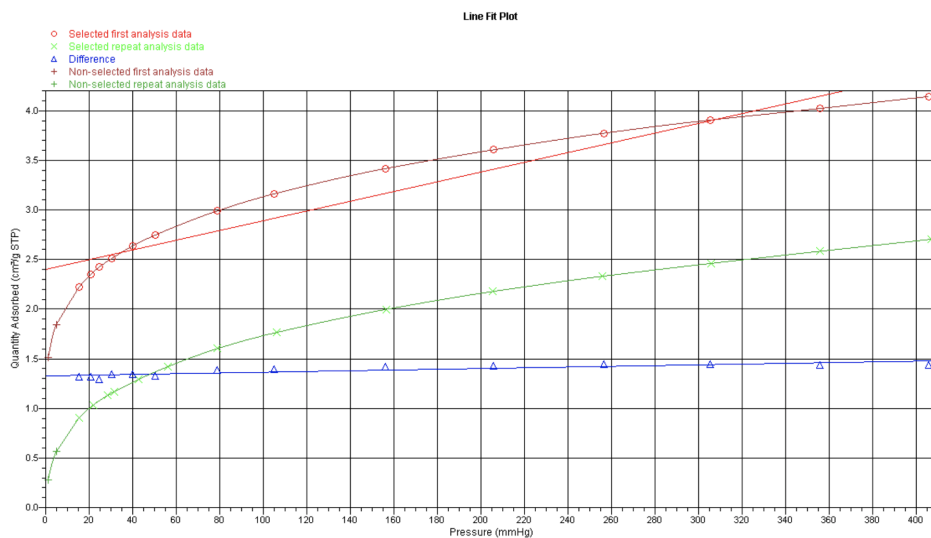

Figure C.2: CO chemisorption line fit plot isotherm of 5wt.% Pt/ZrO_2. The red curve shows the first analysis data, while the green line shows the repeated analysis. The blue line represents strongly adsorbed CO.

Appendix D

TPR H$_2$-consumption Altamira summary report

Summary reports were obtained using the instrument Altamira TPR. The hydrogen consumption was calculated by integrating the area under the curve using pulse calibration as a reference. The reports below shows a summary of 5wt.% Pt/Al$_2$O$_3$ (100mg), 5wt.% Pt/Al$_2$O$_3$ (250mg) and 5wt.% Pt/ZrO$_2$ (100mg), respectively.
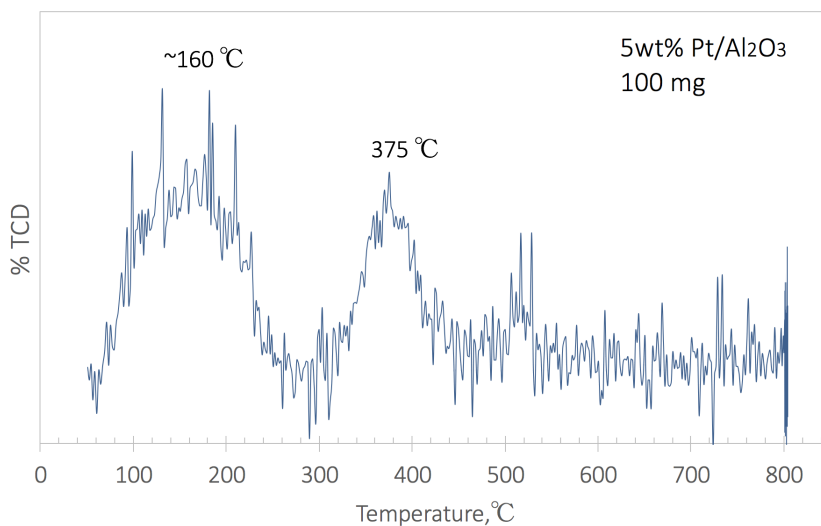
Figure D.1: TPR profile of 5wt.% Pt/Al$_2$O$_3$ with a loading of 100mg catalyst. TPR profiles measured from ambient temperature to 800 °C, showing two reduction peaks at ~150 °C and 375 °C.

```
****************************************************************
DFN Name :                @5Pt_Al2O3.dfn
Comments :                5Pt_Al2O3
Sample Weight :           0.1160 (g)
Active Component :        Pt @ 5.0 % Loading
Calibration Loop Volume : 530.0 (uL)
Loop Temperature :        25.0 (Deg C)
Loop Pressure :           1.0 (atm)
Analytical Gas :          H2 @ 7.0 %


****************************************************************
Uptake :                  65.429 (umol/g)

****************************************************************
% Dispersion :            25.528

Hemi-spherical diameter : 4.663E+1 (Angstroms)
Cubic side length :       3.886E+1 (Angstroms)

****************************************************************
% Reduction :             25.528

****************************************************************
Consumption :             25.528
```

Figure D.2: TPR summary report of 5wt.% Pt/ZrO$_2$ with sample loading of 100mg.

```
************************************************************
DFN Name :              @5Pt_Al2O3_250mg.dfn
Comments :              5PtAl2O3_250mg
Sample Weight :         0.2524 (g)
Active Component :      Pt @ 5.0 % Loading
Calibration Loop Volume :   530.0 (uL)
Loop Temperature :      25.0 (Deg C)
Loop Pressure :         1.0 (atm)
Analytical Gas :        H2 @ 7.0 %


************************************************************
Uptake :                71.764 (umol/g)

************************************************************
% Dispersion :          27.999

Hemi-spherical diameter :   4.251E+1 (Angstroms)
Cubic side length :     3.543E+1 (Angstroms)

************************************************************
% Reduction :           27.999

************************************************************
Consumption :           27.999
```

Figure D.3: TPR summary report of 5wt.% Pt/ZrO$_2$ with sample loading of 250mg.

```
*************************************************************
DFN Name :              @5Pt_ZrO2.dfn
Comments :              5Pt_ZrO2
Sample Weight :         0.1140 (g)
Active Component :      Pt @ 5.0 % Loading
Calibration Loop Volume :   530.0 (uL)
Loop Temperature :      25.0 (Deg C)
Loop Pressure :         1.0 (atm)
Analytical Gas :        H2 @ 7.0 %


*************************************************************
Uptake :                138.948 (umol/g)

*************************************************************
% Dispersion :          54.212

Hemi-spherical diameter :   2.196E+1 (Angstroms)
Cubic side length :     1.830E+1 (Angstroms)

*************************************************************
% Reduction :           54.212

*************************************************************
Consumption :           54.212
```

Figure D.4: TPR summary report of 5wt.% Pt/ZrO$_2$ with sample loading of 100mg.

Appendix E

X-Ray Diffraction (XRD)

The Figure E.1 and E.2, shows the XRD profiles of the crystalline phases of the samples, matched to the suggested reference patterns of spinel reflections, using DIFFRAC. EVA V4.1. The presented figures below show a clear peak of platinum observed on 5wt.%Pt/Al_2O_3 at 82°, and observed platinum oxide on 5wt.% Pt/ZrO_2 at 83.5°.
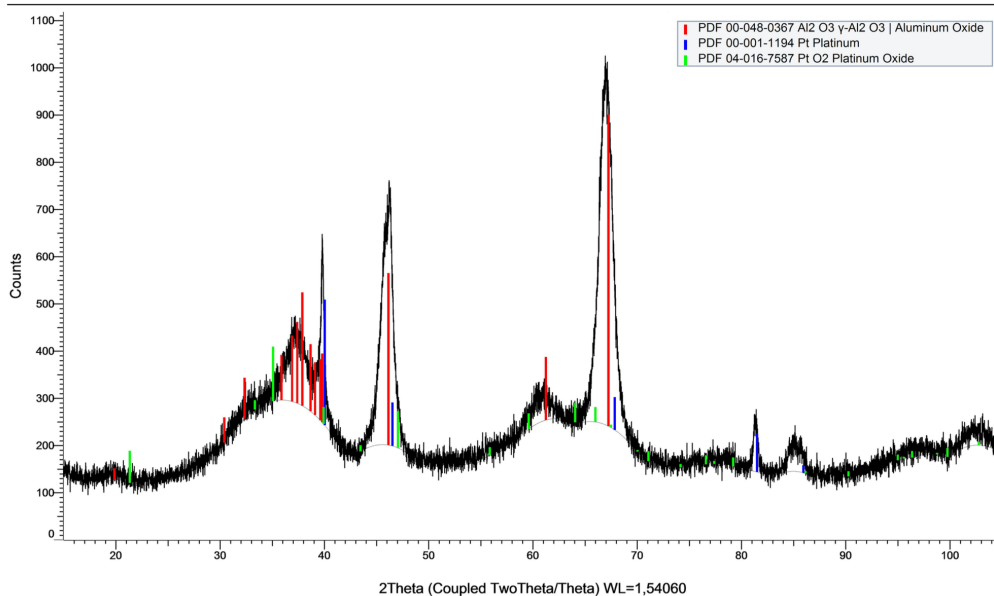
(Coupled TwoTheta/Theta)

Figure E.1: XRD profile of suggested reference patterns spinel reflections of 5wt.% Pt/Al_2O_3.

(Coupled TwoTheta/Theta)

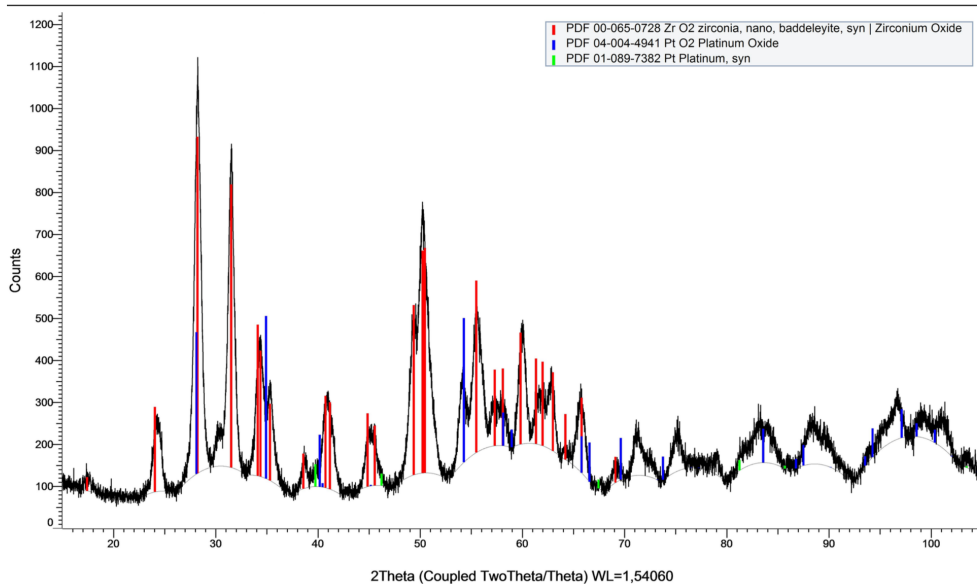Figure E.2: XRD profile of suggested reference patterns spinel reflections of 5wt.% Pt/Al_2O_3.

Appendix F

Raman spectroscopy

Temperature Calibration

A temperature calibration was executed in the specialization project prior to this thesis. The temperature dependency of the Raman shift was investigated using cubic boron nitride (c-BN) as the calibrant. At atmospheric pressure, the temperature dependency for the TO mode was observed around 1054 cm^{-1}. The Raman spectrum is given in Figure F.1 showing the TO mode under elevated temperatures.
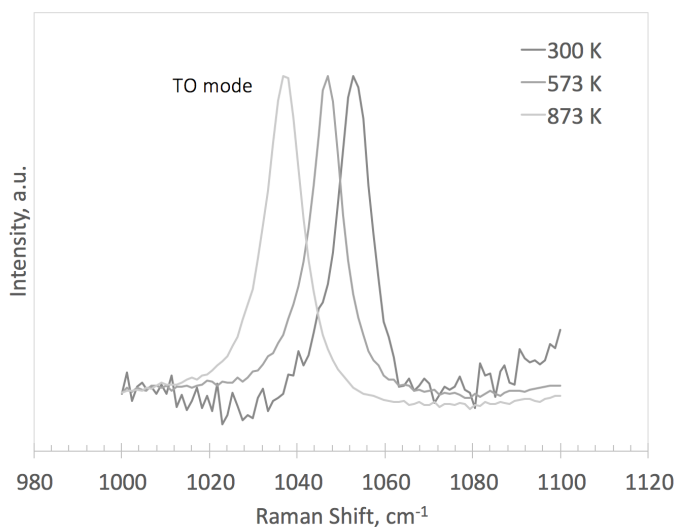

Figure F.1: Observed Raman spectra of the TO mode of cubic boron nitride, c-BN at temperatures of 300 K 573 K and 873 K. The peaks shifts to the left due to increased temperature.
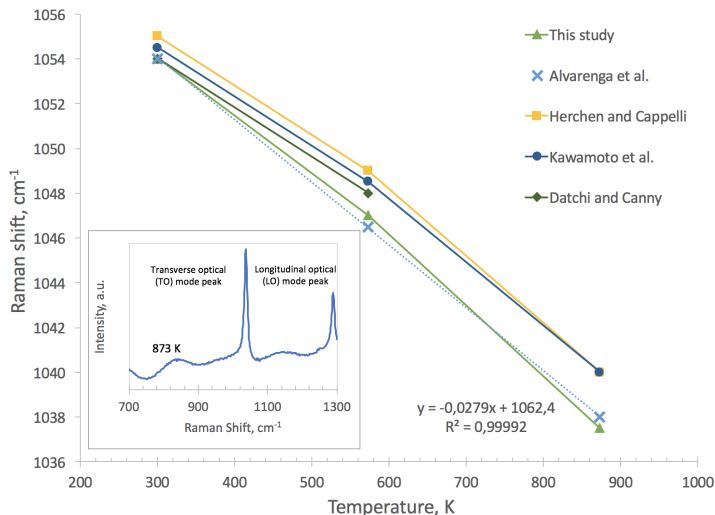
Figure F.2: Temperature dependence of the TO mode of cubic boron nitride, c-BN. The lines denote the Raman shift of the TO mode as a function of temperature. Triangles, crosses, squares, circles and diamonds represent data from this study, Alvarenga et al.[56], Herchen and Cappelli [57], Kawamoto et al. [58] and Datchi and Canny [59], respectively.
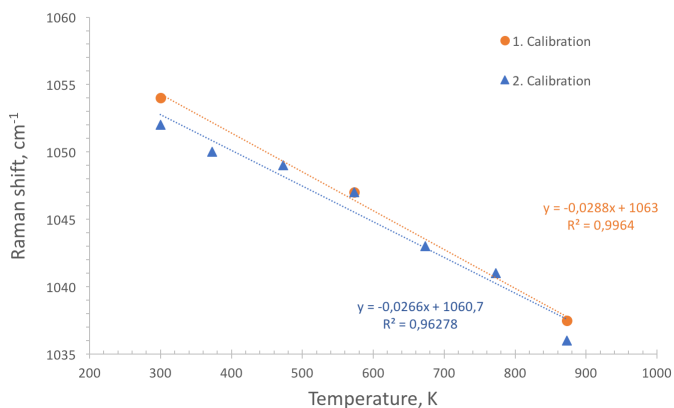

Figure F.3: Linear regression of the first and the second temperature calibration attempted. The circles and the triangles denote the measurements points for the first and the second calibration, respectively. The slope of the TO mode obtained are -0.0288±0.003 cm^{-1}/K and -0.0266±0.0067 cm^{-1}/K.

Appendix G

Ex situ Raman spectroscopy

Optimization of Raman parameters

These measurements were established to gain an understanding of the principle and the Raman parameters. The spectra presented below shows the process of how to obtain the desired spectrum by adjusting the different Raman parameters. *Ex situ* Raman measurements were performed on alumina supported cobalt catalysts obtained from the specialization project done prior to this thesis.
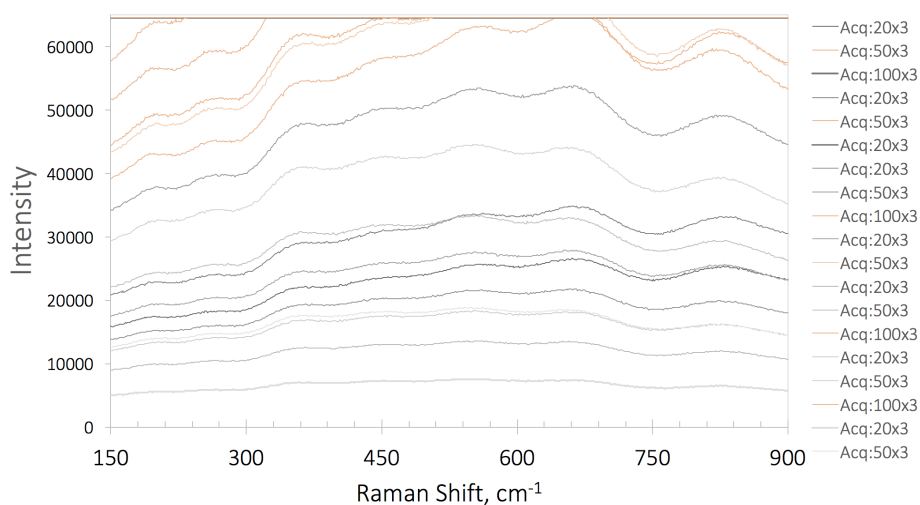

Figure G.1: *Ex situ* measurements of $1Co/Al_2O_3$. No significant peak was observed due to low cobalt loading. The spectra mark with orange was observed to hit the saturation point due to the long exposure time.
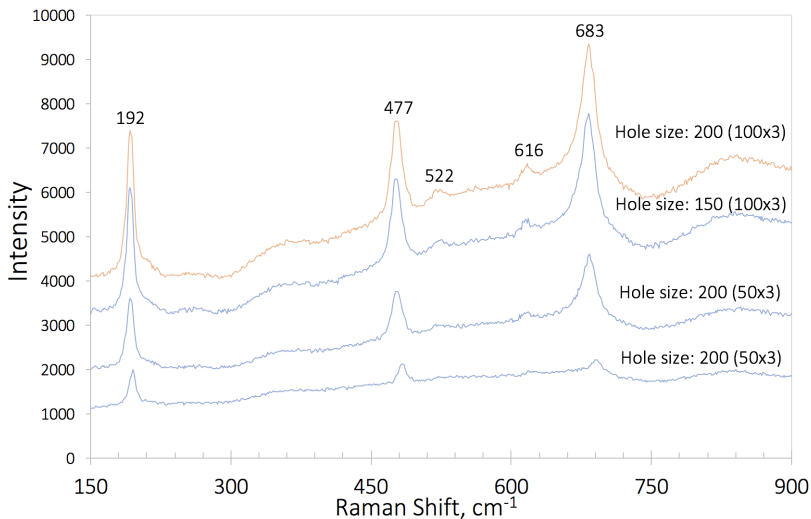
Figure G.2: *Ex situ* measurements of $3Co/Al_2O_3$. The orange spectrum shows the desired spectrum. With the blue spectrum it was observed a peak shift to a higher wavenumber due to more filtration. A better height resolution was observed by increasing the hole size, however decreasing the exposure time also decreases the height resolution. A combination of large hole size and long exposure time gave the desired spectrum.
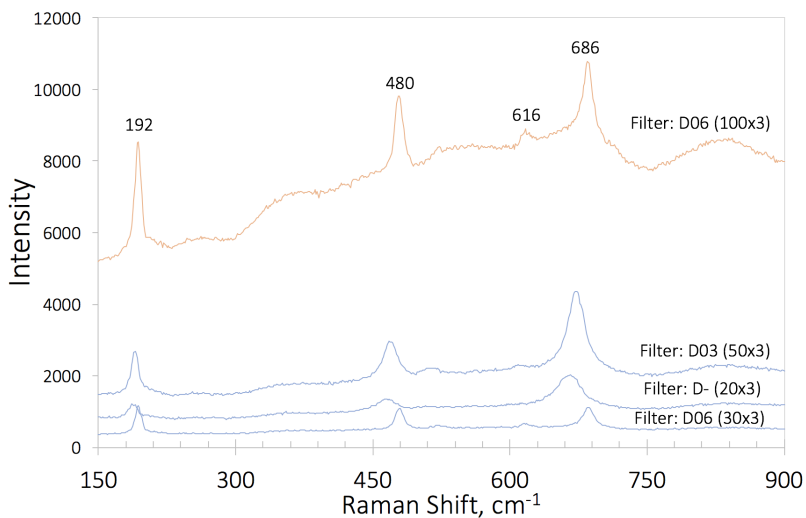

Figure G.3: *Ex situ* measurements of $10Co/Al_2O_3$. The orange spectrum shows the desired spectrum. The blue spectra have the same hole size but different filtration and exposure time. A peak shift to a lower wavenumber due to less filtration is observed, and the intensity increases with increasing exposure time.

Appendix H

In situ Raman spectroscopy

The *in situ* measurements of 5wt.%Pt/ZrO$_2$ with excitation radiation at 633 and 325nm are presented in this section. Oxidation held for 2 hours are presented in Figure H.1 and H.2. Further, after the reduction step, switching to an inert environment and cooled down to room temperature are shown in Figure H.3 and H.4. The catalyst was then reoxidized under a flow of 7%O$_2$/Ar up to 500°C, as presented in Figure H.5 and H.6 and then held for 2 hours (Figure H.7 and H.8). In the end of the measurements the catalyst was cooled down to room temperature presented in Figure H.9 and H.10.

In situ Raman on 5wt.% Pt/ZrO$_2$

Oxidation hold
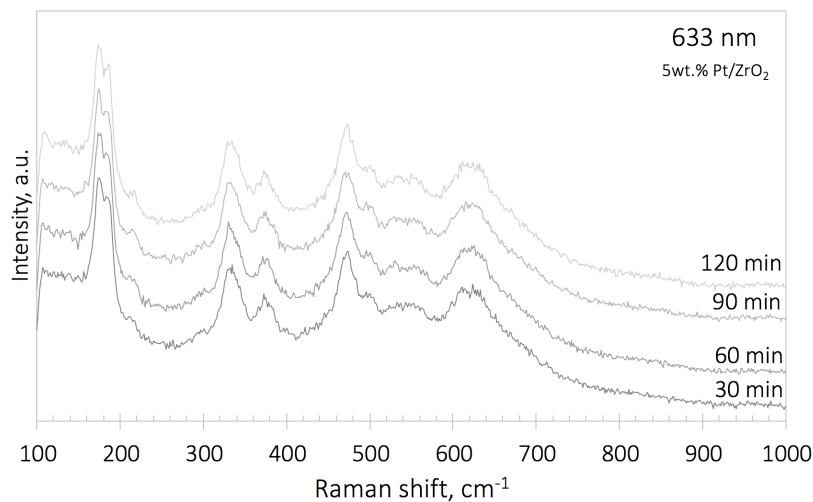
Figure H.1: *In situ* Raman spectra of 5wt.% Pt/ZrO$_2$ under oxidizing conditions at 500°C held for 2 hours using visible laser, with a flow of 40ml/min 7% O$_2$/Ar.

Figure H.2: *In situ* Raman spectra of 5wt.% Pt/ZrO$_2$ under oxidizing conditions at 500°C held for 2 hours using near UV laser, with a flow of 40ml/min 7% O$_2$/Ar.

Reduction cooling

Figure H.3: *In situ* Raman spectra of 5wt.% Pt/ZrO$_2$ after the reduction, cooling down to room temperature under inert environment using visible laser with a flow of 40ml/min argon.

Figure H.4: *In situ* Raman spectra of 5wt.% Pt/ZrO$_2$ after the reduction, cooling down to room temperature under inert environment using near UV laser with a flow of 40ml/min argon.

Reoxidation
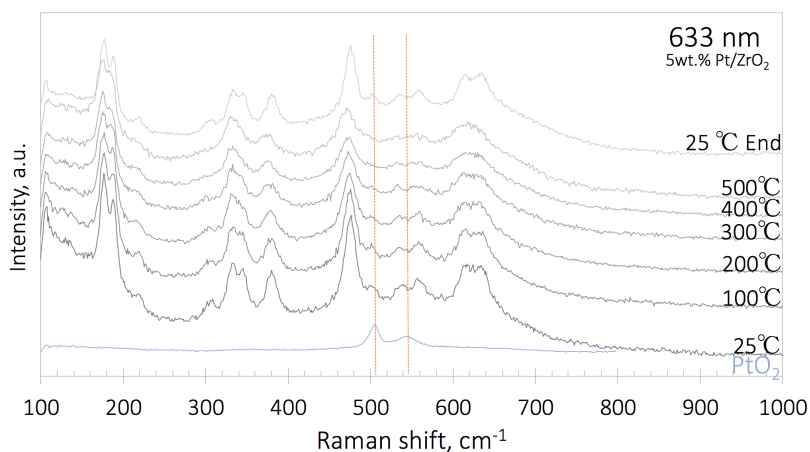
Figure H.5: *In situ* Raman spectra of 5wt.% Pt/ZrO$_2$ measured at different temperatures, from ambient up to 500°C using visible laser, with a flow of 40ml/min 7% O$_2$/Ar. Increasing the temperature increases the noise level, due to thermal expansion. No PtO$_2$ peaks are observed at elevated temperatures.
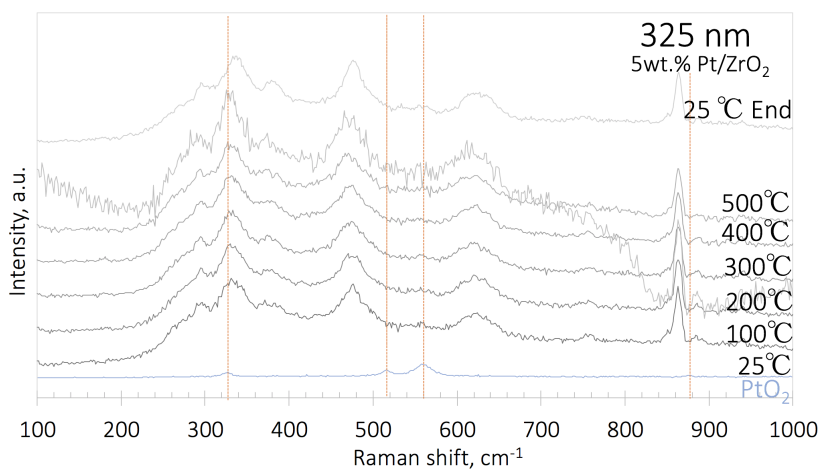
Figure H.6: *In situ* Raman spectra of 5wt.% Pt/ZrO$_2$ measured at different temperatures, from ambient up to 500°C using near UV-light, with a flow of 40ml/min 7% O$_2$/Ar. Increasing the temperature increases the noise level, due to thermal expansion. No PtO$_2$ peaks are observed while increasing the temperature.

Reoxidation hold
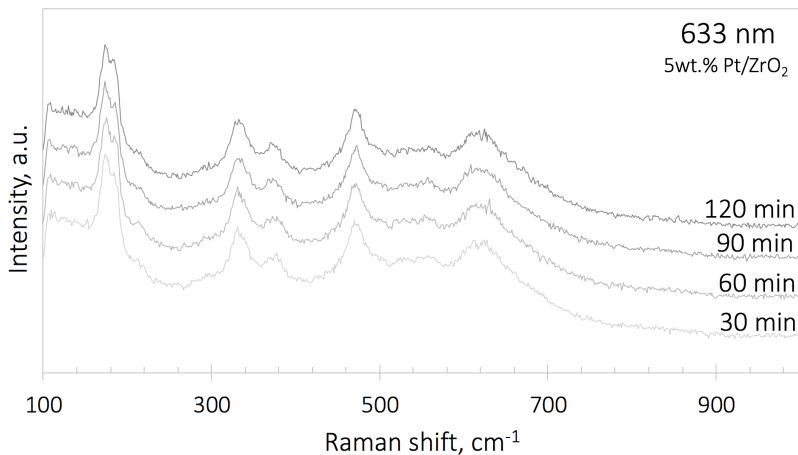
Figure H.7: *In situ* Raman spectra of 5wt.% Pt/ZrO_2 during reoxidation at 500°C held for 2 hours using visible laser, with a flow of 40ml/min 7% O_2/Ar.
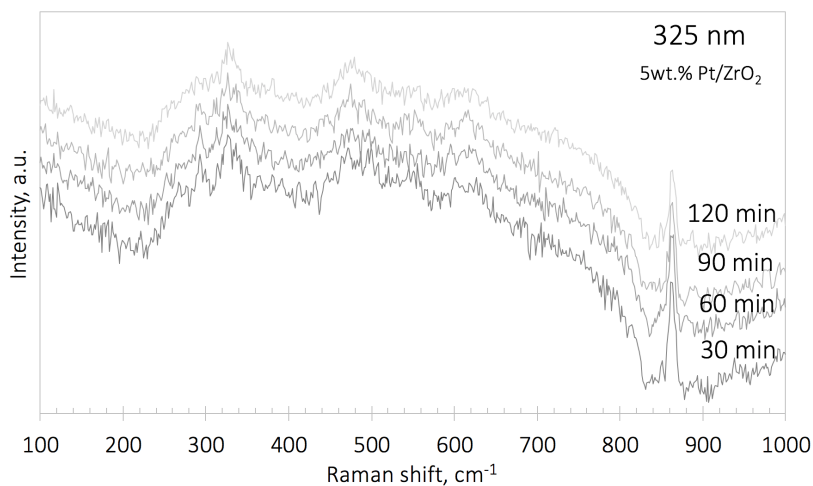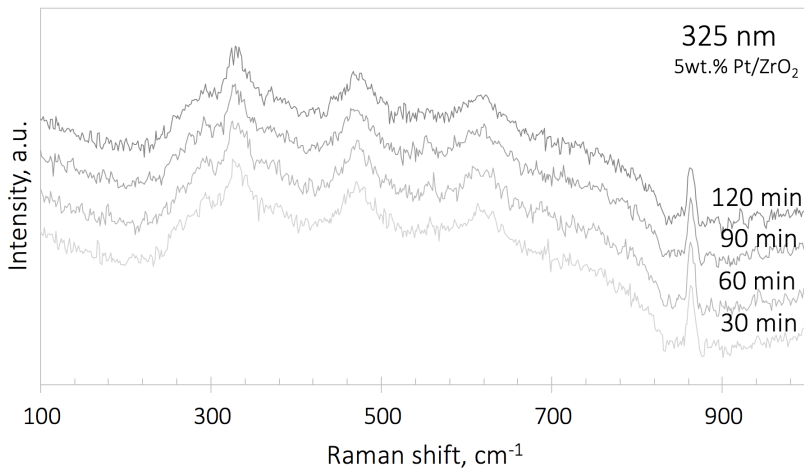

Figure H.8: *In situ* Raman spectra of 5wt.% Pt/ZrO_2 during reoxidation at 500°C held for 2 hours using near UV laser, with a flow of 40ml/min 7% O_2/Ar.
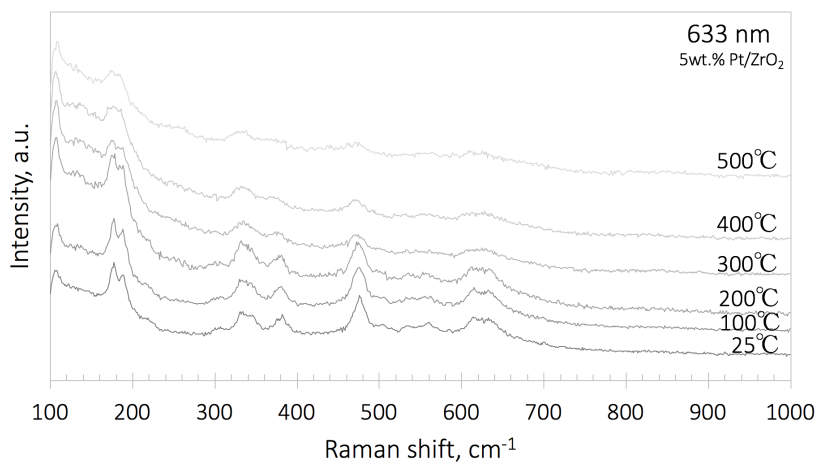
Reoxidation cooling
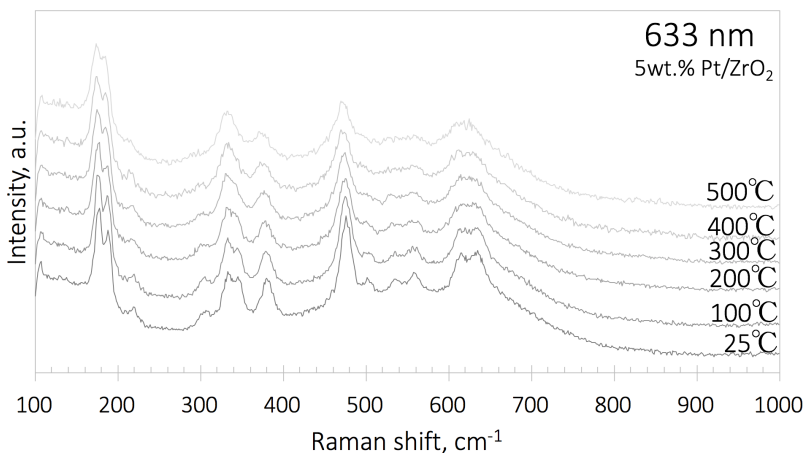
Figure H.9: *In situ* Raman spectra of 5wt.% Pt/ZrO$_2$ after the reoxidizing, cooling down to room temperature under 7% O$_2$/Ar using visible laser with a flow of 40ml/min 7% O$_2$/Ar.
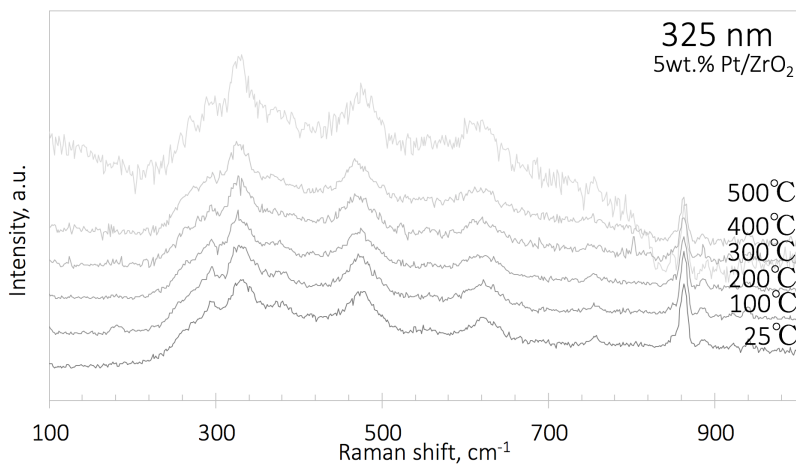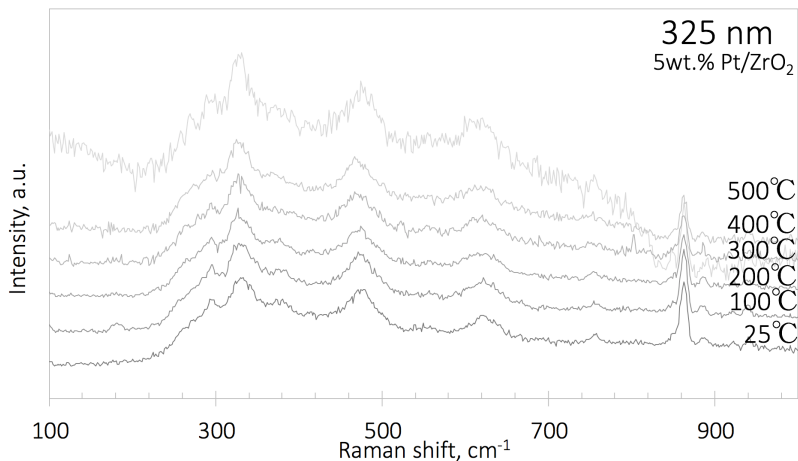

Figure H.10: *In situ* Raman spectra of 5wt.% Pt/ZrO$_2$ after the reoxidizing, cooling down to room temperature under 7% O$_2$/Ar using near UV laser with a flow of 40ml/min 7% O$_2$/Ar.

In situ Raman on 5wt.% Pt/Al$_2$O$_3$

Oxidation
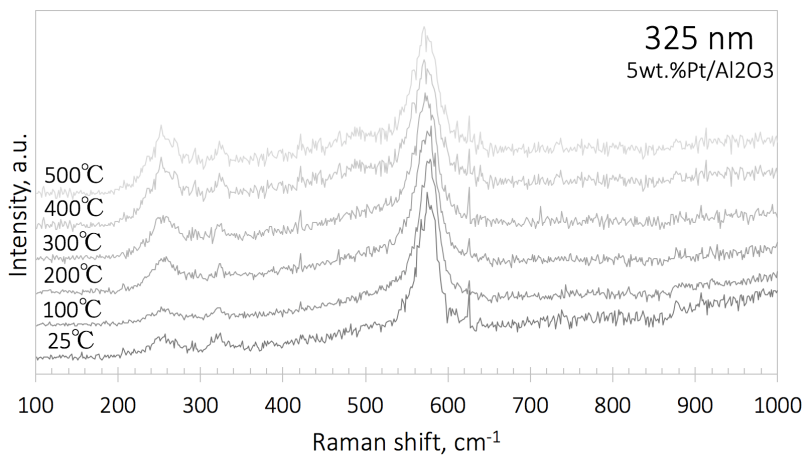
Figure H.11: *In situ* Raman spectra of 5wt.% Pt/Al$_2$O$_3$ under oxidizing conditions using near UV laser with ZnSe window.

Reduction
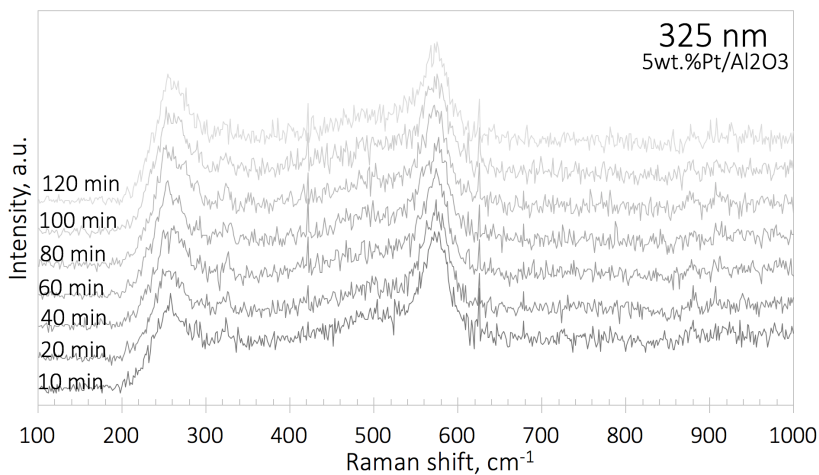
Figure H.12: *In situ* Raman spectra of 5wt.% Pt/Al$_2$O$_3$ under reducing conditions using near UV laser with ZnSe window.

Reoxidation
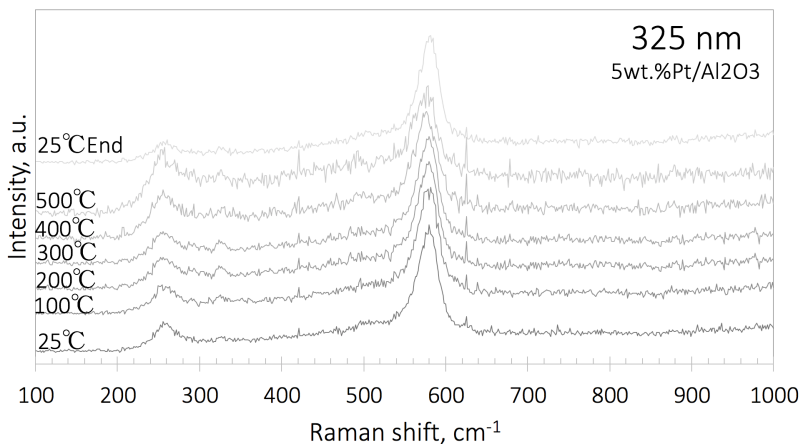
Figure H.13: *In situ* Raman spectra of 5wt.% Pt/Al$_2$O$_3$ under oxidizing conditions after a reduction using near UV laser with ZnSe window.
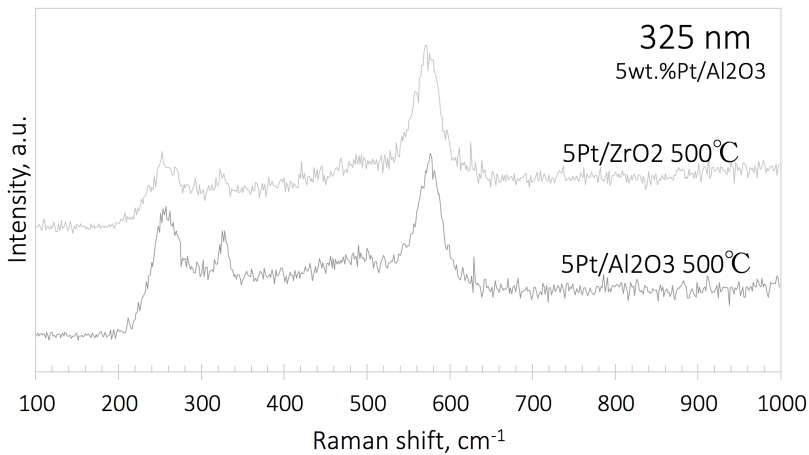
Figure H.14: *In situ* Raman spectra of 5wt.% Pt/ZrO$_2$ 5wt.% Pt/Al$_2$O$_3$ under same conditions, showing identical spectra, indicating that the ZnSe is in focus and not the sample.

Appendix I

Suggested procedure of NO adsorption experiment
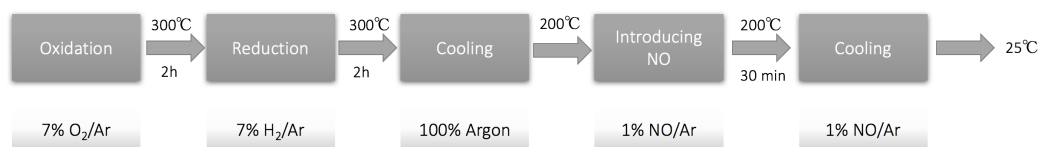
Figure I.1: Block diagram of a suggested procedure of *in situ* Raman experiment of NO adsorption for further work.

Oxidation: Heating up to 300°C, taking raman spectra every 50°C. Hold for 2 hours, taking spectra every 20 minutes.
Purge in Argon for 10-15 minutes.
Reduction: Switching over to a reducing reagent at 300°C, and hold for 2 hours, taking spectra every 20 minutes.
Purge in Argon for 10-15 minutes.
Cooling: Cooling down to 200°C in Argon.
NO: Introducing NO at 200°C, taking spectra every 5 minutes.
Cooling: Cooling down to room temperature in NO, taking spectra every 50°C.

Appendix J

Risk assessment

The risk evaluation performed contains all experiments in the laboratory and is given below. This risk assessment is based on material safety data sheets of chemicals, NTNU HSE handbook and is performed in collaboration with supervisors.

ID	29340		Status	Dato
Risikoområde	Risikovurdering: Helse, miljø og sikkerhet (HMS)		Opprettet	22.05.2018
Opprettet av	My Nhung Thi Tran		Vurdering startet	22.05.2018
Ansvarlig	My Nhung Thi Tran		Tiltak besluttet	
			Avsluttet	

Risikovurdering:
CAT, Master student, 2018, My Nhung Tran

Gyldig i perioden:
1/1/2018 - 6/25/2018

Sted:
4 - Gløshaugen / 427 - Kjemi 5

Mål / hensikt
This risk assessment contains all the activities that the master student My Nhung Tran will perform in the Raman spectroscopy lab of the Catalysis group.

Bakgrunn
The aim of the project is to do an in situ characterization of selected heterogeneous catalysts at relevant conditions in terms of atmospheric pressure, temperature and feed composition.

Beskrivelse og avgrensninger
The catalysts will be prepared by impregnating Alumina (Al_2O_3) and Zirconia (ZrO_2) with platinum nitrate, and drying off the solvent. The catalyst will be measured using in situ Raman spectroscopy with different feed composition as, argon, oxygen, hydrogen and nitrogen monoxide.

Forutsetninger, antakelser og forenklinger
[Ingen registreringer]

Vedlegg
[Ingen registreringer]

Referanser
[Ingen registreringer]

Oppsummering, resultat og endelig vurdering

I oppsummeringen presenteres en oversikt over farer og uønskede hendelser, samt resultat for det enkelte konsekvensområdet.

Farekilde: **Sample preparation Raman**

Uønsket hendelse: **Inhalation of powder**

Konsekvensområde: Helse   Risiko før tiltak: 🟢   Risiko etter tiltak: ⚪

Uønsket hendelse: **Skin contact**

Konsekvensområde: Helse   Risiko før tiltak: 🟢   Risiko etter tiltak: ⚪

Uønsket hendelse: **Eye contact**

Konsekvensområde: Helse   Risiko før tiltak: 🟢   Risiko etter tiltak: ⚪

Farekilde: **Use of lasers**

Uønsket hendelse: **Staring at laser**

Konsekvensområde: Helse   Risiko før tiltak: 🟢   Risiko etter tiltak: ⚪

Farekilde: **Use of compressed gas (Ar, N2)**

Uønsket hendelse: **Gas Leakage**

Konsekvensområde: Helse   Risiko før tiltak: 🟢   Risiko etter tiltak: ⚪

Farekilde: **Use of H2 - flammable gas**

Uønsket hendelse: **Gas Leakage**

Konsekvensområde: Helse   Risiko før tiltak: 🟡   Risiko etter tiltak: ⚪
                       Ytre miljø   Risiko før tiltak: 🟡   Risiko etter tiltak: ⚪
                       Materielle verdier   Risiko før tiltak: 🟡   Risiko etter tiltak: ⚪

Farekilde:	**Use of H2 - flammable gas**		
Uønsket hendelse:	**Fire or explosion**		
Konsekvensområde:	Helse	Risiko før tiltak: 🟡	Risiko etter tiltak: ⚪
	Ytre miljø	Risiko før tiltak: 🟡	Risiko etter tiltak: ⚪
	Materielle verdier	Risiko før tiltak: 🟡	Risiko etter tiltak: ⚪

Farekilde:	**Use of high temperature furnace**		
Uønsket hendelse:	**Burn damage**		
Konsekvensområde:	Helse	Risiko før tiltak: 🟢	Risiko etter tiltak: ⚪

Uønsket hendelse:	**Electric shock**		
Konsekvensområde:	Helse	Risiko før tiltak: 🟢	Risiko etter tiltak: ⚪
	Materielle verdier	Risiko før tiltak: 🟢	Risiko etter tiltak: ⚪

Uønsket hendelse:	**Fire**		
Konsekvensområde:	Helse	Risiko før tiltak: 🟡	Risiko etter tiltak: ⚪
	Ytre miljø	Risiko før tiltak: 🟡	Risiko etter tiltak: ⚪
	Materielle verdier	Risiko før tiltak: 🟡	Risiko etter tiltak: ⚪

Farekilde:	**Use of liquid N2**		
Uønsket hendelse:	**Frost damage**		
Konsekvensområde:	Helse	Risiko før tiltak: 🟢	Risiko etter tiltak: ⚪

Farekilde:	**Preparation of catalysts**		
Uønsket hendelse:	**Chemical burn**		
Konsekvensområde:	Helse	Risiko før tiltak: 🟢	Risiko etter tiltak: ⚪

Uønsket hendelse:	**Formation of harmful chemicals/gas**		
Konsekvensområde:	Helse	Risiko før tiltak: 🟡	Risiko etter tiltak: ⚪
	Ytre miljø	Risiko før tiltak: 🟢	Risiko etter tiltak: ⚪

Farekilde:	**Preparation of catalysts**		

Uønsket hendelse:	**Skin contact**

Konsekvensområde: Helse   Risiko før tiltak: 🟢 Risiko etter tiltak: ⚪

Uønsket hendelse:	**Inhalation**

Konsekvensområde: Helse   Risiko før tiltak: 🟢 Risiko etter tiltak: ⚪

Farekilde:	**Use of CO gas**

Uønsket hendelse:	**Fire or explosion**

Konsekvensområde: Helse   Risiko før tiltak: 🟡 Risiko etter tiltak: ⚪
Ytre miljø   Risiko før tiltak: 🟡 Risiko etter tiltak: ⚪
Materielle verdier   Risiko før tiltak: 🟡 Risiko etter tiltak: ⚪

Uønsket hendelse:	**Gas leakage**

Konsekvensområde: Helse   Risiko før tiltak: 🟢 Risiko etter tiltak: ⚪
Ytre miljø   Risiko før tiltak: 🟢 Risiko etter tiltak: ⚪
Materielle verdier   Risiko før tiltak: 🟢 Risiko etter tiltak: ⚪

Farekilde:	**Use of 2,3% NO/Ar gas**

Uønsket hendelse:	**Gas leakage**

Konsekvensområde: Helse   Risiko før tiltak: 🟡 Risiko etter tiltak: ⚪
Ytre miljø   Risiko før tiltak: 🟢 Risiko etter tiltak: ⚪

Uønsket hendelse:	**Fire or explosion**

Konsekvensområde: Helse   Risiko før tiltak: 🟡 Risiko etter tiltak: ⚪
Ytre miljø   Risiko før tiltak: 🟡 Risiko etter tiltak: ⚪
Materielle verdier   Risiko før tiltak: 🟡 Risiko etter tiltak: ⚪

Endelig vurdering

Involverte enheter og personer

En risikovurdering kan gjelde for en, eller flere enheter i organisasjonen. Denne oversikten presenterer involverte enheter og personell for gjeldende risikovurdering.

Enhet /-er risikovurderingen omfatter

- Fakultet for naturvitenskap (NV)

Deltakere

Samuel K. Regli

Magnus Rønning

Karin Wiggen Dragsten

Lesere

[Ingen registreringer]

Andre involverte/interessenter

[Ingen registreringer]

Følgende akseptkriterier er besluttet for risikoområdet Risikovurdering: Helse, miljø og sikkerhet (HMS):

Helse   **Materielle verdier**   **Omdømme**   **Ytre miljø**

Oversikt over eksisterende, relevante tiltak som er hensyntatt i risikovurderingen

I tabellen under presenteres eksisterende tiltak som er hensyntatt ved vurdering av sannsynlighet og konsekvens for aktuelle uønskede hendelser.

Farekilde	Uønsket hendelse	Tiltak hensyntatt ved vurdering
Sample preparation Raman	Inhalation of powder	Lab Coat
	Inhalation of powder	Safety Googles
	Inhalation of powder	Nitrile Gloves
	Inhalation of powder	Ventilation Hood
	Inhalation of powder	Emergency equipment in labs
	Skin contact	Lab Coat
	Skin contact	Safety Googles
	Skin contact	Nitrile Gloves
	Skin contact	Ventilation Hood
	Skin contact	Emergency equipment in labs
	Eye contact	Lab Coat
	Eye contact	Safety Googles
	Eye contact	Nitrile Gloves
	Eye contact	Ventilation Hood
	Eye contact	Emergency equipment in labs
Use of lasers	Staring at laser	Safety Googles
	Staring at laser	HSE documentation
Use of compressed gas (Ar, N2)	Gas Leakage	Ventilation Hood
	Gas Leakage	Gas Detection
	Gas Leakage	Gas Leakage Test
	Gas Leakage	HSE documentation
Use of H2 - flammable gas	Gas Leakage	Ventilation Hood
	Gas Leakage	Gas Detection
	Gas Leakage	Emergency equipment in labs
	Gas Leakage	Gas Leakage Test
	Gas Leakage	HSE documentation
	Fire or explosion	Gas Detection
	Fire or explosion	Incident and discrepancy
	Fire or explosion	Emergency equipment in labs
	Fire or explosion	Gas Leakage Test
	Fire or explosion	HSE documentation
Use of high temperature furnace	Burn damage	Lab Coat
	Burn damage	Safety Googles

Norges teknisk-naturvitenskapelige universitet (NTNU)   **Utskriftsdato:**   **Utskrift foretatt av:**   **Side:**

Unntatt offentlighet jf. Offentlighetsloven § 14   22.05.2018   My Nhung Thi Tran   6/26

Use of high temperature furnace	Burn damage	Nitrile Gloves
	Burn damage	Emergency equipment in labs
	Burn damage	Heat restistant gloves
	Electric shock	Lab Coat
	Electric shock	Safety Googles
	Electric shock	Nitrile Gloves
	Fire	Gas Detection
	Fire	Incident and discrepancy
	Fire	Emergency equipment in labs
Use of liquid N2	Frost damage	Lab Coat
	Frost damage	Safety Googles
	Frost damage	Nitrile Gloves
Preparation of catalysts	Chemical burn	Lab Coat
	Chemical burn	Safety Googles
	Chemical burn	Nitrile Gloves
	Chemical burn	Ventilation Hood
	Chemical burn	Emergency equipment in labs
	Formation of harmful chemicals/gas	Lab Coat
	Formation of harmful chemicals/gas	Safety Googles
	Formation of harmful chemicals/gas	Nitrile Gloves
	Formation of harmful chemicals/gas	Ventilation Hood
	Skin contact	Lab Coat
	Skin contact	Safety Googles
	Skin contact	Nitrile Gloves
	Skin contact	Ventilation Hood
	Skin contact	Emergency equipment in labs
	Inhalation	Lab Coat
	Inhalation	Safety Googles
	Inhalation	Nitrile Gloves
	Inhalation	Ventilation Hood
Use of CO gas	Fire or explosion	Gas Detection
	Fire or explosion	Incident and discrepancy
	Fire or explosion	Gas Leakage Test
	Gas leakage	Gas Detection
	Gas leakage	Gas Leakage Test
Use of 2,3% NO/Ar gas	Gas leakage	Gas Detection
	Gas leakage	Gas Leakage Test
	Fire or explosion	Gas Detection
	Fire or explosion	Incident and discrepancy

Norges teknisk-naturvitenskapelige universitet (NTNU)   **Utskriftsdato:**   **Utskrift foretatt av:**   **Side:**

Unntatt offentlighet jf. Offentlighetsloven § 14   22.05.2018   My Nhung Thi Tran   7/26

Use of 2,3% NO/Ar gas	Fire or explosion	Emergency equipment in labs
	Fire or explosion	Gas Leakage Test
	Fire or explosion	HSE documentation

Eksisterende og relevante tiltak med beskrivelse:

Lab Coat

Protect the clothing and skin from chemical that may be spilled or splashed.

Safety Googles

Eye and face protection to reduce of chemical exposure, and is required of everyone who enters a chemical work area. Laser safety glasses provides laser radiation protection.

Nitrile Gloves

Hand protection of chemicals. Replace glove after every sample preparation.

Ventilation Hood

[Ingen registreringer]

Gas Detection

Raman lab contains gas alarm detector in case of gas leakage. Blue flashing light indicate low alarm, no evacuation needed. Red flashing light indicate high alarm, gas signal goes to fire central.

Incident and discrepancy

All incident or discrepancy need to be reported.

Emergency equipment in labs

In the laboratory it contains emergency equipment such as first aid kit, emergency showers, emergency eye wash and different fire extinguishers.

Gas Leakage Test

[Ingen registreringer]

HSE documentation

In the lab there are room cards that provide information concerning potential hazards, first aid equipment's and room responsible.

Heat restistant gloves

Using furnaces to calcine the support and impregnated catalyst. Protection against burns

Risikoanalyse med vurdering av sannsynlighet og konsekvens

I denne delen av rapporten presenteres detaljer dokumentasjon av de farer, uønskede hendelser og årsaker som er vurdert. Innledningsvis oppsummeres farer med tilhørende uønskede hendelser som er tatt med i vurderingen.

Følgende farer og uønskede hendelser er vurdert i denne risikovurderingen:

- **Sample preparation Raman**
    - Inhalation of powder
    - Skin contact
    - Eye contact
- **Use of lasers**
    - Staring at laser
- **Use of compressed gas (Ar, N2)**
    - Gas Leakage
- **Use of H2 - flammable gas**
    - Gas Leakage
    - Fire or explosion
- **Use of high temperature furnace**
    - Burn damage
    - Electric shock
    - Fire
- **Use of liquid N2**
    - Frost damage
- **Preparation of catalysts**
    - Chemical burn
    - Formation of harmful chemicals/gas
    - Skin contact
    - Inhalation
- **Use of CO gas**
    - Fire or explosion
    - Gas leakage
- **Use of 2,3% NO/Ar gas**
    - Gas leakage
    - Fire or explosion

Detaljert oversikt over farekilder og uønskede hendelser:

Farekilde: Sample preparation Raman

Sample preparation in Raman room contains of powder samples that need to be moved from the preparation table to the microscope.

Uønsket hendelse: Inhalation of powder

When moving the sample from the preparation table to the microscope, there is a risk that some powder will float in the air.

Sannsynlighet for hendelsen (felles for alle konsekvensområder):   **Lite sannsynlig (2)**

Kommentar:

[Ingen registreringer]

Konsekvensområde: Helse   *Risiko:*

Vurdert konsekvens: **Liten (1)**

Kommentar: [Ingen registreringer]

Uønsket hendelse: Skin contact

While doing a sample preparation lab coat and gloves must be worn to avoid contact with skin.

Sannsynlighet for hendelsen (felles for alle konsekvensområder):   **Svært lite sannsynlig (1)**

Kommentar:

[Ingen registreringer]

Konsekvensområde: Helse   *Risiko:*

Vurdert konsekvens: **Liten (1)**

Kommentar: [Ingen registreringer]

Uønsket hendelse: Eye contact

Avoid samples to get in contact with eye while preparering samples. Use googles and gloves when preparering.

Sannsynlighet for hendelsen (felles for alle konsekvensområder):　　**Svært lite sannsynlig (1)**

　　　Kommentar:

　　　[Ingen registreringer]

Konsekvensområde: Helse　　　　　　　　　　　　　　　　　　　　　　　　　*Risiko:*

　　Vurdert konsekvens: **Middels (2)**

　　　　Kommentar: [Ingen registreringer]

Norges teknisk-naturvitenskapelige universitet (NTNU)　　**Utskriftsdato:**　**Utskrift foretatt av:**　　　　　　**Side:**

Unntatt offentlighet jf. Offentlighetsloven § 14　　22.05.2018　　My Nhung Thi Tran　　　　11/26

Farekilde: Use of lasers

Laser radiation can cause eye injury and skin burn. Class 3B lasers are hazardous for eye exposure. They can heat skin and materials but are not considered a burn hazard.

Uønsket hendelse: Staring at laser

Staring directly into the laser can cause eye injury.

Sannsynlighet for hendelsen (felles for alle konsekvensområder):   **Svært lite sannsynlig (1)**

    Kommentar:

    [Ingen registreringer]

Konsekvensområde: Helse   *Risiko:*

    Vurdert konsekvens: **Liten (1)**

        Kommentar: [Ingen registreringer]

Norges teknisk-naturvitenskapelige universitet (NTNU)   **Utskriftsdato:**   **Utskrift foretatt av:**   **Side:**

Unntatt offentlighet jf. Offentlighetsloven § 14   22.05.2018   My Nhung Thi Tran   12/26

Farekilde: Use of compressed gas (Ar, N2)

Gas is fed to in situ cell while doing a characterization.

Uønsket hendelse: Gas Leakage

Sannsynlighet for hendelsen (felles for alle konsekvensområder):   **Svært lite sannsynlig (1)**

    Kommentar:

    [Ingen registreringer]

Konsekvensområde: Helse   *Risiko:*

    Vurdert konsekvens: **Liten (1)**

        Kommentar: [Ingen registreringer]

Farekilde: Use of H2 - flammable gas

Hydrogen is used in a reduction experiment. Hydrogen is fed to the in situ cell.

Uønsket hendelse: Gas Leakage

Sannsynlighet for hendelsen (felles for alle konsekvensområder): **Sannsynlig (3)**

 Kommentar:

 [Ingen registreringer]

Konsekvensområde: Helse *Risiko:*

 Vurdert konsekvens: **Middels (2)**

 Kommentar: [Ingen registreringer]

Konsekvensområde: Ytre miljø *Risiko:*

 Vurdert konsekvens: **Middels (2)**

 Kommentar: [Ingen registreringer]

Konsekvensområde: Materielle verdier *Risiko:*

 Vurdert konsekvens: **Middels (2)**

 Kommentar: [Ingen registreringer]

Uønsket hendelse: Fire or explosion

- -

Sannsynlighet for hendelsen (felles for alle konsekvensområder): **Svært lite sannsynlig (1)**

Kommentar:

[Ingen registreringer]

Konsekvensområde: Helse *Risiko:*

Vurdert konsekvens: **Stor (3)**

Kommentar: [Ingen registreringer]

Konsekvensområde: Ytre miljø *Risiko:*

Vurdert konsekvens: **Stor (3)**

Kommentar: [Ingen registreringer]

Konsekvensområde: Materielle verdier *Risiko:*

Vurdert konsekvens: **Stor (3)**

Kommentar: [Ingen registreringer]

Farekilde: Use of high temperature furnace

Zirconia will be calcined in HT-furnaces. Catalyst/impregnated alumina and zirconia will be dryed/calcined in furnaces.

Uønsket hendelse: Burn damage

Accidentally touching a hot surface on the furnace may cause burns.

Sannsynlighet for hendelsen (felles for alle konsekvensområder):   **Lite sannsynlig (2)**
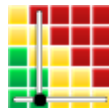
> *Kommentar:*
> [Ingen registreringer]

Konsekvensområde: Helse

> *Vurdert konsekvens:* **Middels (2)**
>
> > *Kommentar:* [Ingen registreringer]

Risiko:

Uønsket hendelse: Electric shock

When operating the furnace there is a chance to get electric shock.

Sannsynlighet for hendelsen (felles for alle konsekvensområder):   **Svært lite sannsynlig (1)**
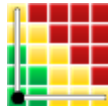
> *Kommentar:*
> [Ingen registreringer]

Konsekvensområde: Helse

> *Vurdert konsekvens:* **Middels (2)**
>
> > *Kommentar:* [Ingen registreringer]

Risiko:

Konsekvensområde: Materielle verdier

> *Vurdert konsekvens:* **Liten (1)**
>
> > *Kommentar:* [Ingen registreringer]

Risiko:

Uønsket hendelse: Fire

- -

Sannsynlighet for hendelsen (felles for alle konsekvensområder):   **Lite sannsynlig (2)**

    Kommentar:

    [Ingen registreringer]

Konsekvensområde: Helse   *Risiko:*

    Vurdert konsekvens: **Stor (3)**

        Kommentar: [Ingen registreringer]

Konsekvensområde: Ytre miljø   *Risiko:*

    Vurdert konsekvens: **Stor (3)**

        Kommentar: [Ingen registreringer]

Konsekvensområde: Materielle verdier   *Risiko:*

    Vurdert konsekvens: **Stor (3)**

        Kommentar: [Ingen registreringer]

Farekilde: Use of liquid N2

Using liquid N2 to measure the nitrogen absorption of the catalysts.

Uønsket hendelse: Frost damage

Spilling liquid N2 can cause frost damage.

Sannsynlighet for hendelsen (felles for alle konsekvensområder):   **Lite sannsynlig (2)**

   Kommentar:
   [Ingen registreringer]

Konsekvensområde: Helse   *Risiko:*

   Vurdert konsekvens: **Middels (2)**

      Kommentar: [Ingen registreringer]

Norges teknisk-naturvitenskapelige universitet (NTNU)   **Utskriftsdato:**   **Utskrift foretatt av:**   **Side:**

Unntatt offentlighet jf. Offentlighetsloven § 14   22.05.2018   My Nhung Thi Tran   18/26

Farekilde: Preparation of catalysts

Preparation of precursor solution and impregnation of alumina and zirconia support. Diluting Platinum nitrate solution and impregnating alumina and zirconia.

Uønsket hendelse: Chemical burn

Platinum nitrate is corrosive and oxidising.

Sannsynlighet for hendelsen (felles for alle konsekvensområder):   **Lite sannsynlig (2)**

    Kommentar:

    [Ingen registreringer]

Konsekvensområde: Helse   *Risiko:*

    Vurdert konsekvens: **Middels (2)**

        Kommentar: [Ingen registreringer]

Uønsket hendelse: Formation of harmful chemicals/gas

Platinum nitrate may react and form harmful gas.

Sannsynlighet for hendelsen (felles for alle konsekvensområder):   **Sannsynlig (3)**

    Kommentar:
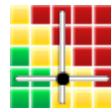
    [Ingen registreringer]

Konsekvensområde: Helse   *Risiko:*

    Vurdert konsekvens: **Middels (2)**

        Kommentar: [Ingen registreringer]

Konsekvensområde: Ytre miljø   *Risiko:*

    Vurdert konsekvens: **Liten (1)**

        Kommentar: [Ingen registreringer]

Uønsket hendelse: Skin contact

Spill of platina onto skin

Sannsynlighet for hendelsen (felles for alle konsekvensområder):   **Lite sannsynlig (2)**

   Kommentar:
   [Ingen registreringer]

Konsekvensområde: Helse   *Risiko:*

   Vurdert konsekvens: **Middels (2)**

      Kommentar: [Ingen registreringer]

Uønsket hendelse: Inhalation

Sannsynlighet for hendelsen (felles for alle konsekvensområder):   **Lite sannsynlig (2)**

   Kommentar:
   [Ingen registreringer]

Konsekvensområde: Helse   *Risiko:*

   Vurdert konsekvens: **Middels (2)**

      Kommentar: [Ingen registreringer]

Norges teknisk-naturvitenskapelige universitet (NTNU)   **Utskriftsdato:**   **Utskrift foretatt av:**   **Side:**

Unntatt offentlighet jf. Offentlighetsloven § 14   22.05.2018   My Nhung Thi Tran   20/26

Farekilde: Use of CO gas

CO gas is used to measure the dispersion of the catalysts

Uønsket hendelse: Fire or explosion

Carbon oxides are extremely flammable

Sannsynlighet for hendelsen (felles for alle konsekvensområder): **Lite sannsynlig (2)**

Kommentar:

[Ingen registreringer]

Konsekvensområde: Helse   *Risiko:*

Vurdert konsekvens: **Stor (3)**

Kommentar: [Ingen registreringer]

Konsekvensområde: Ytre miljø   *Risiko:*

Vurdert konsekvens: **Stor (3)**

Kommentar: [Ingen registreringer]

Konsekvensområde: Materielle verdier   *Risiko:*

Vurdert konsekvens: **Stor (3)**

Kommentar: [Ingen registreringer]

Uønsket hendelse: Gas leakage

- -

Sannsynlighet for hendelsen (felles for alle konsekvensområder):   **Svært lite sannsynlig (1)**

      Kommentar:

      [Ingen registreringer]

Konsekvensområde: Helse   *Risiko:*

      Vurdert konsekvens: **Middels (2)**

            Kommentar: [Ingen registreringer]

Konsekvensområde: Ytre miljø   *Risiko:*

      Vurdert konsekvens: **Liten (1)**

            Kommentar: [Ingen registreringer]

Konsekvensområde: Materielle verdier   *Risiko:*

      Vurdert konsekvens: **Liten (1)**

            Kommentar: [Ingen registreringer]

Farekilde: Use of 2,3% NO/Ar gas

NO gas is used when doing in situ Raman adsorption measurements

Uønsket hendelse: Gas leakage
- -

Sannsynlighet for hendelsen (felles for alle konsekvensområder):   **Lite sannsynlig (2)**

    Kommentar:

    [Ingen registreringer]

Konsekvensområde: Helse   *Risiko:*

    Vurdert konsekvens: **Stor (3)**

       Kommentar: [Ingen registreringer]

Konsekvensområde: Ytre miljø   *Risiko:*

    Vurdert konsekvens: **Middels (2)**

       Kommentar: [Ingen registreringer]

Uønsket hendelse: Fire or explosion
- -
May cause or intensify fire, oxidiser.
Contains gas under pressure, may explode if heated.

Sannsynlighet for hendelsen (felles for alle konsekvensområder):   **Lite sannsynlig (2)**

    Kommentar:

    [Ingen registreringer]

Konsekvensområde: Helse   *Risiko:*

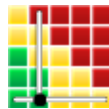   *Vurdert konsekvens:* **Stor (3)**
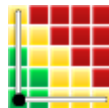
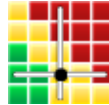   *Kommentar:* [Ingen registreringer]

Konsekvensområde: Ytre miljø

Vurdert konsekvens: **Stor (3)**

Kommentar: [Ingen registreringer]

Risiko:

Konsekvensområde: Materielle verdier

Vurdert konsekvens: **Stor (3)**

Kommentar: [Ingen registreringer]

Risiko:

Oversikt over besluttede risikoreduserende tiltak:

Under presenteres en oversikt over risikoreduserende tiltak som skal bidra til å reduseres sannsynlighet og/eller konsekvens for uønskede hendelser.

Detaljert oversikt over besluttede risikoreduserende tiltak med beskrivelse:

Detaljert oversikt over vurdert risiko for hver farekilde/uønsket hendelse før og etter besluttede tiltak

Norges teknisk-naturvitenskapelige universitet (NTNU)

Unntatt offentlighet jf. Offentlighetsloven § 14

Utskriftsdato:

22.05.2018

Utskrift foretatt av:

My Nhung Thi Tran

Side:

26/26